12-2007

EFFECT OF CARBON NANOFIBERS ON MICROSTRUCTURE AND PROPERTIES OF POLYMER NANOCOMPOSITES

Sungho Lee
Clemson University, sunghol@clemson.edu

EFFECT OF CARBON NANOFIBERS ON MICROSTRUCTURE AND PROPERTIES OF POLYMER NANOCOMPOSITES

A Dissertation
Presented to
the Graduate School of
Clemson University

In Partial Fulfillment
of the Requirements for the Degree
Doctor of Philosophy
Chemical Engineering

---

by
Sungho Lee
December 2007

Accepted by:
Dr. Amod A. Ogale, Committee Chair
Dr. Douglas E. Hirt
Dr. Graham M. Harrison
Dr. Gary C. Lickfield

ABSTRACT

Nano-modifiers are typically three orders of magnitude smaller in size than their micro-counterparts. At this scale, interactions between matrix molecules and the nano-modifiers can lead to novel physical and chemical properties of the resulting nanocomposites. Carbon nanofibers (CNFs) are a class of nano-modifiers that has received significant attention recently because they have superior electrical conductivity and mechanical properties with a high aspect ratio (length over diameter). Several recent research studies have focused on enhancing electrical and mechanical performance of composites in the presence of CNFs. However, the influence of CNFs on the structure of the polymer matrix is important in understanding the role CNFs have on the properties of nanocomposites, but this has not been thoroughly examined. Therefore, crystalline and orientational structure of CNF/polymer composites was investigated in this study.

First, the microstructure of two different grades of CNFs, MJ (experimental) and PR (commercial), was investigated as a function of different thermal treatments. Using Raman spectroscopy and XRD analysis, an enhancement of crystallite size was observed after heat treatment at 2200°C. The crystallite thickness increased from 1.6±0.1 nm to 10.9±0.5 nm for MJ fibers and from 3.1±0.3 nm to 11.7±0.4 nm for PR fibers. Also, an increase in thermal oxidation stability for heat-treated CNFs was observed. BET adsorption isotherms showed a significant reduction of specific surface area of MJ fibers after the heat treatment, resulting from a decrease of pore volume. However, even after heat treatment, MJ fibers possessed a rougher surface than did PR fibers. The role of such

nano-texture was studied on two distinct types of polymeric matrices: flexible-chain and semi rigid-rod polymers.

Linear low density polyethylene (LLDPE), a flexible-chain polymer, is widely used for packaging applications because of its film-forming properties and good barrier characteristics. However, LLDPE has a poor electrical conductivity, which results in poor EMI/ESD shielding. Therefore, CNFs were incorporated into LLDPE to improve electrical conductivity. The Electrical percolation threshold was observed at approximately 15 wt% MJ (MJ15) and 30 wt% PR (PR30). Tensile modulus increased from 110 MPa for pure LLDPE to 200 MPa and 300 MPa for MJ15 and PR15, respectively. However, the tensile strength remained fairly unchanged at about 20 MPa. Strain-to-failure decreased from 690% for pure LLDPE to 460% and 120% for MJ15 and PR15, respectively. This indicates that the interfacial bonding of LLDPE matrix with MJ fibers is better than that with PR fibers, possibly due to rougher surface of the MJ fibers.

Crystallization behavior of LLDPE nanocomposites was investigated in the presence of three types of CNFs (MJ, PR, and PRCVD). During non-isothermal crystallization studies, all three crystalline melting peaks for LLDPE matrix were observed in the presence of PRCVD fibers up to 15 wt% content. However, at only 1 wt% MJ fibers, the disappearance of the intermediate melting peak was observed. The broad melting peak at the lower temperature became larger, suggesting an increase in the relative content of thinner lamellae in the presence of MJ fibers. The larger and the rougher surface of MJ fibers observed from the nano-textural study contributes toward the different crystallization behavior of MJ/LLDPE composites. TEM micrographs of

nanocomposites revealed transcrystallinity of LLDPE on the surface of CNFs. Further, a broader distribution of LLDPE lamellar thickness was observed in TEM images of MJ composites.

The third major component of this research project was a study on the role of CNFs on a thermotropic liquid crystalline polymer (TLCP) matrix possessing a semi rigid-rod molecular structure. A variation of anisotropy of the TLCP was investigated in the presence of CNFs. Electrical percolation threshold was observed at approximately 5 wt% MJ fibers. Decrease of tensile modulus and strength was observed for composites. For a given type of flow, wide angle X-ray diffraction studies showed a decrease in Herman's orientation parameter from 0.85 for pure V400P to 0.71 for 5 wt% MJ composites. Thus, the presence of CNFs led to a reduction of the overall anisotropy of the nematic phase in the nanocomposite.

The disruption of molecular orientation of TLCPs was inferred by SEM and TEM analysis. SEM micrographs revealed a fibrillar structure for pure TLCPs at a macro-scale. However, this structure was not observed in composites at the same scale although micro-size fibrils were found with the addition of PR fibers. TEM micrographs displayed banded structures of pure TLCPs, but these structures were not significant in the vicinity of PR fibers. These results indicate that CNFs can help to reduce the severe anisotropy that is otherwise observed for TLCPs. In summary, this study establishes the significant role of CNFs as nano-modifiers that help modify the texture of the matrix while serving to enhance specific properties, such as electrical conductivity, for the nanocomposites.

DEDICATION

This work is dedicated to my parents, Mr. Youngsoo Lee and Mrs. Youngsook Youm.

ACKNOWLEDGMENTS

I would like to appreciate individuals, who provided academic and mental supports. Their assistance made me complete this work successfully.

First, I would like to thank my advisor, Dr. Amod A. Ogale for his motivation, and guidance during my research. His precious advice and patience helped me go through the course of my study.

I am deeply grateful to my committee members, Dr. Hirt, Dr. Harrison, and Dr. Lickfield for their time and proficient suggestions during the experiments.

I sincerely appreciate Dr. Myung-Soo Kim for his invaluable effort and encouragement through scientific discussion and technical help in carbon research over the last four years.

Dr. Ogale's research group members, Dr. Amit Naskar, Dr. Srinivas Cherukupalli, Dr. Tianren Guo, Dr. Santanu Kundu, Mr. Eric Quin, Mr. Giriprasath Gururajan, Mr. Dan Sweeney, Ms. Rebecca Always-Cooper, and Mr. Marlon Morales helped me enjoy the stay in Clemson with friendship and collaborations. I thank Dr. Heifeng for his collaboration on X-ray diffraction measurement.

Mr. Bill Coburn provided a technical service for a great research environment. Also, I acknowledge Dr. JoAn S. Hudson, Mr. Amar Kumbhar, Mr. Cash Dayton, and Mr. Donald Mulwee for their help in conducting SEM and TEM experiments.

I thank the Center for Advanced Engineering Fibers and Films for financial support of this research work through the ERC program of the National Science Foundation.

With the endless love, understanding, and support of my parents, Mr. Youngsoo Lee and Mrs. Youngsook Youm, it was possible to attain this goal. Finally, I appreciate my lovely wife, Mrs. Sook Lim, for her support and inspiration, which allowed me to focus on the research. My son, Justin J. Lee, was a great source of cheer-up.

TABLE OF CONTENTS

Page

TITLE PAGE i

ABSTRACT ii

DEDICATION v

ACKNOWLEDGMENTS vi

LIST OF TABLES xi

LIST OF FIGURES xii

CHAPTER

1. INTRODUCTION 1

1.1 Introduction to nanocomposites 1
1.2 Carbon nanofibers 2
1.2.1 Synthesis of carbon nanofibers 3
1.2.2 Modification of carbon nanofibers 7
1.2.3 Analysis of carbon nanofiber 8
1.3 Carbon nanofibers based nanocomposites 12
1.3.1 Electrical properties of carbon nanofibers based nanocomposites 13
1.3.2 Mechanical properties of carbon nanofibers based nanocomposites 18
1.3.3 Crystalline structure of polymer in carbon nanofibers based nanocomposites 21
1.4 Thermotropic liquid crystalline polymer 24
1.4.1 Liquid crystalline polymers 28
1.4.2 Structure and orientation of TLCP 32
1.4.3 Liquid crystalline polymer composites with carbonaceous materials 36
1.5 Objectives 38

2. STRUCTURAL CHARACTERIZATION OF CARBON NANOFIBERS 41

2.1 Introduction 41
2.2 Experimental 42
2.2.1 Materials 42
2.2.2 Characterization 44

Table of Contents (Continued)

Page

2.3 Results and Discussion 44
2.3.1 Crystalline structure of CNFs 44
2.3.2 Morphology of CNFs 51
2.4 Conclusions 64

3. INFLUENCE OF CARBON NANOFIBERS ON THE PROPERTIES AND CRYSTALLIZATION BEHAVIOR OF LINEAR LOW DENSITY POLYETHYLENE NANOCOMPOSITES 66

3.1 Introduction 66
3.2 Experimental 67
3.2.1 Materials 67
3.2.2 Nanocomposite characterization 68
3.3 Results and Discussion 70
3.3.1 Electrical and mechanical properties 70
3.3.2 Crystallization kinetics 81
3.3.4 Microstructure 97
3.4 Conclusions 101

4. EFFECT OF CARBON NANOFIBERS ON THE ANISOTROPY OF AN AROMATIC THERMOTROPIC LIQUID CRYSTALLINE POLYMER 102

4.1 Introduction 102
4.2 Experimental 103
4.2.1 Materials 103
4.2.2 Processing 104
4.2.3 Characterization 105
4.3 Results and Discussion 106
4.3.1 Electrical and mechanical properties 106
4.3.2 Wide angle X-ray diffraction analysis 110
4.3.3 Microstructure and morphology 127
4.4 Conclusions 140

5. CONCLUSIONS AND RECOMMENDATIONS 142

5.1 Conclusions 142
5.2 Recommendations for future work 145

Table of Contents (Continued)

Page

APPENDICES 149

LITERATURE CITED 159

LIST OF TABLES

Table		Page
1.1	The major Raman bands of carbon fibers	11
1.2	Material classification based on resistivity characteristics	15
2.1	Crystalline properties of carbon nanofibers	47
2.2	Textural properties of carbon nanofibers	63
3.1	Static decay time of pure LLDPE and its composites	71
3.2	Properties of carbon nanofibers	79
3.3	The crystallization temperatures (T_c), melting points (T_m), and heats of crystallization measured by DSC for LLDPE and its composites containing PRCVD, PR and MJ fibers	85
3.4	The relative area of melting peaks after deconcolution of DSC thermograms for LLDPE and its composites containing PRCVD, PR, and MJ fibers	87
4.1	Static decay time of pure V400P and MJ composites	107
4.2	Herman's orientation parameter for molecular alignment of pure V400P and its composites containing MJ fibers	116
4.3	Herman's orientation parameter for pure V400P, pure A950, and their composites containing PR fibers	126

LIST OF FIGURES

Figure Page

1.1 Schematic of CVD reactor for carbon nanofibers....4

1.2 Schematic representation of the catalytic growth of a carbon nanofiber using a gaseous carbon-containing gas....4

1.3 TEM and schematic presentations of (a) platelet, (b) herringbone, and (c) ribbon structure of carbon nanofibers....6

1.4 (a) High-resolution TEM image of a graphitized carbon nanofiber shows unusual morphological features of a graphitized carbon nanofiber. Various types of loops project from the outer and inner surfaces. (b) High-resolution TEM image shows one wall of a graphitized carbon nanofiber....9

1.5 Crystal structure of graphite showing ABAB stacking sequence and unit cell....11

1.6 TEM of (a) an as-grown fiber corresponding to a heat-treatment temperature of 1100°C and (b) a fiber heat treated to 2900°C....16

1.7 Mechanical properties of PP/carbon nanofiber composites as a function carbon nanofiber heat treatment temperature: (a) tensile strength and (b) tensile modulus....20

1.8 TEM micrograph of a pure LLDPE (ethylene/1-octene copolymer)....22

1.9 Optical micrograph of carbon fiber/HDPE composite. Transcrystallinity is observed on the surface of carbon fiber....22

1.10 Transcrystallinity of PP around carbon nanofibers in carbon nanofiber/PP composite. SEM micrograph was taken with a freeze fractured sample....23

1.11 Schematic of solid, liquid crystals and liquid phase....25

1.12 Molecular ordering with director....25

1.13 Schematic of as nematic, smetic and cholesteric phases....27

List of Figures (Continued)

Figure Page

1.14 Schematic of polymer phase 28

1.15 Chemical structures of monomers for TLCPs 31

1.16 WAXD pattern of an extruded sheet sample of HBA/HNA copolyester 32

1.17 (a) Schematic of pseudo-hexagonal phase of WAXD pattern and (b) radial (2θ) intensity profile in fibers of HBA rich copolymers (HNA:HBA=1:3) 34

1.18 (a) Schematic of orthorhombic phase of WAXD pattern and (b) radial (2θ) intensity profile in fibers of HNA rich copolymers (HNA:HBA=3:1) 35

1.19 The illustration of the exceptionally low permeability to water vapor and oxygen for TLCP (Vectran LCP) 37

2.1 Raman spectra of carbon nanofibers 46

2.2 X-ray diffractograms of carbon nanofibers 48

2.3 TGA profiles of various carbon nanofibers 50

2.4 Scanning electron micrographs of: (a) PR, and (b) MJ fibers 52

2.5 Scanning transmission electron micrographs of (a)PR, (b)MJ, (c)PRCVD, (d)MJCVD, (e)PRHT, and (f)MJHT fibers 53

2.6 Transmission electron micrographs of double layer structure of (a)PR, (b)PR, (c)PRCVD, (d)PRCVD, (e)PRHT, and (f)PRHT fibers. (b), (d), and (f) are in high resolution for (a), (c), and (e), respectively 55

2.7 Transmission electron micrographs of (a)MJ, (b)MJ, (c)MJCVD, (d)MJCVD, (e)MJHT, and (f)MJHT fibers. (b), (d), and (f) are in high resolution for (a), (c), and (e), respectively 57

2.8 SAED patterns of (a) PR and (b) PRHT fibers. The insets show the corresponding bright field images 60

List of Figures (Continued)

Figure Page

2.9 (a) N_2 adsorption-desorption isotherms and (b) pore size distributions of carbon nanofibers 62

3.1 Volume resistivity of pure LLDPE and its composites. Solid curves are trend lines 72

3.2 (a) Tensile modulus, (b) tensile strength, and (c) strain-to-failure of pure LLDPE and its composites 74

3.3 SEM micrographs of 15 wt% CNF/LLPDE composites containing: PRCVD, (b) PR, and (c) MJ fibers. The inset micrographs are at a higher magnification 77

3.4 TEM micrographs of 15 wt% CNF/LLPDE composites containing: PRCVD, (b) PR, and (c) MJ fibers 78

3.5 Histograms of diameter distribution of: (a) PRCVD (b) PR (c) MJ fibers 80

3.6 DSC thermograms (first heating) of pure LLDPE/ CNF composites at a heating rate of 10°C/min for: (a) PRCVD, (b) PR, and (c) MJ fibers 82

3.7 DSC thermograms (cooling) of pure LLDPE/ CNF composites at a heating rate of 10°C/min for: (a) PRCVD, (b) PR, and (c) MJ fibers 83

3.8 DSC thermograms (second heating) of pure LLDPE/ CNF composites at a heating rate of 10°C/min for: (a) PRCVD, (b) PR, and (c) MJ fibers 84

3.9 Representative deconvoluted thermograms (second heating) of pure LLDPE and its composites 88

3.10 DSC thermograms (second heating) of pure LLDPE at a heating rate of 10°C/min after various cooling rates (CR) 90

3.11 Avrami plots of pure LLDPE and 1 wt% composites containing PRCVD, PR, and MJ fibers 92

List of Figures (Continued)

Figure Page

3.12 Integrated azimuthal profiles (2θ plots) for: (a) pure LLDPE, and 1 wt% and 15 wt% MJ composites and (b) LLDPE/1 wt% composites containing PRCVD, PR and MJ fibers 94

3.13 Integrated azimuthal profiles (2θ plots) for: (a) pure LLDPE, and 1 wt% and 15 wt% MJ composites and (b) LLDPE/1 wt% composites containing PRCVD, PR and MJ fibers 96

3.14 Transmission electron micrographs of: (a) pure LLDPE, and LLDPE/15 wt% composites containing (c) PR-19, (e) PR-24 and (g) MJ fibers. (b), (d), (f), and (h) are in high resolution for (a), (c), (e), and (g), respectively 98

3.15 Histograms of thickness distribution of LLDPE lamellae in: pure, and 15 wt% nanocomposites containing (b) PRCVD, PR, and (d) MJ fibers 100

4.1 Volume resistivity of pure V400P and MJ composites 107

4.2 Tensile properties for pure V400P and MJ composites 109

4.3 The DSC thermograms for pure V400P and 15 wt% MJ composite at a rate of 20 °C/min 109

4.4 Wide angle x-ray diffraction patterns of molded samples from: (a) pure TLCP, (b) 0.1 wt%, (c) 1 wt% and (d) 5 wt% MJ composites..... 111

4.5 Wide angle x-ray diffraction patterns of extrudates from: (a) pure TLCP, (b) 0.1 wt%, (c) 1 wt% and (d) 5 wt% MJ composites..... 112

4.6 Radial (2θ) intensity profiles of molded and extruded samples from pure, 1 wt% and 5 wt% MJ composites 113

4.7 Azimuthal intensity profiles at 2θ = 19.8° of molded samples: pure V400P, 0.1 wt%, 1 wt% and 5 wt% MJ composites 115

4.8 Azimuthal intensity profiles at 2θ = 19.8° of extrudates from pure TLCP, 0.1 wt%, 1 wt% and 5 wt% MJ composites..... 117

List of Figures (Continued)

Figure Page

4.9 Radial (2θ) intensity profiles of extrudates for:
(a) pure TLCP, (b) 5 wt% MJ composites 119

4.10 Wide angle x-ray diffraction patterns of extrudates from:
(a) pure V400P, (b) 1 wt%, (c) 5 wt%, and (d) 10 wt% PR composites 122

4.11 (a) Radial (2θ) intensity profiles and (b) azimuthal intensity profiles
at 2θ ~ 19° of extrudates: pure V400P, 1 wt%, 5 wt%, and
10 wt% PR composites 123

4.12 Wide angle x-ray diffraction patterns of extrudates from:
(a) pure A950, (b) 1 wt%, (c) 5 wt%, and (d) 10 wt% PR composites..... 124

4.13 (a) Radial (2θ) intensity profiles and (b) azimuthal intensity profiles
at 2θ ~ 19° of extrudates: pure A950, 1 wt%, 5 wt%, and
10 wt% PR composites 125

4.14 SEM micrographs of pure V400P at various magnifications:
(a) 100, (b) 1K, (c) 1K, and (d) 10K 128

4.15 SEM micrographs of V400P/10 wt% PR fibers
at various magnifications: (a) 100, (b) 1K, (c) 10K, and (d) 30K 130

4.16 SEM micrographs of pure A950 at various magnifications:
(a) 100, (b) 1K, (c) 1K, and (d) 10K 131

4.17 SEM micrographs of A950/10 wt % PR fibers
at various magnifications: (a) 100, (b) 1K, (c) 10K, and (d) 20K 132

4.18 TEM micrographs of V400P at various magnifications:
(a) 15K, (b) 50K, (c) 100K, and (d) 300K 134

4.19 TEM micrographs of V400P/10 wt% PR fibers
at various magnifications: (a) 10K, (b) 50K, (c) 100K, and (d) 300K 137

4.20 TEM micrographs of A950 at various magnifications:
(a) 10K, (b) 50K, (c) 100K, and (d) 300K 138

4.21 TEM Micrographs of A950/10 wt% PR fibers
at various magnifications: (a) 10K, (b) 50K, (c) 100K, and (d) 300K 139

List of Figures (Continued)

Figure Page

A.1 A photograph of the ATS universal tensile tester 900 152

A.2 A photograph of the static decay meter 154

A.3 A photograph of the Megaohmmeter 155

A.4 A schematic of TEM 158

CHAPTER 1

INTRODUCTION

1.1 Introduction to nanocomposites

Polymers find significant application in the packaging industry due to their low gas and water permeability, and ease of processing. In 2003, the estimated world consumption of polymers in film was about 40 million tons [Pardos, 2004]. However, polymers can not be used in their unmodified state in electronics packaging because of their nonconductive nature. Therefore, polymer composites with conductive fillers have been developed to enhance their conductivity [Blythe, 1979]. For instance, carbon fillers have been incorporated into various polymers (such as polypropylene, polyethylene, poly(methyl methacrylate), poly(ethylene terephthalate), and polycarbonate) to improve their electrical and mechanical properties [Avella et al., 1996; Thongruang et al., 2002; Huang and Young, 1996; Vilcakova et al., 2002].

In 1999, Ijima reported the discovery of carbon nanotubes and their unique mechanical, thermal, and electrical properties [Ijima, 1999]. Since then, nano-scale carbonaceous materials such as carbon nanotubes (CNTs) and carbon nanofibers (CNFs) have been investigated [Thostenson et al., 2005]. This interest is natural since nano-scale size materials with dimensions on the order of 1-100 nm are crucial for nano-system, nano-electronics, and nano-structured materials [Thostenson et al., 2005]. Further, nanocomposites consisting of polymer matrices are being used for the fabrication of nano-scale devices because polymer nanocomposites provide superior processability.

Carbon-based nanocomposites are electrically conductive, and are used as housing materials for electrical devices to protect them from electromagnetic interference (EMI) and electrostatic discharge (ESD) phenomena. Compared to conventional carbon fibers or carbon black, a smaller amount of CNTs or CNFs is needed due to their nano-scale size and high aspect ratio (length over diameter). Further, it has been reported that select mechanical properties (such as tensile modulus) of polymers can be enhanced by the presence of CNFs [Kuriger et al., 2002].

However, polymer nanocomposites with CNT or CNF have been facing critical challenges: uniform dispersion and orientation of these reinforcements [Thostenson et al., 2005]. Due to very strong van der Waals bonding, CNTs or CNFs are often agglomerated, which hinders uniform dispersion. Orientation is important to maximize the effect of incorporation of CNT or CNF on mechanical properties of nanocomposites. However, it is difficult to make nano-scaled CNT or CNF aligned along preferred direction.

Further, the effect of nanofillers on crystalline and orientational structure of polymer matrix is critical to understand properties of polymeric composites with those nanofillers. Therefore, basic research is still necessary to understand polymer nanocomposites with nano-scale carbonaceous materials.

1.2 Carbon nanofibers (CNFs)

In the 1880's, a patent was given for the preparation of carbon filaments from iron and a hydrocarbon feed stock [Hughes et al., 1889]. Later on, transmission electron microscopy allowed researchers to investigate the growth mechanism and structure of

CNFs [Baker et al., 1972]. Also, the discovery of carbon nanotubes (CNTs) [Ijima, 1999] and the demand of nano-scale materials in industry has stimulated a significant research interest in CNFs [Rodriguez et al., 1995; Toebes et al., 2002; Li et al., 2005; Lim et al., 2005].

1.2.1 Synthesis of carbon nanofibers

Chemical vapor deposition (CVD) over a metal catalyst is one of the methods to produce CNFs. The CVD process is a controllable, cost-effective technique as compared to the arc-discharge and laser ablation methods [Toebes et al., 2002]. Furthermore, this technique has been adopted for large-scale production of carbon nanotubes [Tibbetts, et al., 2007]. CNFs have diameters on the order of 50-200 nm, which are relatively larger than that of CNTs (diameters are the order of 5-30 nm). The length of CNFs ranges from 1 to 100 μm. The primary advantage of CNFs over CNTs is their lower cost (~$0.2/g CNF vs. ~$20/g CNT) which is desirable in large-volume applications.

For batch-scale preparation of CNFs by CVD, powdered metal catalysts are precipitated from solution over substrate and then dried. Subsequently, they are calcined in air and reduced in a H_2/He flow. These catalysts are dispersed in a ceramic boat, which is in the center of a horizontal quartz reactor tube located in a furnace (Figure 1.1). A hydrocarbon source (such as methane, ethane, propane, natural gas, and carbon monoxide) is introduced into the reactor along with an inert gas.

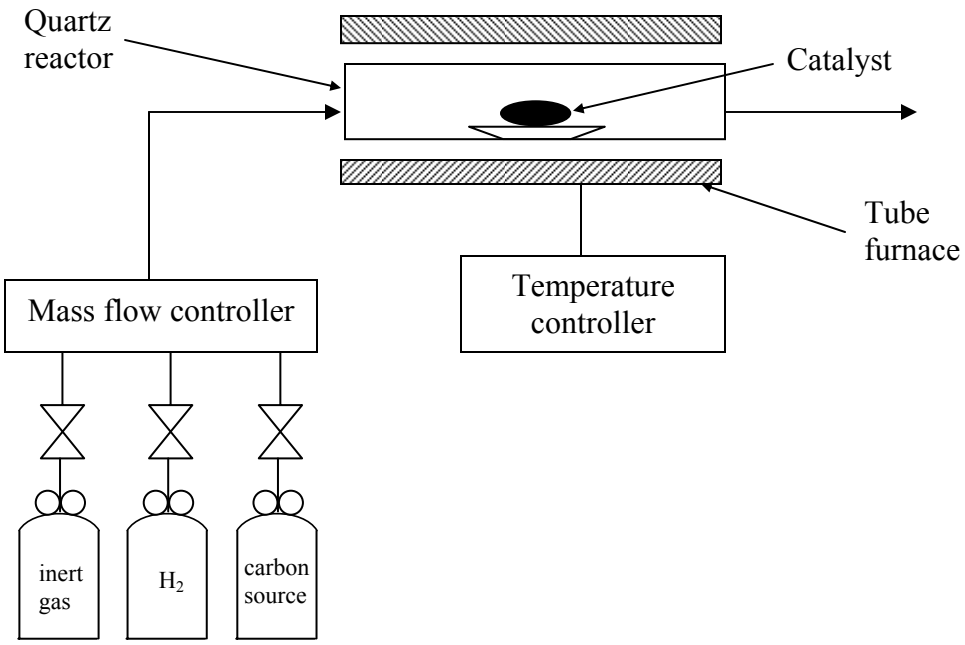

Figure 1.1. Schematic of CVD reactor for carbon nanofibers.

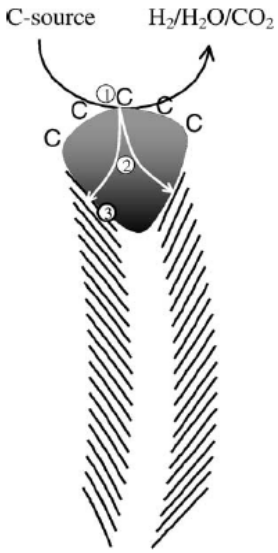

Figure 1.2. Schematic representation of the catalytic growth of a carbon nanofiber using a gaseous carbon-containing gas [Toebes et al., 2002].

During CVD reactions, the hydrocarbon is adsorbed and decomposed on the surface of catalyst, and carbon atoms diffuse through the catalyst particle. Finally, carbon in a fibrous structure form is precipitated on the other side of the catalyst [Baker et al., 1972; Rodriguez et al., 1995; Toebes et al., 2002]. Figure 1.2 shows a schematic representation of the catalytic growth of CNFs [Toebes et al., 2002].

It has been reported in the literature that morphology and crystalline structure of CNFs depends on the chemical nature of the catalyst and the conditions of the reactions [Rodriguez et al., 1995; Rodriguez et al., 1997; Li et al., 2005]. Rodriguez et al. [1995] synthesized three different types of CNF structures: platelet, herringbone, and ribbon. In the platelet structure, graphene layers are parallel to the fiber axis (Figure 1.3a). These CNFs were prepared by decomposition of CO/H_2 (4:1) over iron catalyst at 600°C. Figure 1.3b displays the herringbone structure, where graphene layers were inclined to the fiber axis with a solid core. The decomposition of C_2H_4/H_2 (4:1) over iron-copper (7:3) catalyst at 600°C produced this structure. Finally, they reported that graphene layers aligned perpendicular to the fiber axis (ribbon structure) by the decomposition of CO/H_2 (4:1) over silica supported iron at 600°C (Figure 1.3c).

Further, modified platelet and herringbone structures have also been reported [Rodriguez et al., 1997; Li et al., 2005]. Helical conformation was prepared by the decomposition of C_2H_6 over iron-nickel (8:2) catalyst at 815°C [Rodriguez et al., 1997]. Herringbone structured CNFs, with a hollow core, were grown in a mixed flow CO/H_2 (4:1) over $Fe/\gamma\text{-}Al_2O_3$ catalyst system at 600°C [Li et al., 2005].

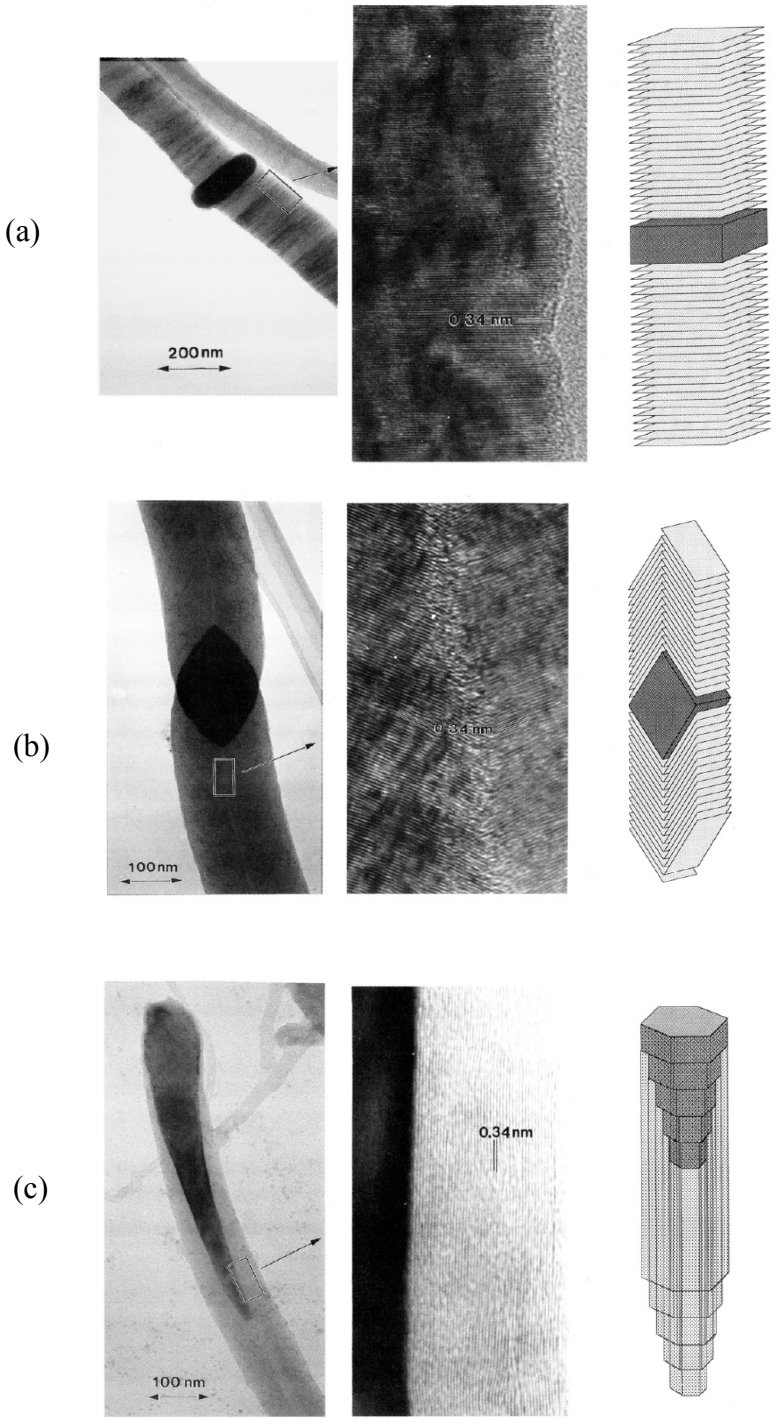

Figure 1.3. TEM and schematic presentations of (a) platelet, (b) herringbone, and (c) ribbon structure of CNFs [Rodriguez et al, 1995].

Thus, it is noted that a suitable combination of metal catalyst, carbon precursor, and thermal energy makes it possible to selectively synthesize various types of carbon nanofibers.

1.2.2 Modification of carbon nanofibers

Further processing, such as non-catalytic CVD, oxidation, carbonization, and graphitization can modify the surface and crystalline structure of CNFs. The diameter of CNFs increases by the non-catalytic CVD, which is the deposition process of amorphous carbon on the surface of CNFs [Lakshminarayanan et al., 2004].

It has been reported in the literature that as-grown CNFs are hydrophobic [Toebes et al., 2004]. Thus, oxygen-containing groups such as carboxylic and carbonyl groups have been introduced by liquid phase oxidative treatment on the surface of CNFs. These functional groups make CNFs hydrophilic and their surface more reactive [Lakshminarayanan et al., 2004; Toebes et al., 2004; Ros et al., 2002; Shaikhutdinov et al., 1995]. An advantage of liquid phase oxidative treatment is that pitting and degradation of CNFs is less than that afforded by gas phase oxidative treatment. By acid treatment with aqueous solutions of HNO_3, or mixture of HNO_3 and H_2SO_4, an increase of oxygen content and acidic surface groups was observed. However, acid treatment did not affect the crystalline structure of CNFs [Toebes et al., 2004; Ros et al., 2002] even though an increase of surface area [Lakshminarayanan et al., 2004] (20-25 to 41-73 m^2/g) and roughness of surface [Shaikhutdinov et al., 1995] of CNFs were found due to oxidative treatments.

Carbonization and graphitization processes are essentially heat treatment of carbonaceous materials. By definition, carbonization implies heat treatment at temperatures of 1700°C or less, whereas graphitization refers to heat treating to higher temperatures [Buckley and Edie, 1992]. It should be noted that in most cases, CNFs are produced below 1000°C. Graphite is an extremely stable form of carbon. However, CNFs possess defects and their structure is irregular. When higher temperatures are applied to the CNFs, reorganization occurs to convert them into the more stable graphitic structure. During heat treatment, topological changes of CNFs have been observed [Kim et al., 2001]. It was concluded that the morphological change at the micrometer scale from a smooth surface, to a rope-like structure, on to a grain-like structure, was closely related with the volume change. Further, a structural transformation from turbostratic to a three dimensional graphite was shown in the graphitization process of CNFs [Lee et al., 2001]. Endo et al. reported that the formation of energetically stable loops between adjacent graphene layers form the unstable edge planes in both the outer surface and the inner hollow core (Figure 1.4) [Endo et al., 2003].

1.2.3 Analysis of carbon nanofiber

Scanning electron microscopy (SEM) and transmission electron microscopy (TEM) (Figure 1.4) have been widely used to observe micro- and nano-scaled structure of CNFs. Recently, *in situ* TEM images and movies revealed how carbon nanofibers grow on the surface of a nickel catalyst [Helveg et al. 2004].

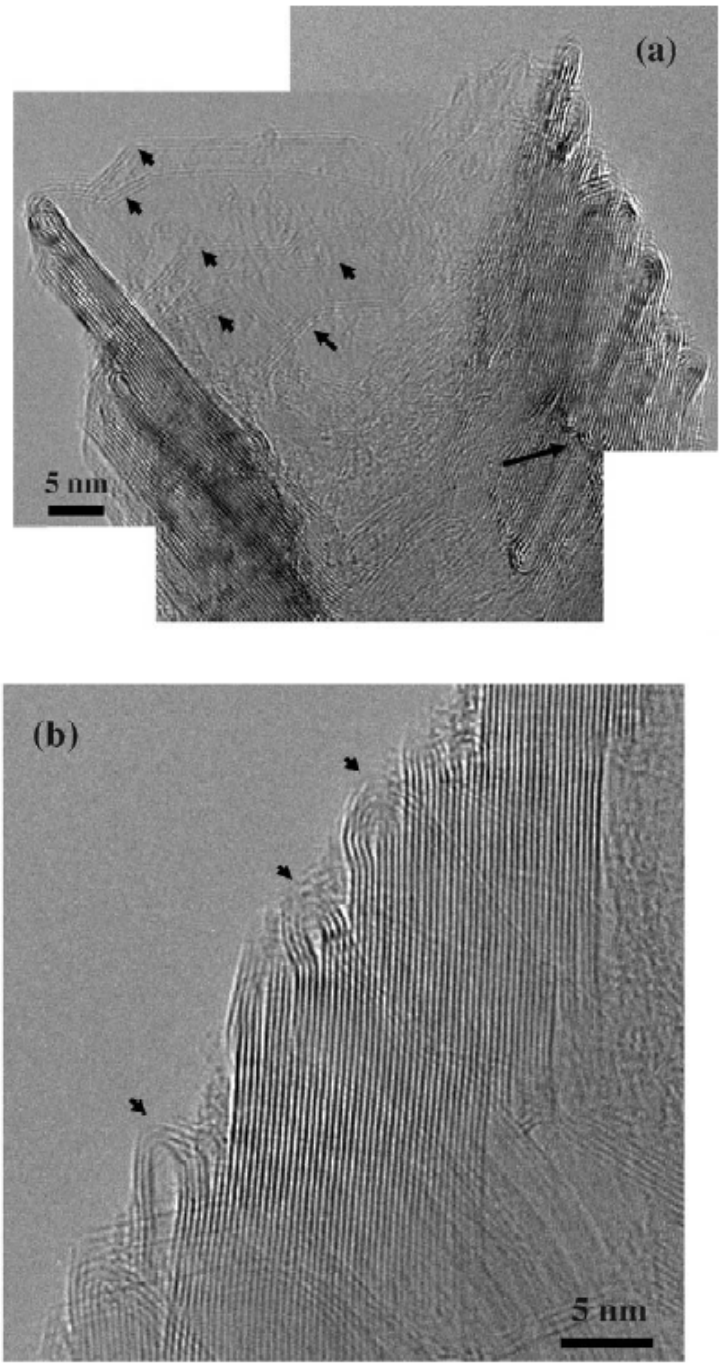

Figure 1.4. (a) High-resolution TEM image of a graphitized carbon nanofiber shows unusual morphological features of a graphitized carbon nanofiber. Various types of loops project from the outer and inner surfaces. (b) High-resolution TEM image shows one wall of a graphitized carbon nanofiber. [Endo et al., 2003].

Also, using X-ray diffraction and Raman spectroscopy, the crystalline structure of CNFs has been investigated [Pierson, 1993].

Hexagonal packing is the most common crystalline form of graphitic carbonaceous materials. The stacking sequence with a -ABABAB- stacking order can be displayed by carbon atoms, which are superimposed over each other in every other layer as shown Figure 1.5 [Pierson, 1993]. This graphite structure is reflected as the (002), (100), and (101) planes in an X-ray diffractogram. In addition, the average values of the degree of orientation, interlayer spacing (d_{002}), crystallite thickness (L_c), and crystallite width (L_a) can also be observed from wide angle X-ray diffraction. The orientation of the graphene layers can be calculated from an azimuthal scan at the fixed Bragg position of (002) reflection. The full-width-half-maximum of the intensity, Z, or Herman's orientational order parameter [$f = 0.5\ (3\langle\cos^2\varphi\rangle-1)$] is used to quantify the degree of orientation of the graphene layers. The d_{002} is obtained from the peak position of (002) reflection in radial (2θ) intensity profile using Bragg's law ($2d\sin(\theta)=n\lambda$). Further, 2θ scan is used to estimate the values of L_c and L_a from the (002) and (100) peaks, respectively.

Carbon can exist in a wide range of disordered forms. Raman spectroscopy is one of powerful tools used for investigating carbonaceous materials since it is sensitive to these structures and to changes that perturb the translational symmetry [Jawhari et al., 1995].

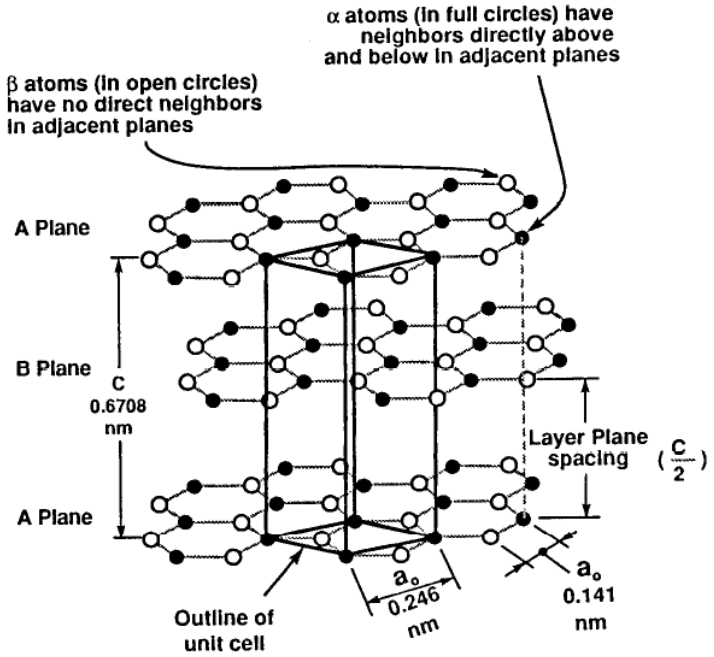

Figure 1.5. Crystal structure of graphite showing ABAB stacking sequence and unit cell [Pierson, 1993].

Table 1.1 The major Raman bands of carbon fibers [Melantis et al., 1996]

	D band	G band	D' band	G' band
Peak (cm^{-1})	1350-1370	1575-1582	~1620	2690-2730
Present in	poorly graphitized fibers. disappeared at higher graphitization temperatures.	single graphite crystal and all carbon fibers	non-graphitized fibers. Detected as a shoulder of the G band in higher graphitization temperatures.	crystalline graphite and graphitized fibers.
Attribute to	the breakdown of the lattice symmetry of the graphite cell and assigned to the A_{1g} vibration mode of the graphite plane, introduced by small crystal size and structural disorder	the vibrational mode E_{2g} of the graphite cell	disorder and small crystallite size. It disappears at well-graphitzed fibers	overtone of the D band

This frequency range can be divided into two regions: the first-order region (0-1650 cm^{-1}) and the second–order region (1650-3300 cm^{-1}) as the fundamental and overtone/combination frequencies, respectively [Melantis et al., 1996]. Various Raman bands (D, G, D', and G') are noticeable in experimental Raman studies of carbon fibers, and designations of these bands are summarized in Table 1.1 [Melantis et al., 1996].

Other bands have been also reported in the literature. A broad band at 1500-1550 cm-1 is associated with amorphous forms of carbon [Nikiel and Jagodzinski, 1993; Jawhari et al., 1995]. Keller et al. communicated that bands at 1175 cm^{-1} indicated the presence of basic C=O functional groups [Keller et al., 2002]. Among Raman bands, the spectrum between 1300 cm^{-1} and 1650 cm^{-1}, such as D and G bands, is important because the integrated intensity ratio of I_D/I_G is inversely proportional to crystallite width (L_a) ($L_a=44[I_D/I_G]^{-1}$) [Knight and White, 1989; Nikiel and Jagodzinski, 1993; Jawhari et al., 1995; Wang et al., 2003; Li et al., 2005].

1.3 Carbon nanofibers based nanocomposites

Heremans reported that the intrinsic resistivity of carbon nanofibers was 2×10^{-3} Ω-cm [Heremans, 1985]. One of commercial CNFs (Pyrograph III®) exhibited 4×10^{-3} Ω-cm [Finegan and Tibbetts, 2001] or 55×10^{-3} Ω-cm [Guillemo and Jana, 2006; Applied Science Inc., 2006]. Tensile strength and modulus were in range of 2.0-7.0 and 100-680 GPa, respectively [Jacobsen, 1995; Kuriger, 2002; Guillemo and Jana, 2006]. Most of these reported values in literature were measured indirectly, since it is not easy to measure such intrinsic properties of CNFs due to their small size. It is known that CNFs

exhibit good electrical conductivity and possess excellent mechanical properties. Therefore, the research objectives of this study focused on improving electrical and mechanical properties of polymeric matrix nanocomposites. Two different types of polymers have been used as matrices: flexible chain and semi rigid-rod polymers.

It is noted that the majority of referenced studies in this chapter consider melt mixing as the technique for composite fabrication. In terms of dispersion and breaking of CNFs, in-situ polymerization or solvent casting may be preferred. However, melt mixing, such as batch mixing and extrusion, is more conventional and compatible for existing polymer melt processes.

1.3.1 Electrical properties of carbon nanofibers based nanocomposites

Typically, pure polymers have a high volume resistivity (>10^{12} Ω-cm) [Sperling, 2001]. Incorporation of conductive fillers such as CNFs can render the composite electrically conductive. However, unless enough CNFs are added into the polymer matrix to form a network of CNFs, volume resistivity does not decrease significantly. As the volume fraction of CNFs increases, the distance between CNFs is small enough to make a CNF network and allow electrons to tunnel or hop. This is the transition region, called the percolation threshold, in which electrons can pass through composites resulting in a significant decrease in volume resistivity. Table 1.2 describes materials classified by their resistivity characteristics. Lozano et al. reported that the percolation threshold for PP/CNF (Pyrograf-III^{TM}, PR-24) composites (produced using a Haake internal mixer) was observed at 9-18 wt%, and the volume resistivity for samples containing 18 wt%

CNF was ~10^8 Ω-cm [Lozano et al., 2001]. The CNFs used by Lozano et al. were purified and functionalized. Hammel et al. used two CNFs (Electrovac nanofibers, ENF®) with different diameters (100 nm and 200 nm) for preparing PP/CNF composites using a DACA Microcompounder (DACA Instruments, Goleta, USA) [Hammel et al., 2004]. The average length for both CNFs was approximately 10 μm. They reported that volume resistivity for PP/CNF (200 nm) composites was 4×10^6 Ω-cm with 18 wt% CNF content whereas PP/CNF (100 nm) composites showed 10^6 Ω-cm with 10 only wt% CNF content, indicating that aspect ratio (length over diameter) is critical for electrical properties in CNF based composites.

Table 1.2 Material classification based on resistivity characteristics

Material type	Volume resistivity (Ω-cm)	Characteristics
Insulative	$\geq 1\times10^{11}$	These materials prevent or limit the flow of electrons across their surface or though their volume. Static charges remain in place on these materials for a very long time.
Electrostatic dissipative	$\geq 1\times10^{4}$, $<1\times10^{11}$	Charges flow to ground more slowly and in a somewhat more controlled manner than with conductive materials.
Conductive	$<1\times10^{4}$	Electrons easily more across the surface or through the bulk of these materials.
Electromagnetic interference shielding	$<1\times10^{3}$	For ESD-sensitive devices, these materials provide Faraday cage protection from energy transfer.

Thermally modified CNFs have been incorporated to enhance electrical properties of composites. PR-19-HT CNFs (Applied Science, Inc.) graphitized at 3000°C were incorporated into PP to measure volume resistivity [Kuriger et al., 2002]. Resistivity as low as 20 Ω-cm was achieved with approximately 18 wt% CNF content. This is due to an increase of intrinsic conductivity of CNFs after graphitization. Howe et al. investigated the effect of heat treatment of CNFs on PP/CNF (Pyrograf-III^{TM}, PR-19) composites [Howe et al., 2006]. It was evident that as heat treating temperature increased, the d_{002} decreased and L_c increased, indicating a higher graphitic content of CNFs, which resulted in an increase of intrinsic conductivity. However, they observed, using TEM, that with

heat treatment to 2900°C, fibers were converted into short nested conical crystallites (Figure 1.6), which reduced electrical transport properties.

Hine et al., incorporated CNF (Pyrograf-III^{TM}, PR-19) into PP using a Prism Eurolab twin screw extruder [Hine et al., 2005]. After mixing, in order to measure the fiber length in composites, samples were burned off at 450°C for 2 hr. They observed a significant decrease in fiber length from 20-100 μm (from manufacturer) to 2.53±1.5 μm. To reduce this fiber breaking effect during fabrication of composite by melt mixing, Guillermo and Jana used chaotic mixing for PMMA/CNF composites, which could produce lower shear stress compared to a conventional internal mixer [Guillermo and Jana, 2006]. They reported that a nominal size of particle agglomerates in chaotic mixing was bigger than that in internal mixing. Further, longer fibers were also found in chaotic mixing. They concluded that this chaotic mixing resulted in a percolation threshold at ~2 wt% CNF content (~10^6 Ω-cm), whereas composites produced by internal mixing led to a percolation threshold of 6 wt% CNF (10^6 Ω-cm) [Guillermo and Jana, 2006].

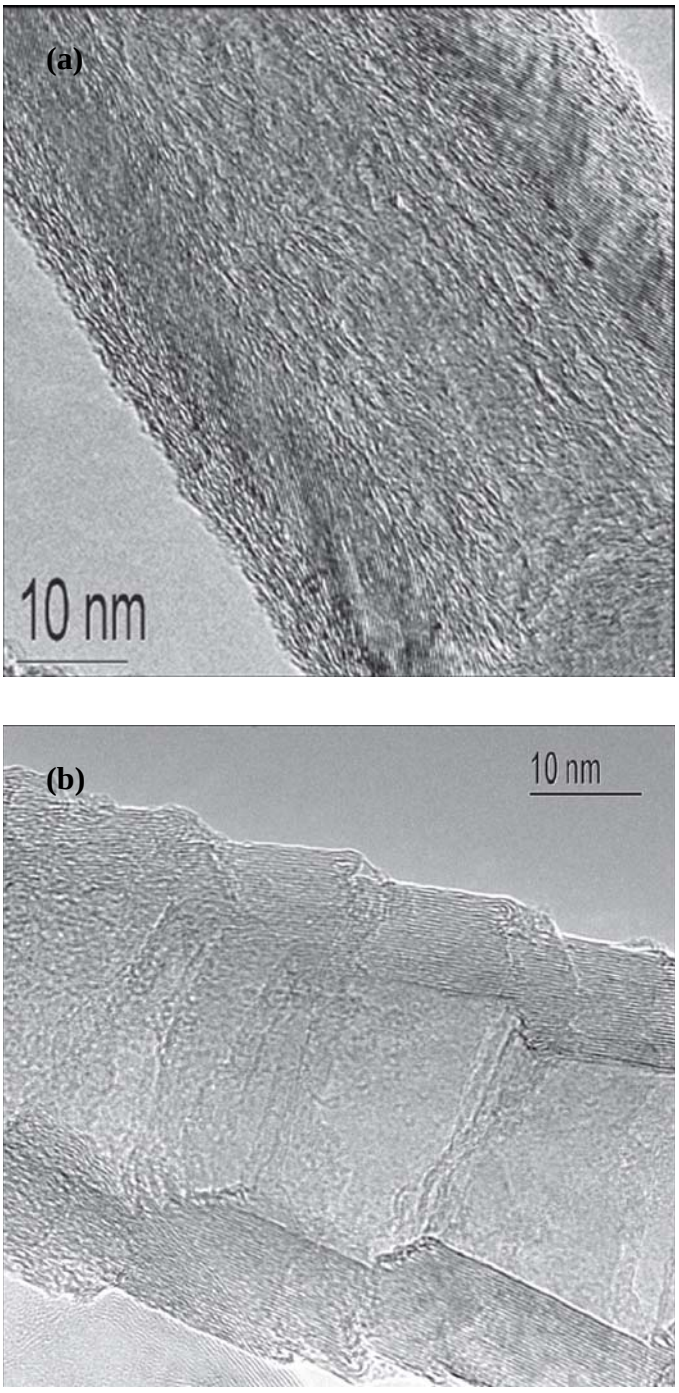

Figure 1.6. TEM of (a) an as-grown fiber corresponding to a heat-treatment temperature of 1100°C and (b) a fiber heat treated to 2900°C [Howe et al., 2006].

1.3.2 Mechanical properties of carbon nanofibers based nanocomposites

Orientation of CNFs affects the performance of nanocomposites, especially the mechanical properties. It is very difficult to have aligned fibrous nanofillers along a preferred composite flow direction due to their discontinuity and nano-scale dimension. Therefore, although tensile modulus has been found to increase with CNF-reinforced composites with various polymers, a significant increase of tensile strength has not been observed [Kumar et al., 2002; Ma et al., 2003; Zeng et al., 2004].

It has been reported [Kumar et al., 2002] that the fibers spun from 5 wt% CNF (Pyrograf-III^{TM}, PR-21) with PP, using melt spinning equipment showed an increase of the modulus and compressive strength over pure PP by 50% and 100%, respectively. However, there was only a small increase in tensile strength and almost 30% decrease in elongation at break [Kumar et al., 2002]. With melt-spun fibers of poly(ethylene terephthalate) (PET) containing 5 wt% of CNF (Pyrograf-III^{TM}, PR-24), Ma et al. observed insignificant increase in tensile modulus [Ma et al., 2003]. However, a decrease in tensile strength and elongation at break was observed. Zeng et al., reported that 5 and 10 wt% of CNFs (Pyrograf-III^{TM}, PR-21 and PR-24) with a fiber length of 60 μm were incorporated into poly(methyl methacrylate) using a twin screw extruder [Zeng et al., 2004]. Tensile modulus increased by 50% as compared to pure PMMA. However, a decrease of 20 and 35% was observed in tensile strength and elongation at break, respectively.

Kuriger et al. reported that an improved tensile strength of PP/CNF composites was observed with increase of the degree of CNF (Pyrograf-III^{TM},PR-21 and PR-19)

orientation [Kuriger et al., 2002]. They also determined electrical resistivity of strands and sheet type composites. Due to the additional misalignment of fibers, sheets showed low electrical resistivity. This indicates that a high degree of CNF orientation is not preferred for electrical properties.

Another factor that affects mechanical properties of composites is interfacial bonding between nanofillers and polymers. When composites are stretched, the load is transferred from matrix to nanofiller. Therefore, a strong bonding is particularly essential for tensile strength and elongation at break. It is known that an insignificant improvement in tensile strength and a decrease in elongation at break in composites result from poor bonding associated with defects at the interface [Choi et al., 2005; He et al., 2005]. Hence, work on surface modification of CNFs has been done toward enhancing the interfacial bonding with polymers [Brandl et al., 2004; Finegan et al., 2003; Howe et al., 2006].

CNFs were plasma treated in order to introduce oxygen containing functional group which increased CNF hydrophilicity [Brandl et al., 2004]. Composites with 5 wt% CNFs in PP were prepared using twin screw extrusion and injection molding. In mechanical testing, an increase in tensile modulus and strength by up to 49 and 19 wt%, respectively, was observed. Finegan et al. prepared air-etched fibers after oxidation in air at 450°C for 16 min [Finegan et al., 2003]. Adhesion between CNF and PP was enhanced due to an increase of surface area and surface energy of CNFs. They also varied feedstock residence time during synthesis of CNFs, and lower feedstock residence times led to more graphitic fibers which displayed poorer adhesion to PP. Howe et al. reported the effect of heat treating CNFs on mechanical performance of composites with PP

[Howe et al., 2006]. Short nested conical crystallites formed after heat treatment at 2900°C (Figure 1.6) resulted in reduced tensile strength and modulus. It was observed that optimal mechanical properties resulted when CNFs were treated at 1500°C (Figure 1.7).

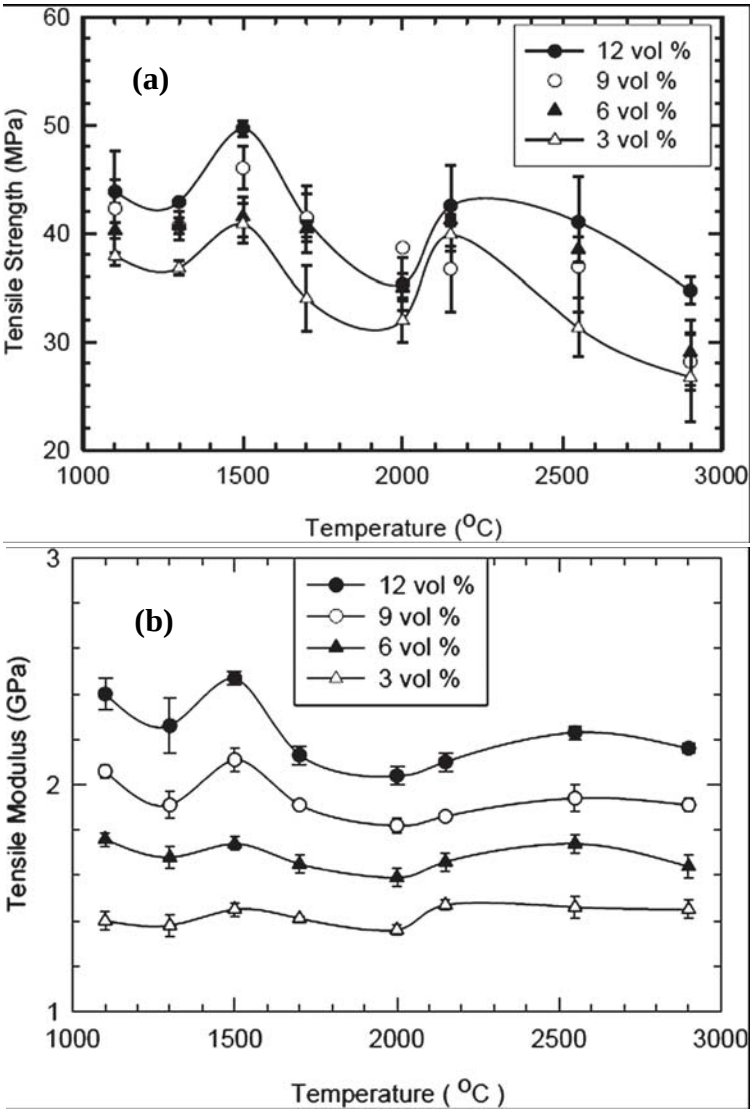

Figure 1.7. Mechanical properties of PP/CNF composites as a function CNF heat treatment temperature: (a) tensile strength and (b) tensile modulus [Howe et al., 2006]

1.3.3 Polymer crystalline structure in carbon nanofibers based nanocomposites

As described above, there is significant interest in carbon nanofiber based nanocomposites obtained from semi-crystalline flexible polymer matrices such as PE and PP. These polymers have lamellar structures, which can be represented by crystalline lamellae and amorphous regions stacked alternatively. TEM has been used for observing lamellar structure of PE and PP [Defoor et al., 1992; Schmitt, 2000; Feng et al., 2002; Marega et al., 2003; Muller et al., 2003] (Figure 1.8). Samples were prepared by cryo-microtoming and staining with chlorosulfonic acid [Defoor et al., 1992; Schmitt] or Ruthenium tetroxide [Feng et al., 2002; Marega et al., 2003; Muller et al., 2003].

When fibers are incorporated into semicrystalline polymers, they act as nucleating agents, and crystallization occurs along the interface between fibers and polymer. Nuclei of polymers can not grow laterally due to a dense nuclei density on the fiber surfaces. As a result, most nuclei grow perpendicularly to the fiber surfaces, resulting in transcrystalline layers [Quan et al., 2005]. This is important to understand fiber/polymer interfaces, which affect mechanical performance of composites. Transcrystallinity has been observed with composites based on carbon fibers [Mironov et al., 2002], where transcrystalline lamellae of high density polyethylene (HDPE) grew on the surface of CFs (Figure 1.9).

In study of CNFs based polymer composites, an increase of crystallization temperature was found using DSC, confirming the role of CNFs as nucleating agents [Lozano and Barrera, 2001]. However, there are few literature studies that report on the polymer crystalline structure in composites (Figure 1.10) [Hine et al., 2005].

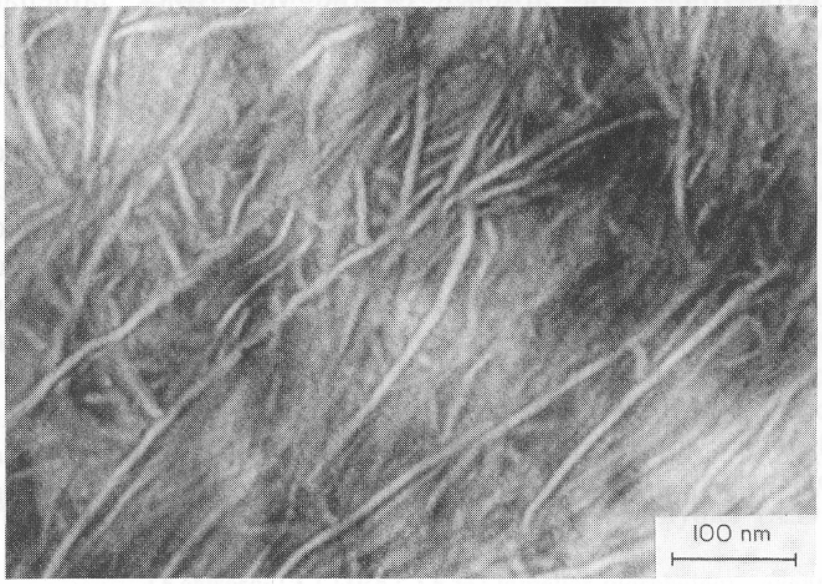

Figure 1.8. TEM micrograph of a pure LLDPE (ethylene/1-octene copolymer) [Defoor et al., 1992].

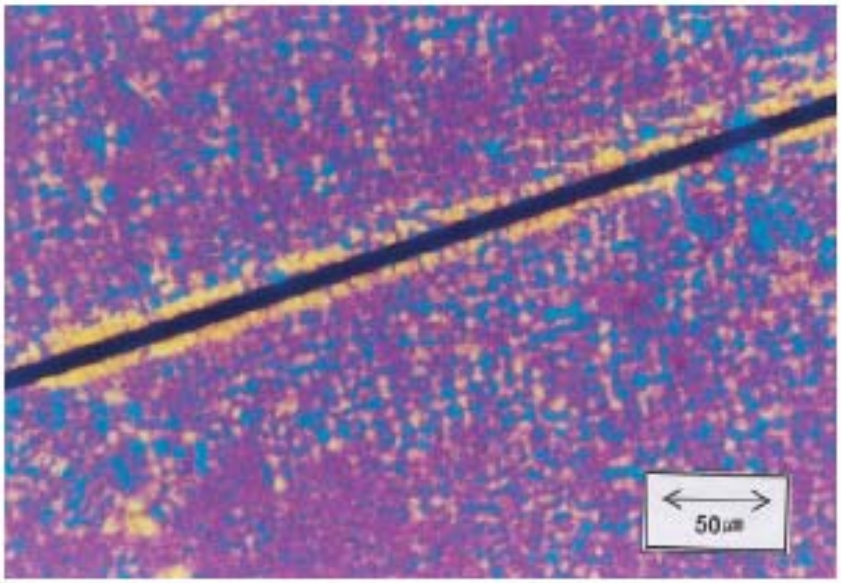

Figure 1.9. Optical micrograph of carbon fiber/HDPE composite. Transcrystallinity is observed on the surface of carbon fiber [Mironov et al., 2002].

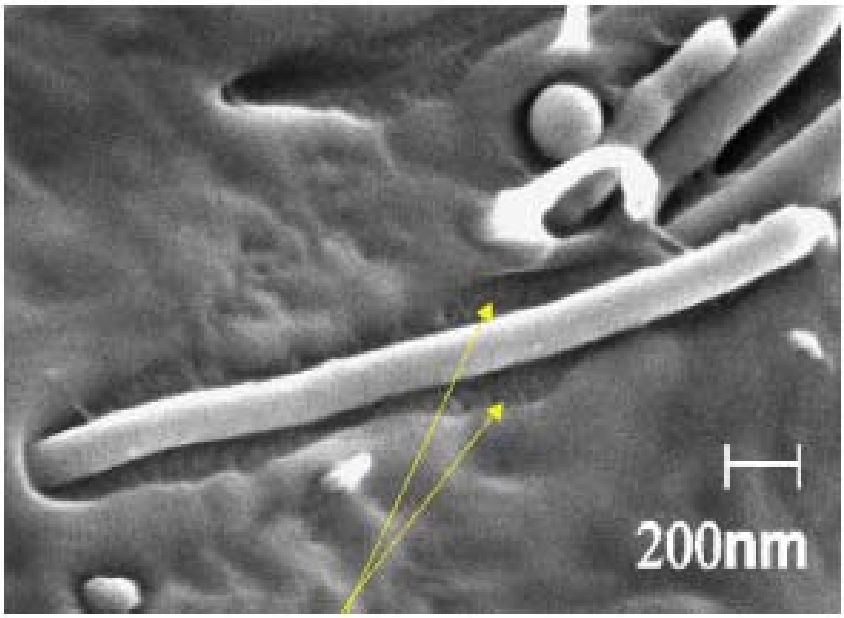

Figure 1.10. Transcrystallinity of PP around carbon nanofibers in carbon nanofiber/PP composite. This SEM micrograph was taken of a freeze fractured sample [Hine et al., 2002].

1.4 Liquid crystalline polymers (LCPs)

In this section, liquid crystalline polymers and their composites with carbonaceous materials will be reviewed. Liquid crystals are defined as substances that exhibit long-range order in one or two dimensions. Solid crystals are ordered in all three dimensions whereas liquids are entirely disordered [Sperling, 2001]. The liquid crystalline state, discovered by Friedrich Reinitzer in 1888, was found with cholesteryl benzonate. It was reported that it melted from a solid to a cloudy liquid at 145.5°C and then a cloudy liquid changed to a clear liquid at 178.5°C [Reinitzer, 1888]. Lehman [Lehman,1890] described the new phase as the liquid crystalline or mesomorphic phase. Since then, a large number of liquid crystalline materials have been synthesized, and their characteristics have been studied [Kelker and Hatz, 1980; Chung, 2001; Tjong, 2003].

Crystalline order can be described by positional order and orientational order. In other words, molecules occupy certain positions in lattice sites and orient themselves in specific directions. As temperature increases, the solid state changes into a liquid state and then both the position and orientation order are destroyed. However, in some materials, between solid state and liquid state, there is liquid crystalline phase, which possesses orientational order but no (or little) positional order (Figure 1.11). This means that in liquid crystalline phase, molecules orient along a preferred direction known as a director (Figure 1.12) [Tjong, 2003].

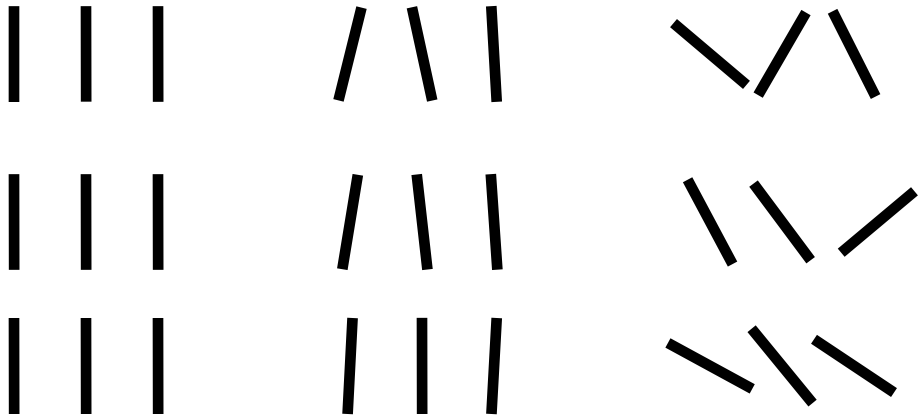

Figure 1.11. Schematic of a solid, liquid crystal, and liquid phase [Tjong, 2003].

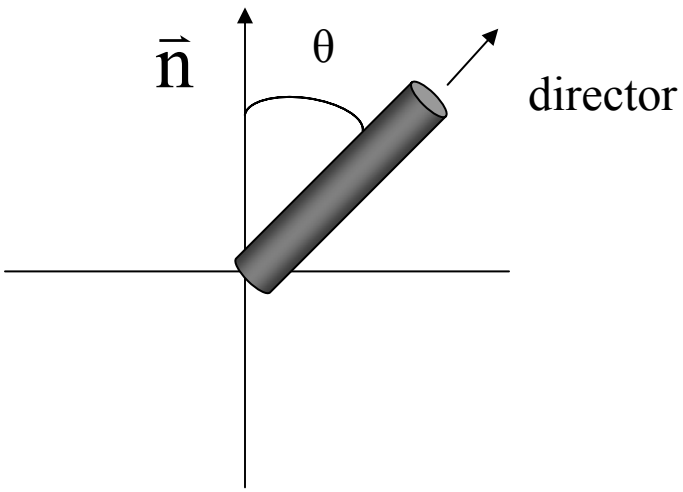

Figure 1.12. Molecular ordering with director [Tjong, 2003].

Depending on molecular ordering, liquid crystals are classified as nematic, smectic and cholesteric (Figure 1.13) [Freidel, 1922]. The nematic phase has orientational order but no long-range position order. When the nematic phase is more arranged as a layered structure, the smectic phase is formed with positional ordering in one dimension. There are two common smectic phases depending on orientational correlation between the director of molecules and a layer plane. The smectic A phase exhibits perpendicular director of molecule into the layer plane whereas the director and a layer plane has some angle in the smectic C phase. The cholesteric phase can be simply described as a helical nematic layer structure. This phase consists of a stack of nematic layers for which the director changes from one layer to another.

Liquid crystalline behavior can be observed in both molten and solution states [Sperling, 2001]. The lyotropic state is liquid crystallinity in a solution above a certain concentration. The thermotropic state is liquid crystallinity in the melt phase above certain temperature. Several literature studies report on synthesizing and developing liquid crystalline polymers (LCPs) since they possess unusually high mechanical properties (i.e., strength and stiffness), good chemical resistance and a low thermal expansion coefficient [Han and Bhowmik, 1997]. These synthetic LCPs exhibit liquid crystalline characteristics described, i.e., intermediate between crystalline phase and amorphous phase (Figure 1.14) [Wu and Schultz, 2002]. This intermediate state can be close to a poor crystalline structure, or on the other hand, close to an oriented amorphous structure with no long-range position. In polymers, the liquid crystalline phase is formed

by the presence of mesogenic monomer units [Tjong, 2003]. These units can be in the main chain or the side-chain of LCPs backbone [Donald and Windle, 1992].

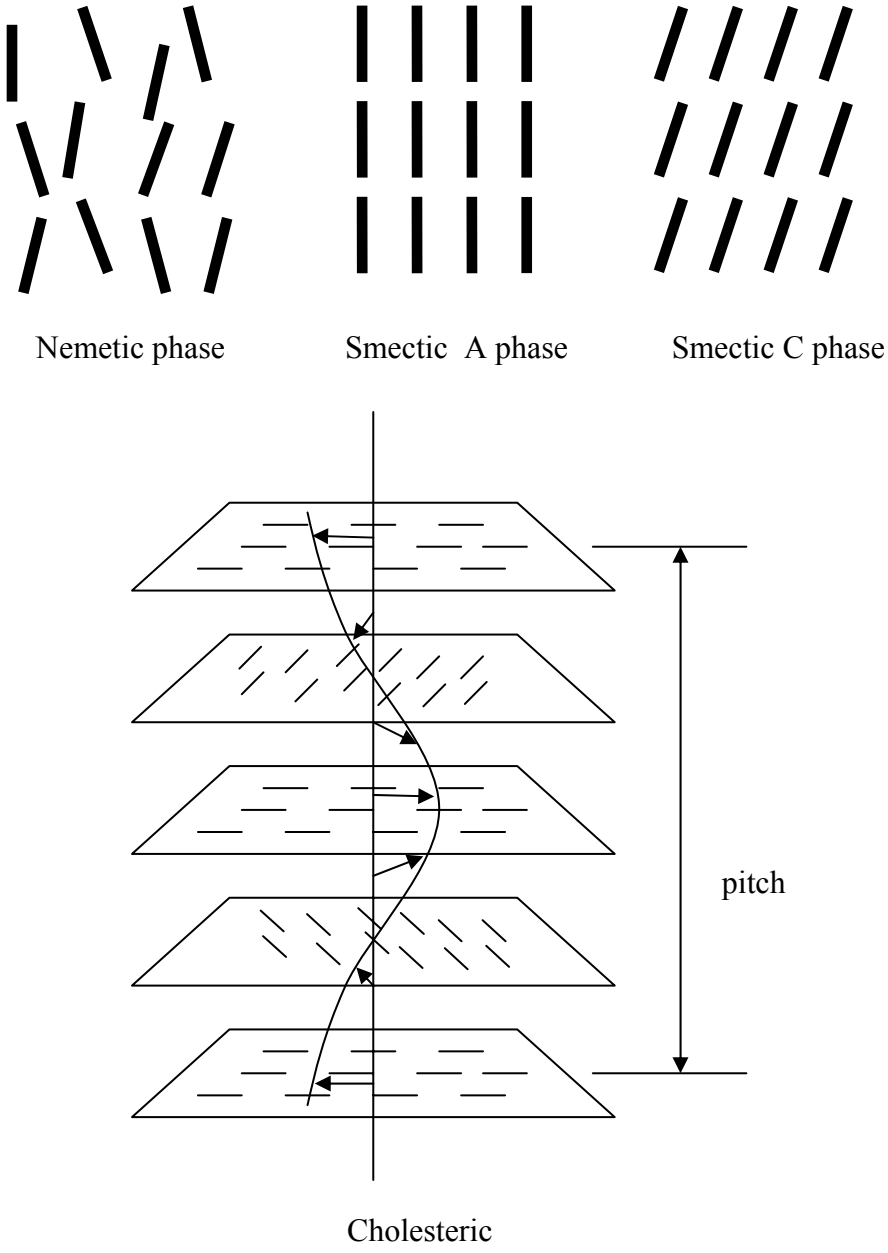

Figure 1.13. Schematic of nematic, smectic and cholesteric phases [Tjong, 2003].

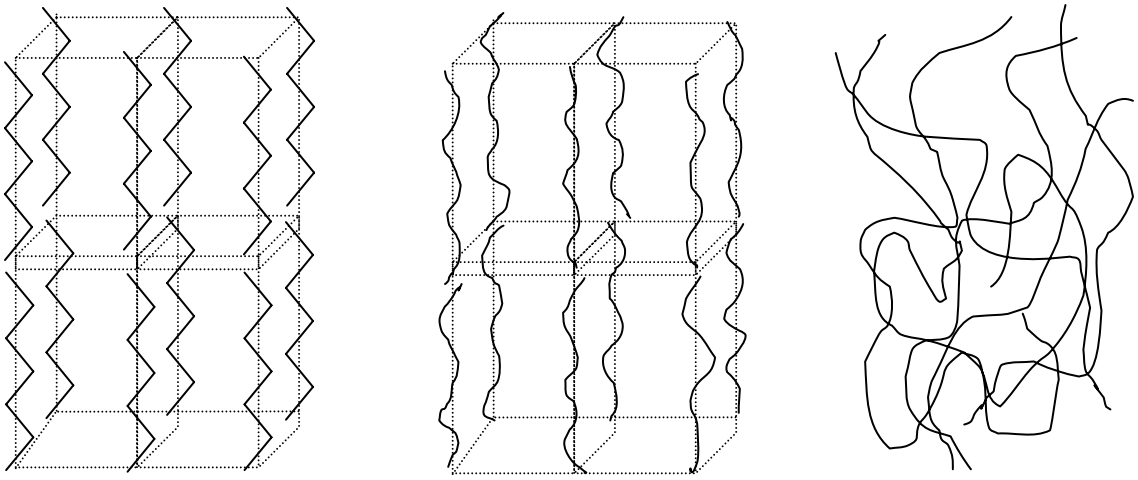

Figure 1.14. Schematic of polymer phases [Wu and Schultz, 2002]

1.4.1 Thermotropic liquid crystalline polymers (TLCPs)

Typically, a very strong solvent is needed for processing lyotropic LCPs, and the solvent removal process limits its application. For example, “Kevlar” developed in 1965 by DuPont as a commercial lyotropic LCP, is spun from a concentrated sulfuric acid solution. In contrast, in terms of processability, thermotropic LCPs are preferred since they can be processed by conventional melt processes such as blown film, cast film and melt-spinning processes.

In the 1970s, chemical companies such as Carborundum, Eastman-Kodak, Celanese, Amoco, and DuPont developed and commercialized TLCPs due to their melt processability, good mechanical properties, low moisture up-take, and excellent thermal and chemical resistance [Chung, 2001]. “Ekkcel I-2000” by Carborundum was an aromatic copolyester based on a biphenol monomer. Eastman-Kodak synthesized an aromatic-aliphatic copolyster (X7G). “Vectra” is a copolyster based on 1,4-hydroxybenzoic acid and 2,6-hydroxynaphthalene acid [Chung, 2001].

The melting temperature of thermotropic LCPs (TLCPs) with mesogenic units in the polymer backbone is relatively high; 430°C and 440°C for the hydroxybenzoic acid homopolymer and hydroxynaphthalene acid homopolymer, respectively [Langelaan and Posthuma de Boer, 1996]. Modified TLCPs have been developed with a lowered melting temperature. From a thermodynamic point of view, where melting temperature is determined by entropy and enthalpy changes during melting, high melting temperatures result from low melting entropy.

$$T_m = \frac{\Delta H}{\Delta S}$$

Therefore, increasing entropy change or decreasing enthalpy change can reduce melting temperature. An enthalpy change decreases by disrupting crystal structure of thermotropic LCPs, which have rigid mesogenic units. Introducing either flexible spacers, links with more freedom, or bulky side-groups or chains that provide less chemical

regularity related with molecular packing, can disrupt thermotropic LCPs structure [Donald and Windle, 1992].

There are homopolymers that exhibit the characteristics of thermotropic LCPs. Such polymers are synthesized from terephthalic acid (TA), 1,4-hydroxybenzoic acid (HBA), and hydroquinone (HQ) (Figure 1.15). As expected, these homopolymers have very high melting temperature for conventional process. Copolymerization is one of the modifications done to LCP structure to lower melting temperature by incorporating other mesogenic monomers randomly [Tjong, 2003].

For commercially available thermotropic LCPs, the aromatic rings of the above monomers have been replaced by naphthalene or biphenyl units during copolymerization with 2,6-dihydroxynaphthalene (DHN), 2,6-hydroxynaphthalene acid (HNA) or 2,6-naphthalene dicarboxylic acid (NDA) (Figure 1.15) [Tjong, 2003]. Thus, copolymers are composed of molecules with rigid and flexible monomeric unit. The rigid part (the mesogenic monomer) imparts high thermal and mechanical properties, while the flexible monomers contribute to processibility. For example, Celanese has developed and commercialized a copolyester based on HBA as the mesogenic monomer and HNA as the comonomer using random copolymerization. As a result, the three dimensional molecular packing of HBA units is disrupted by HNA units and melting temperature is reduced, but the extended chain conformation is maintained [Tjong, 2003].

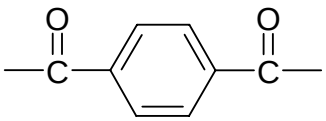

telephthalic acid (TA)

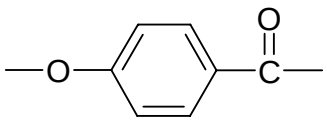

hydroxybenzoic acid (HBA)

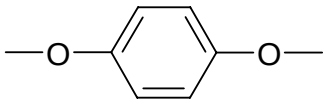

hydroquinone (HQ)

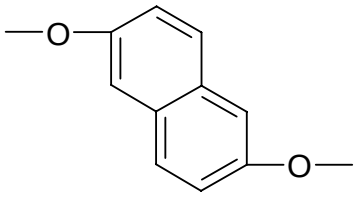

2,6-dihydroxynaphalene (DHN)

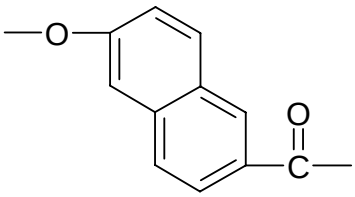

2,6-hydroxynaphthalene acid (HNA)

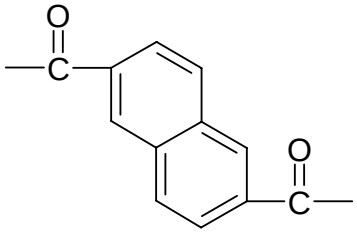

2,6-naphthalene dicarboxylic acid (NDA)

Figure 1.15. Chemical structures of monomers for TLCPs [Tjong, 2003].

1.4.2 Structure and orientation of HBA/HNA copolyester

The structure of HBA/HNA copolyester has been studied using WAXD [Kaito et al., 1990; Wilson et al., 1993; Langelaan and Posthuma de Boer, 1996]. Kaito et al. [Kaito et al., 1990] used HBA/HNA (73 mol%/27 mol%), provided by Polyplastics Co. Ltd. Oriented sheets (thickness of 0.4-0.5 mm) were prepared by extrusion and molding at 290^{o}C. Analysis of WAXD patterns (Figure 1.16) obtained from those samples showed two distinct peaks in the equatorial region. These peaks were associated with (110) and (211) planes at 2θ of 19.8 and 27°.

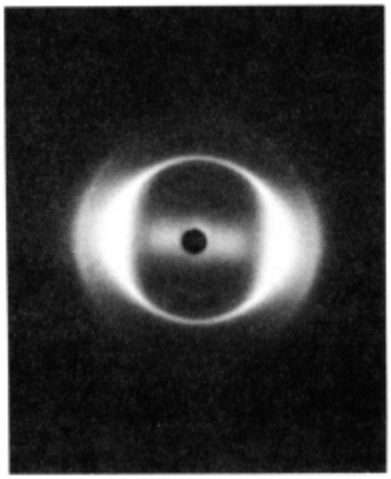

Figure 1.16. WAXD pattern of an extruded sheet sample of HBA/HNA copolyester [Kaito et al., 1990].

Wilson et al. [Wilson et al., 1993] claimed that fibers of HNA rich copolymers (HNA:HBA=3:1 from Hoechst-Celanese Co.) exhibited an orthorhombic phase since the pseudo-hexagonal phase in fibers of HBA rich copolymers (HNA:HBA=1:3 from Hoechst-Celanese Co.) was distorted. Using WAXD data, a pseudo-hexagonal phase in HBA rich polymers was characterized by a single, a very intense equatorial region associated with (110) plane and two other reflections associated with (211) and (310) planes. Furthermore, there was a diffuse region of diffracted intensity centered at the equator which was associated with the non-crystalline phase (Figure 1.17). However, in HNA rich copolymers there is splitting of the (110) peaks into (110) and (200) peaks corresponding to orthorhombic phase (Figure 1.18). It was also noted that not only chemical compositions but also heat treatment can affect the molecular structure of HBA/HNA copolymers [Kaito et al., 1990; Wilson et al., 1993].

Using these WAXD diffractograms, the degree of molecular orientation was quantified [Butzbach et al., 1986; Kaito et al., 1991; Romo-Uribe and Windle, 1996]. The (110) planes were used for calculating an average orientation parameter, which was determined from the second order Legendre polynomial of the orientation distribution. The parameter *f*, also called Herman's orientation parameter, is defined as

$$f = \frac{3\langle \cos^2 \theta \rangle - 1}{2}$$

where θ is the angle between the transition moment vector and the chain axis [Kaito et al., 1991]. If molecules are oriented along longitudinal direction, *f* is 1, and if molecules are oriented along transverse direction, *f* is -0.5.

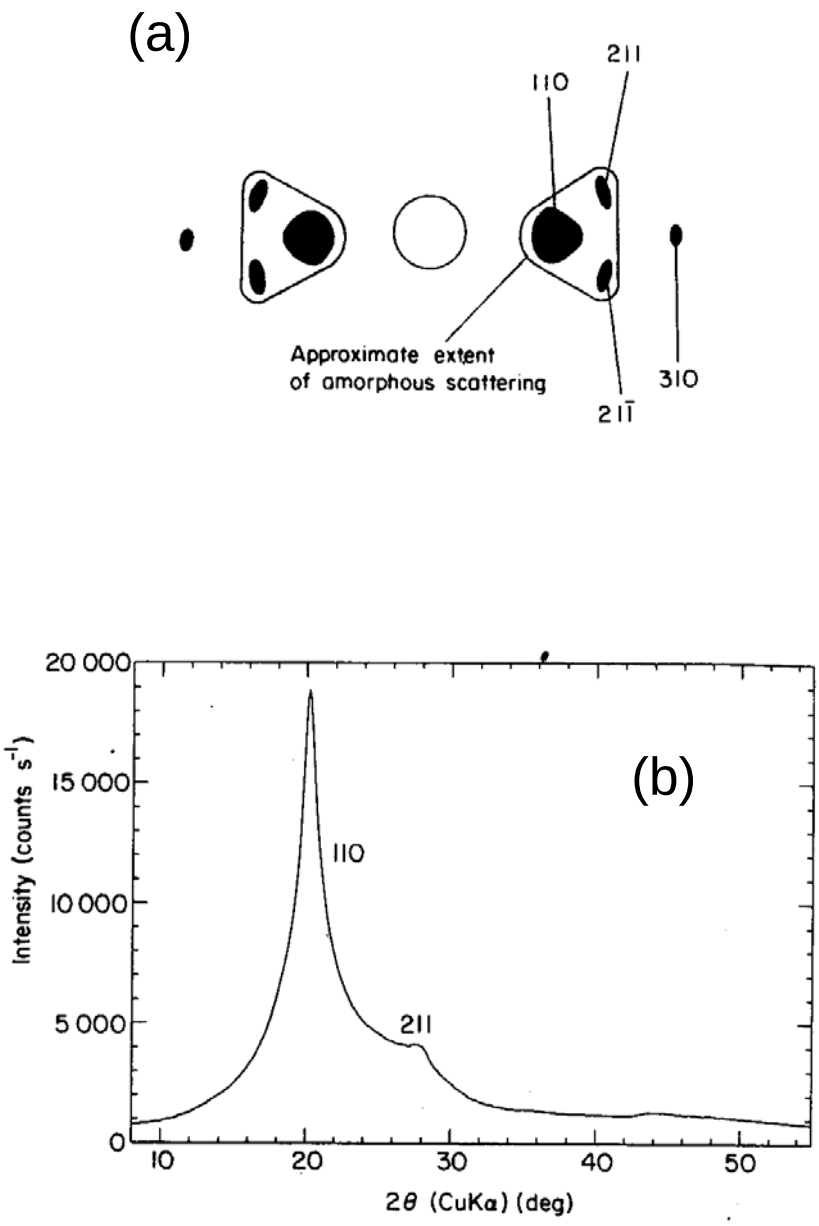

Figure 1.17. (a) Schematic of pseudo-hexagonal phase of WAXD pattern and (b) radial (2θ) intensity profile in fibers of HBA rich copolymers (HNA:HBA=1:3) [Wilson et al., 1993].

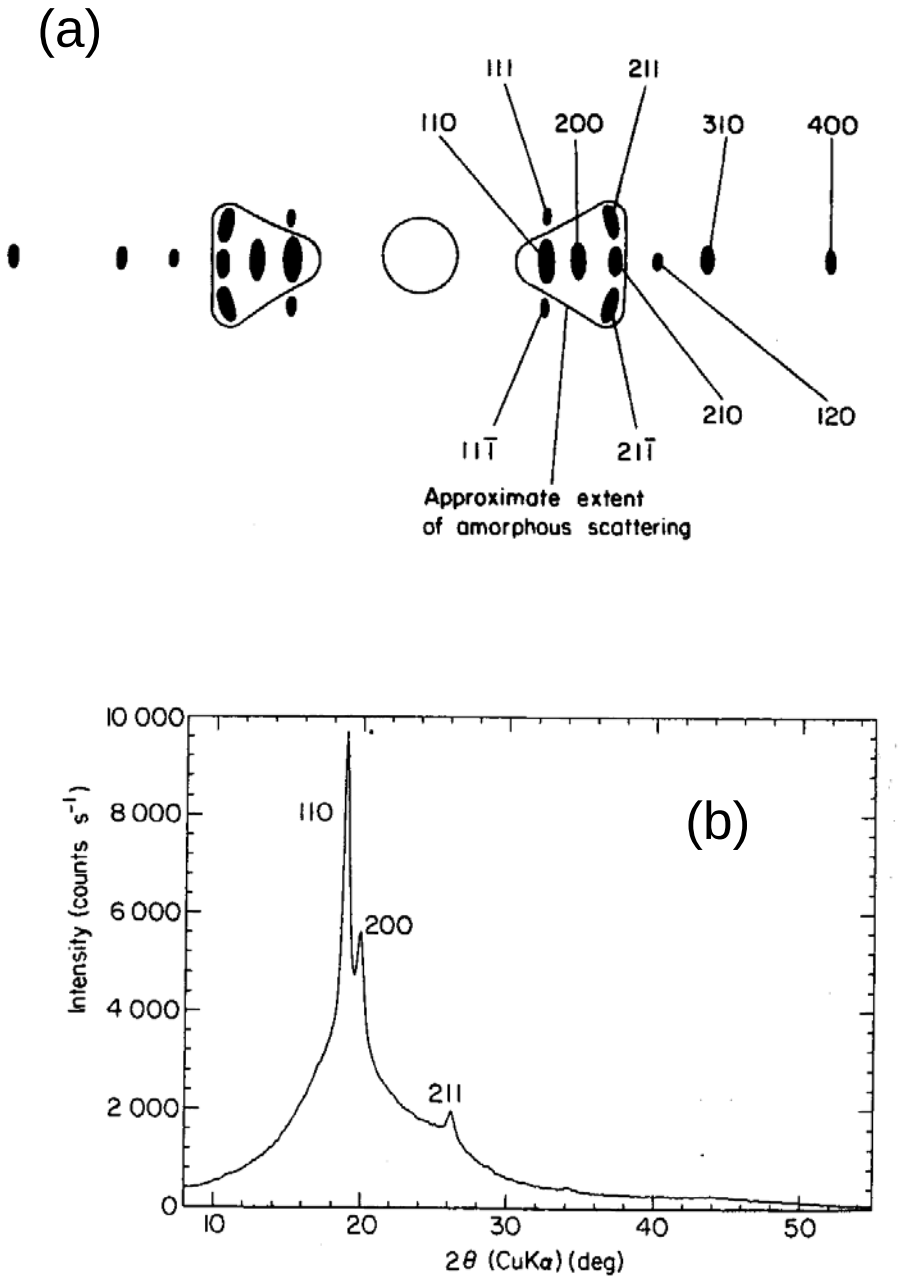

Figure 1.18. (a) Schematic of orthorhombic phase of WAXD pattern and (b) radial (2θ) intensity profile in fibers of HNA rich copolymers (HNA:HBA=3:1) [Wilson et al., 1993].

Further, *f* is zero for a random distribution of molecules. Kaito et al. [Kaito et al., 1991] prepared strand samples of HBA/HNA (73 mol%/27 mol%, Polyplastics Co. Ltd.) using a single screw extruder. Subsequently, these strands were stretched to a draw-down ratio of 10. They reported Herman's orientation parameter values of 0.68-0.88 in strands.

1.4.3. Liquid crystalline polymer composites with carbonaceous materials

As noted earlier, one of the interesting features of liquid crystalline polymers is their excellent mechanical performance. Ticona, a TLCP manufacturer, reported values of 10 GPa and 200 MPa for tensile modulus and strength, respectively, for injection molded Vectra A950 [Ticona, 2007]. It has been found that these high modulus and strength values are due to the intrinsically high degree of molecular alignment in the liquid crystalline phase [Handlos and Baird et al., 1996]. This characteristic helps TLCPs melt processing since their melt viscosities are much lower than those of conventional polymers. In addition, TLCPs possess a low coefficient of thermal expansion, high resistance to chemical degradation, and very low oxygen permeability (Figure 1.19) [Chiou and Paul, 1987]. All these properties make TLCPs promising candidates for electronics packaging applications [Flodberg et al., 2003]. However, like other polymers, TLCPs are not electrically conductive. Therefore, pure TLCPs are inadequate for sensitive electronics packaging applications that need electrostatic dissipative characteristics.

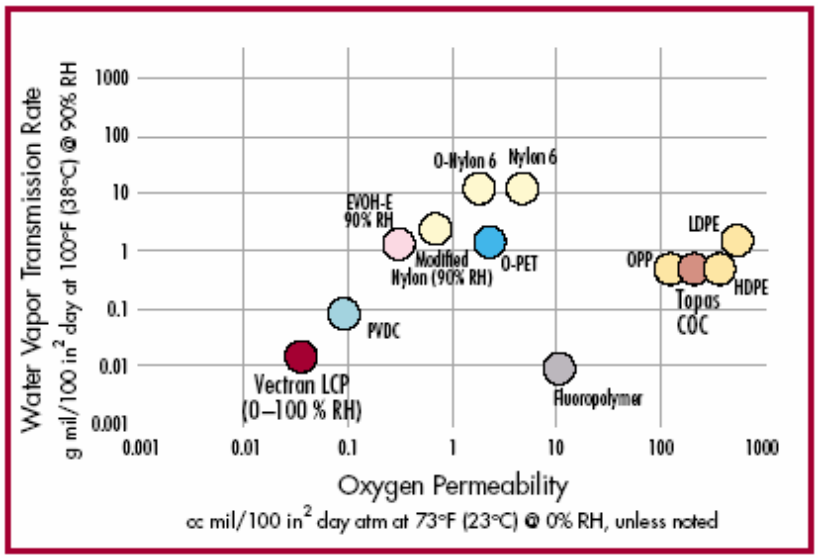

Figure 1.19. The illustration of the exceptionally low permeability to water vapor and oxygen for TLCP (Vectran LCP) [Ticona].

Therefore, carbonaceous materials such as carbon blacks (CBs) [Wong and Shin, 2001; Tchoudakov et al., 2004; King et al., 2006], carbon fibers (CFs) [Jou et al., 2002; Wolf and Willert-Porada, 2005], and CNFs [Yang et al., 2003 and 2005] have been incorporated into TLCPs as conductive fillers. The goal of most of these literature studies was to enhance conductivity and evaluate EMI shielding effectiveness of TLCP composites.

King et al. [King et al., 2006] incorporated CBs (Ketjenblack) into Vectra A950 using a single screw extruder. Ketjenblack possesses a highly branched structure and a large surface area (1250 m^2/g) compared to normal CBs, resulting in decreased electrical resistivity (10^{-2}-10^{-1} Ω-cm) [King et al., 2006]. They found an electrical percolation threshold at 5 wt% of CB and volume resistivity decreased significantly down to 10^7 Ω-cm. Other researchers reported that a similar CB content was required to observe percolation threshold phenomena [Wong and Shin, 2001]. In the open literature, there are only limited studies on CNF/TLCP composites [Yang et al., 2003 and 2005]. Yang et al. reported a volume resistivity of 3×10^2 Ω-cm with TLCP composites containing 5wt% CNFs.

1.5 Objectives

From a literature review of carbon nanofibers and their nanocomposites, it is noted that although there are several studies reported on carbon nanofibers composites, no systematic study has been reported in the literature about the influence of carbon nanofibers on polymer structure. The primary goal of this research was to investigate polymer crystalline and orientation structure in carbon nanofiber based composites. For this study, two different types of carbon nanofibers were incorporated into linear low density polyethylene and thermotropic liquid crystalline polymers. Fundamental properties, such as electrical and mechanical properties, were investigated. Microstructure was investigated using various techniques such as scanning electron

microscopy, transmission electron microscopy and wide angle X-ray diffraction. The specific objectives were to:

1. investigate the micro-structure of carbon nanofibers with different core and surface structures as a function of heat treatments;
2. examine the influence of surface and structural changes of carbon nanofibers on the electrical and mechanical properties, and crystallization behavior of linear low density polyethylene nanocomposites;
3. determine the role of carbon nanofibers in controlling the microstructure of thermotropic liquid crystalline polymers and the resulting properties.

In Chapter 2, the microstructure of two different grades of carbon nanofibers with different core structures, hollow (PR) and solid (MJ), was investigated as a function of two treatments: CVD and thermal. Using Raman spectroscopy and X-ray diffraction analysis, crystallite thickness and width was measured for fibers. Further, the effect of thermal treatment on morphology and textural properties of carbon nanofibers were investigated by BET adsorption isotherms and TEM techniques.

It is hypothesized that the microstructure of nanomodifiers, including surface characteristics, plays a critical role in the properties of nanocomposites that are ultimately produced. By using two different types of carbon nanofibers in linear low density polyethylene, in Chapter 3, mechanical and electrical properties of nanocomposites are reported. Further, the effect of carbon nanofibers on the crystallization characteristics of

linear low density polyethylene was investigated by thermal analysis, wide angle X-ray diffraction, and electron microscopy.

In Chapter 4, copolyester thermotropic liquid crystalline polymers were chosen to investigate how carbon nanofibers affect the orientational structure of polymers. This characteristic can enable us to observe a distinct influence of carbon nanofibers on orientation of thermotropic liquid crystalline polymers. Electrical and mechanical properties of thermotropic liquid crystalline polymer composites in the presence of carbon nanofibers were investigated. The orientational microstructure of nanocomposites was investigated by wide angle X-ray diffraction. Also, scanning electron microscopy and transmission electron microscopy were used to study microstructure and morphology of thermotropic liquid crystalline polymers and their composites.

Finally, Chapter 5 summarizes the conclusions drawn from the present research, and provides ideas for future work. Detailed experimental procedures are described at the end of this dissertation in various appendices.

CHAPTER 2

STRUCTURAL CHARACTERIZATION OF CARBON NANOFIBERS

2.1 Introduction

It is known that structure of carbon nanofibers (CNF) can vary depending on the type of catalyst and carbon precursor used during synthesis [Lee et al., 2001; Qin et al., 2004; Rodriguez et al., 1995]. CNFs contain graphite platelets stacked perpendicular to the fiber axis when iron catalyst is used in conjunction with carbon monoxide/hydrogen (4:1) at 600°C [Rodriguez et al., 1995]. These graphite platelets are parallel to the fiber axis with silica supported iron catalyst even though the same carbon precursor and synthesis conditions were used. Herringbone structure is observed with CNFs synthesized with ethylene/hydrogen (4:1) over iron-copper catalyst at 600°C [Rodriguez et al., 1995].

Carbon precursor also plays an important role of structure of CNFs. It has been reported that helical CNFs were obtained by chemical decomposition of acetylene [Qin et al., 2004; Rodriguez et al., 1995]. In contrast, a fairly straight shape is observed for PR-24-PS and PR-19-PS (Applied Science, Inc., Cedarville OH) that were obtained from iron-sulfide catalyst and natural gas precursor [Applied Science, Inc., 2007].

Two variations of commercial grades (PR-19-PS and PR-24-PS) and one research grade (MJ) were examined in this study. Chapters 3 and 4 will discuss the role of theses nanofibers in the microstructure of the matrices and resulting nanocomposites. The microstructure of reinforcements, including surface characteristics, plays a critical role in the properties of composite materials that are ultimately produced. In this chapter, a

fundamental study of the microstructure of CNFs with different core structure (hollow and solid) was conducted as a function of two treatments: CVD and thermal. The surface and structural changes in CNFs resulting from these treatments are important for ultimately controlling the properties of nanocomposites. This Chapter is based on our results that were recently published [Lee et al., 2007a].

2.2 Experimental

2.2.1 Materials

MJ fibers were prepared from the chemical decomposition of C_2H_4-H_2 mixture (4:1) over Ni-Cu (7:3) bimetallic catalyst [Lee et al., 2001a]. To modify the structure of these CNFs, heat treatment or CVD steps were applied. For heat treatment, an Astro furnace (Thermal Technology Inc.) was used with a He atmosphere. After CNF loading, the temperature was increased to 1000°C at a rate of 20 °C/min. Subsequently, the temperature was increased to 2200°C at a rate of 10 °C/min and the CNFs were held at 2200°C for 1 h. CVD layers were deposited over MJ fibers by pure CH_4 decomposition at 850°C for 5 h in a tubular quartz reactor [Han et al., 2006]. PR-24-PS and PR-19-PS fibers, synthesized using the chemical decomposition of hydrocarbons over iron-sulfide catalyst, were obtained from Applied Science, Inc. (Cedarville OH) [Applied Science, Inc., 2007]. PR-19-PS fibers already have a carbon layer deposited by chemical vapor deposition (CVD) as the outer surface [Applied Science, Inc., 2007]. Hence, six different CNF combinations were studied in this work: MJ, heat treated MJ (MJHT), CVD treated

MJ (MJCVD), PR-24-PS (PR), PR-19-PS (PRCVD) and heat treated PR-24-PS (PRHT) fibers.

2.2.2 Characterization

Raman spectroscopy was performed using a Renishaw Raman system 100 with 26 mW-785 nm diode laser. All the spectra were obtained over a spectral range of 500–3000 cm^{-1}. X-ray diffractometry (XRD, X'pert Pro, Netherlands) using Cu Kα radiation (λ=1.5406 Å) was used over the 2θ range of 5 to 50°. From these techniques, crystallite width (L_a), interlayer spacing (d_{002}), and crysatallite thickness (L_c) were calculated. Typically, three replicates were obtained for quantitative analysis of graphitic structure of CNFs. The overall degree of crystallinity was determined by the oxidation profiles of CNFs using a Pyris 1 Perkin-Elmer thermo gravimetric analysis (TGA) instrument. Samples were heated up to 1000°C at a rate of 10 °C/min under CO_2 gas. STEM-Hitachi H 2000 and TEM-Hitachi H 9500 transmission electron microscope (TEM) were used for investigating structure of CNFs. CNFs were dispersed in a vial with acetone and sonicated for 10 min. This solution was dropped on a formvar/carbon film supported copper grid and dried. The surface area of CNFs was determined by the N_2 adsorption data at 77 K using an automatic surface analyzer (Autosorb-1, Quantachrome). Pore size distribution was obtained by BJH method [Barrett et al., 1951]. These textural measurements and analyses were performed by Dr. Kim's group at Myungji University, Korea.

2.3 Results and Discussion

2.3.1 Crystalline structure of CNFs

Figure 2.1 displays Raman spectra of all six types of CNFs. A weak shoulder at ~1170 cm^{-1} and two sharp peaks at ~1320 cm^{-1} and ~1590 cm^{-1} were observed for both of the base fibers (MJ and PR). For carbon materials, the G band at 1580 cm^{-1} is attributed to the graphitic crystalline structure [Melanitis et al., 1996; Yu et al., 2003; Park et al., 2005]. Structural disorder within graphite planes resulted in the D band at 1360 cm^{-1} [Melanitis et al., 1996; Yu et al., 2003; Park et al., 2005] and the D' band at 1620 cm^{-1} [Melanitis et al., 1996; Jawhari et al., 1995]. A broad peak around 1500-1550 cm^{-1} has been observed with amorphous carbon [Jawhari et al., 1995]. A broad peak around 1150-1200 cm^{-1} is associated with functional groups such as C=O [Keller et al., 2002]. Thus, a shoulder at ~1170 cm^{-1} observed for both fibers can be inferred as functional groups obtained during nanofiber synthesis and storage. At 1400-1500 cm^{-1}, a higher intensity band was observed for PR fibers than for MJ fibers, indicating that PR fibers possess a larger amorphous carbon content than do MJ fibers. Therefore, broader D and G bands were observed for PR fibers. For both nanofibers, a shift of the G band from 1580 cm^{-1} (for highly crystalline structure) to ~1590 cm^{-1} was observed, being inferred as a merger of the G and the D' band. The Raman spectra of CVD-processed fibers did not show a significant difference relative to that of the base fibers.

Heat-treated MJ fibers (MJHT) revealed significant changes in their Raman spectra. They showed a sharper D band, indicating a reduction of functional groups and

amorphous carbon phase. Also, the ~1590 cm^{-1} peak split into 1580 cm^{-1} and 1610 cm^{-1} peaks associated with the G and the D' bands, respectively. Further, a peak at 2610 cm^{-1}, known as the G' band of crystalline graphite, was observed. These results confirm that the heat treatment helps in the graphitization of the amorphous carbon phase. For PRHT fibers, four sharp D, G, D', and G' peaks were observed at 1320, 1580, 1610, and 2620 cm^{-1}, respectively. It is interesting to note that the intensity of the G band is higher than that of the D band, indicating more crystalline graphite content.

In addition, the G' band in PRHT fibers was more intense than that in MJHT fibers. Therefore, PR fibers were more graphitized than MJ fibers at the given heat treatment condition. After deconvolution of Raman spectra for nanofibers, the integrated intensity ratios of the D to G bands (I_D/I_G) were measured. Using the I_D/I_G ratio, crystallite width (L_a) was determined ($L_a=44[I_D/I_G]^{-1}$(nm)) [Yu et al., 2003; Park et al., 2005] and is reported in Table 2.1. It is evident that crystallite width increased with the heat treatment for both MJ and PR fibers. Further, the heat treatment led to more significant change of L_a of PR fibers (1.7±0.7→8.0 ±0.7nm) than that of MJ fibers (1.0±0.2→3.1±0.5nm).

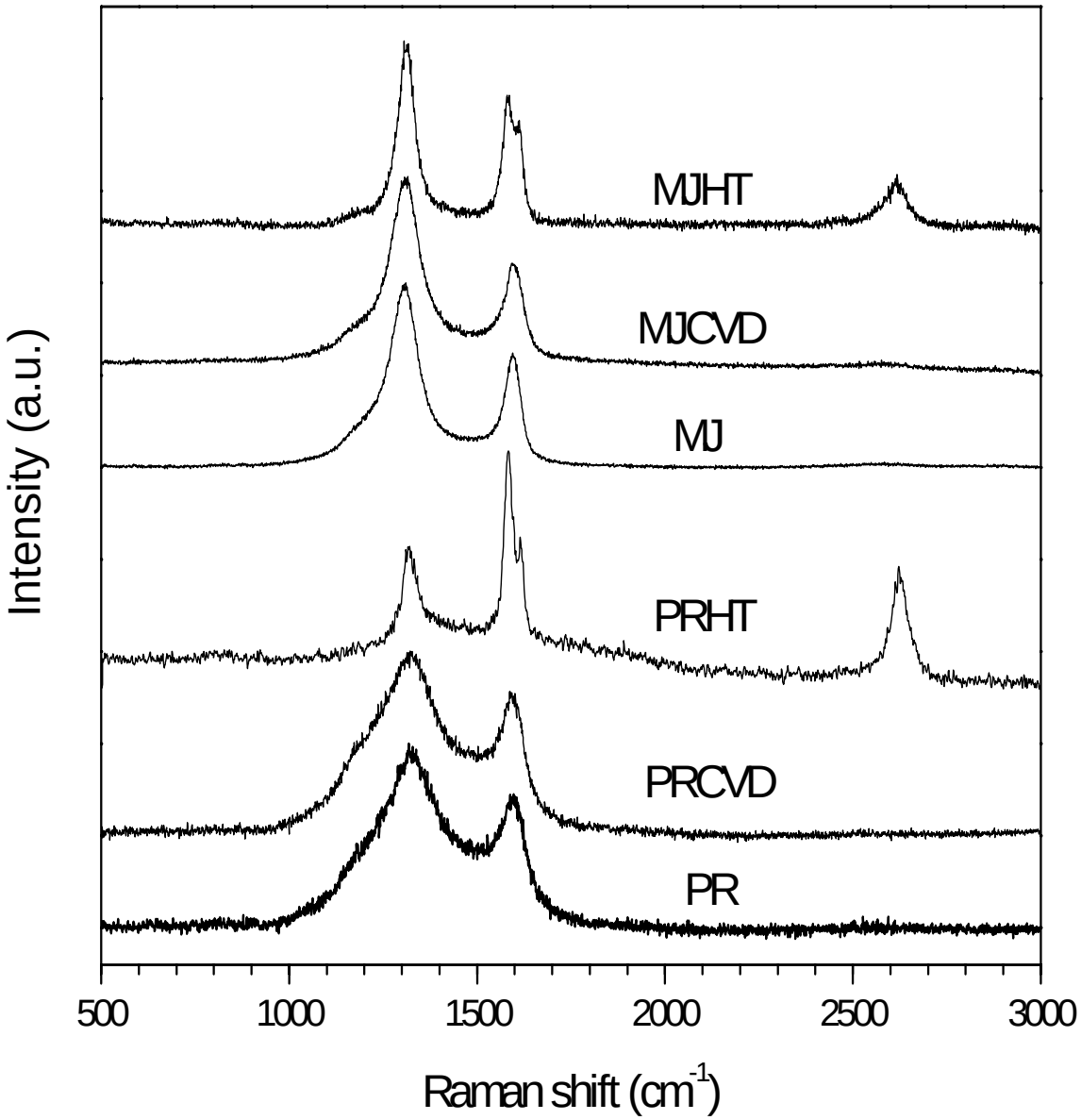

Figure 2.1. Raman spectra of carbon nanofibers.

Table 2.1. Crystalline properties of carbon nanofibers

CNFs	d_{002}[1] (nm)	L_c[1] (nm)	I_D/I_G[2]	L_a[2] (nm)
MJ	0.3409	1.6±0.1	4.4±1.0	1.0±0.2
MJCVD	0.3409	1.7±0.1	4.7±0.2	0.9±0.1
MJHT	0.3384	10.9±0.5	1.4±0.2	3.1±0.5
PR	0.3400	3.1±0.3	3.1±1.3	1.7±0.7
PRCVD	0.3405	2.9±0.1	2.5±0.7	1.9±0.6
PRHT	0.3386	11.7±0.4	0.6±0.1	8.0±0.7

Obtained from [1]XRD and [2]Raman data

The integrated azimuthal profiles (2θ scans) from XRD of CNFs are displayed in Figure 2.2; the baselines are shifted vertically for convenience. At $2\theta \approx 26°$, a distinct peak associated with the (002) graphene planes appeared for all samples. It is evident that peaks of heat treated CNFs sharpened and shifted to higher angles. Also, for PR fibers, a weak peak and a shoulder were observed at $2\theta \approx 43$ and 44°, indicating (100) and (101) graphene planes, respectively [Park et al., 2005; Hwang et al., 2002]. It is evident that the intensity of these peaks was higher for PRHT. In contrast, MJ fibers showed two weak, broad peaks at $2\theta \approx 43$ and 44°.

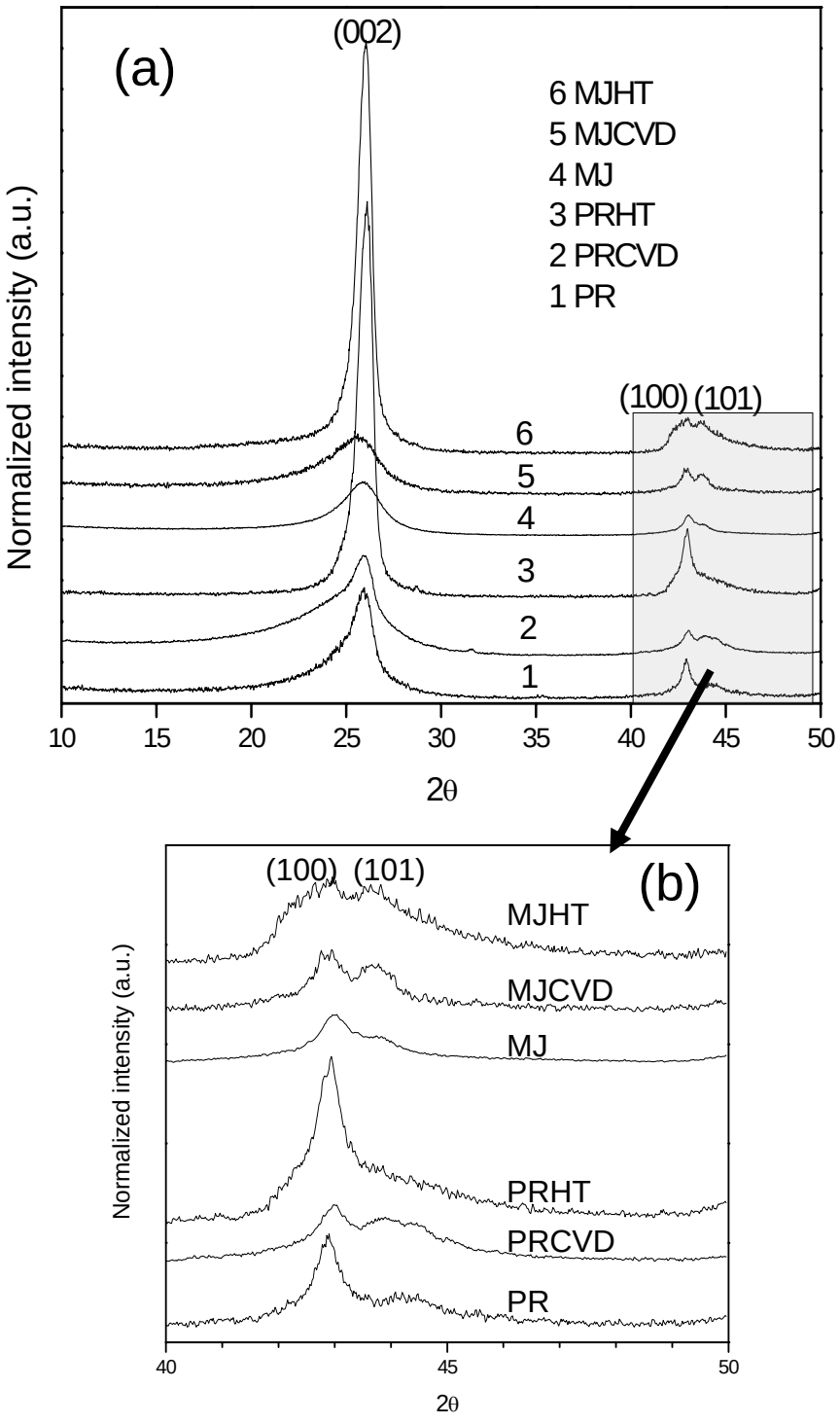

Figure 2.2. X-ray diffractograms of carbon nanofibers.

Despite an increase of intensity of these peaks for MJHT over MJ fibers, they were less significant compared to those for PRHT over PR fibers. Based on these profiles, the interlayer spacing (d_{002}) was calculated using Bragg's law. Using Scherrer formula, crystallite thickness (L_c) was calculated for all CNFs (Table 2.1). As expected, the integrated azimuthal profiles and d_{002} data confirm that the heat treatment for both MJ and PR fibers led to a significant increase of graphitic content and crystallite thickness.

Further, using TGA analysis, the weight loss of various CNFs in a CO_2 environment was measured at a heating rate of 10°C/min (Figure 2.3). The onset temperatures were ~600°C and ~500°C for MJ and PR fibers, respectively. The oxidation was complete at ~800°C and ~890°C for MJ and PR fibers, respectively. This broader oxidation range of PR fibers indicates that, as compared to MJ fibers, PR fibers contain a wider range of ordered carbon structure.

The onset and complete oxidation temperature of MJCVD fibers were ~ 630°C and ~880°C, higher than that of MJ fibers. It is likely that the CVD layers obtained at 850°C contribute additional crystallinity over that of bare MJ fibers (prepared at 600°C). Another possible explanation is that the more active sites for CO_2 oxidation are blocked by the CVD layers. In contrast, PRCVD fibers showed a similar oxidation profile as PR fibers (~500°C and ~910°C for onset and complete oxidation temperature, respectively). The onset temperatures were ~730°C and ~780°C for MJHT and PRHT fibers, respectively. The oxidation was complete at ~1000°C and ~1100°C for MJHT and PRHT fibers, respectively.

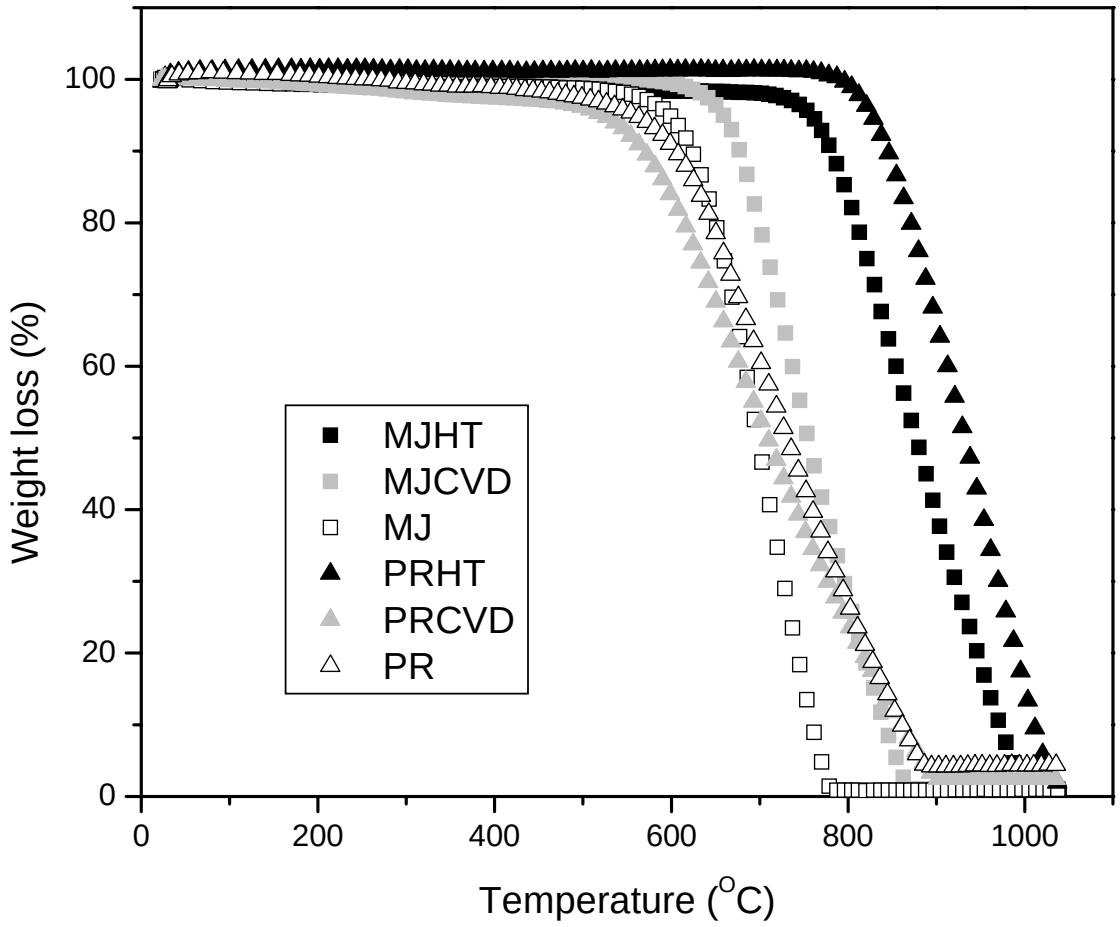

Figure 2.3. TGA profiles of various carbon nanofibers.

It is evident that heat-treated CNFs showed higher onset temperatures than did untreated CNFs. More interestingly, PRHT fibers showed higher onset and completion temperatures than did MJHT fibers, indicating that the structure of PRHT fibers is more ordered than that of MJHT fibers. Thus, heat treatment at 2200°C is more effective in changing the structure of PR fibers than that of MJ fibers.

2.3.2 Morphology of CNFs

MJ and PR nanofibers were investigated using scanning electron microscopy (SEM). It is interesting that MJ nanofibers are twisted or even coiled whereas PR nanofibers are fairly straight (Figure 2.4). Surface morphology of CNFs was observed by STEM (Figure 2.5a-f). STEM micrographs of the CNFs reveal that MJ nanofibers possessed rough surfaces even after CVD or heat treatment. It is noted that the surface of PR nanofibers was significantly smoother than that of MJ nanofibers.

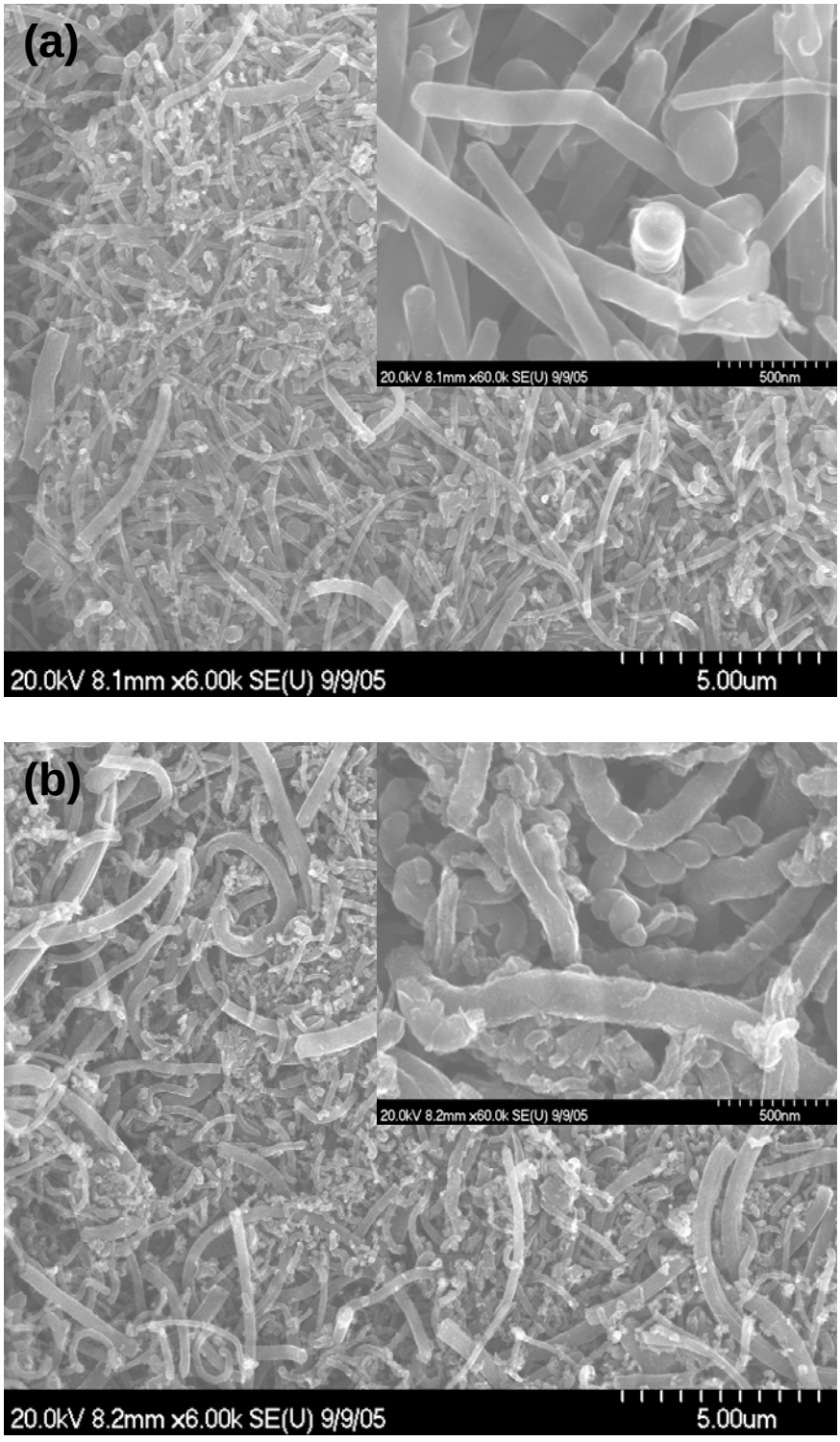

Figure 2.4. Scanning electron micrographs of: (a) PR and (b) MJ fibers.

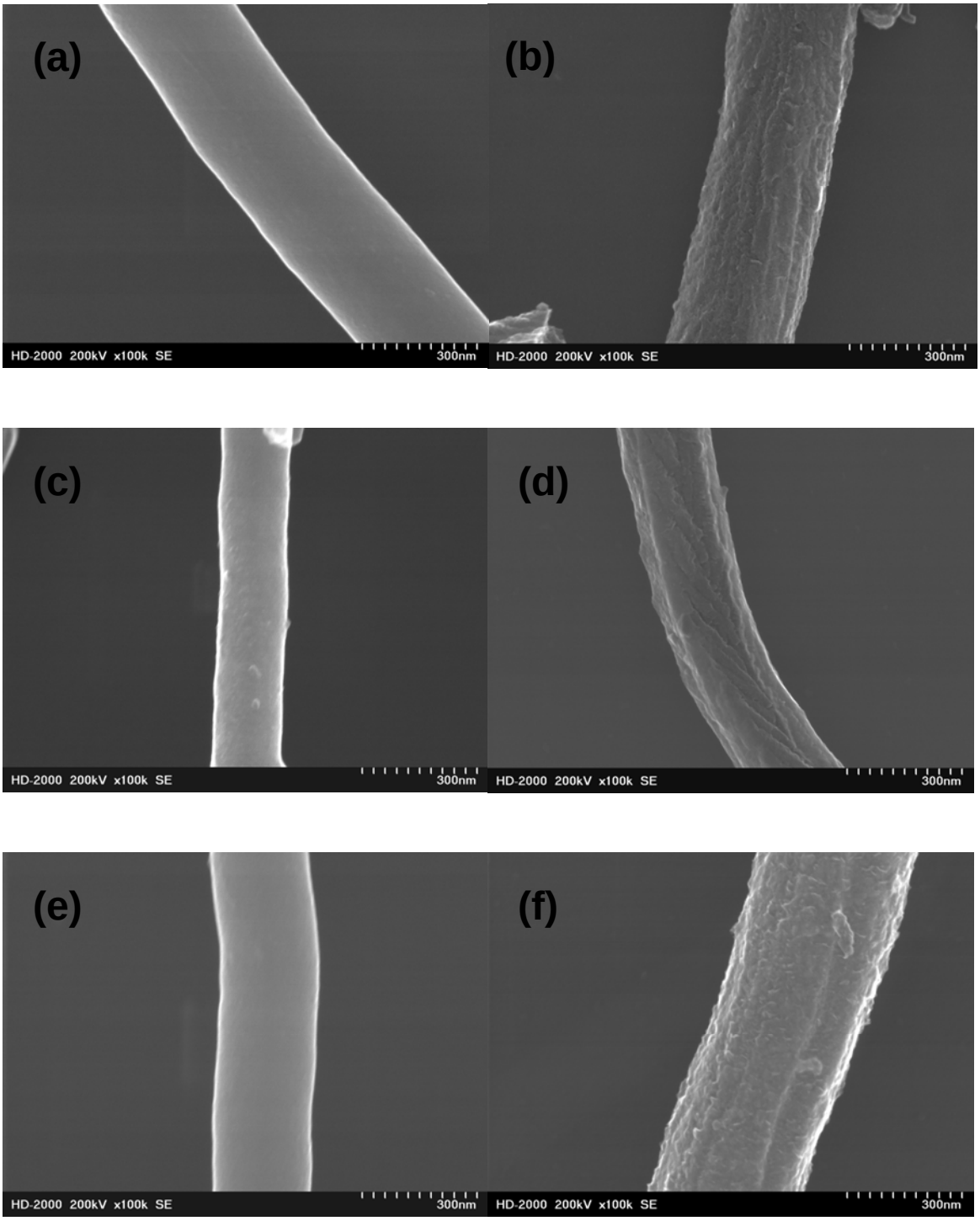

Figure 2.5. Scanning transmission electron micrographs of (a)PR, (b)MJ, (c)PRCVD, (d)MJCVD, (e)PRHT, and (f)MJHT fibers.

Uchida et al. [Uchida et al., 2006] reported single and double layer morphologies for PR-24-HT fibers (heat treated at 3000°C). Single layer PR-24-HT fibers possessed graphite sheets oriented at about 15° to the fiber axis. In contrast, TEM of a distinct double layer PR-24-HT fiber has been reported to show that two layers have different angles with respect to the fiber axis [Uchida et al., 2006]. Graphite sheets of inner layer were varied between 4 to 36°, whereas outer layers were oriented along fiber axis [Uchida et al., 2006]. Single layer PR-24-HT displayed the loops in outer and inner surface of a wall, which has been also reported in prior literature studies. [Hwang et al., 2002; Uchida et al., 2006; Endo et al., 2003].

Similar morphologies were observed in PRHT fiber at a much lower heat treatment temperature of 2200°C, as compared with that of Uchida et al. [Uchida et al., 2006] (Figure 2.6). Loops were observed at both walls for single layer PRHT. A more interesting observation was that there was a significant discontinuity between inner and outer layer due to folding of graphene layer (Figures 2.6e and f). This spatial discontinuity was not visible in PR fibers (Figures 2.6a and b). There was not a significant difference between PR and PRCVD fibers.

Figures 2.7a and b display TEM micrographs of MJ fibers. These nanofibers possess a solid core, in contrast to the hollow core for PR fibers. Similar to PR fibers, a significant change was not observed after CVD treatment. Inter layers of MJHT (Figure 7e) were more aligned than those of MJ (Figure 7a). Further, on the edge of MJHT, loops were observed due to heat treatment, indicating enhancement of graphitic structure (Figure 7f).

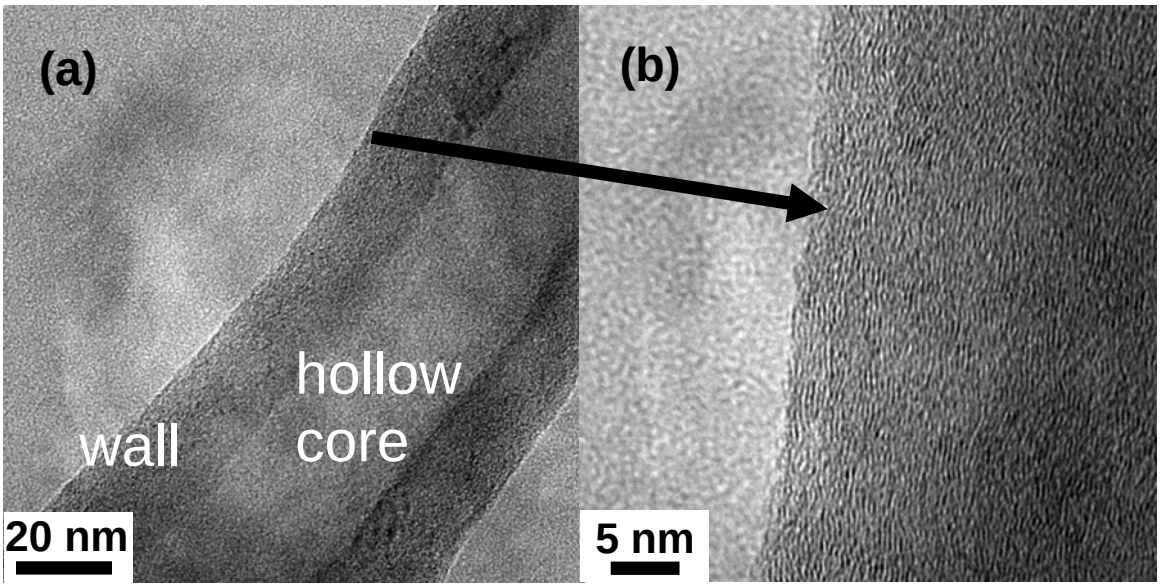
(a)
(b)
hollow
core
wall
20 nm
5 nm

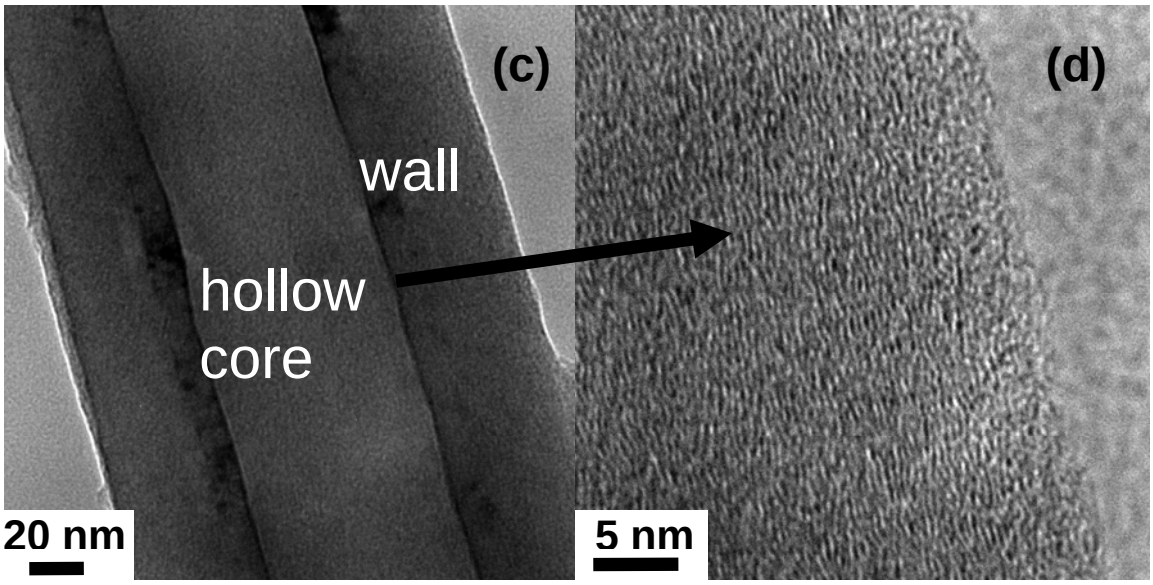
(c)
(d)
wall
hollow
core
20 nm
5 nm

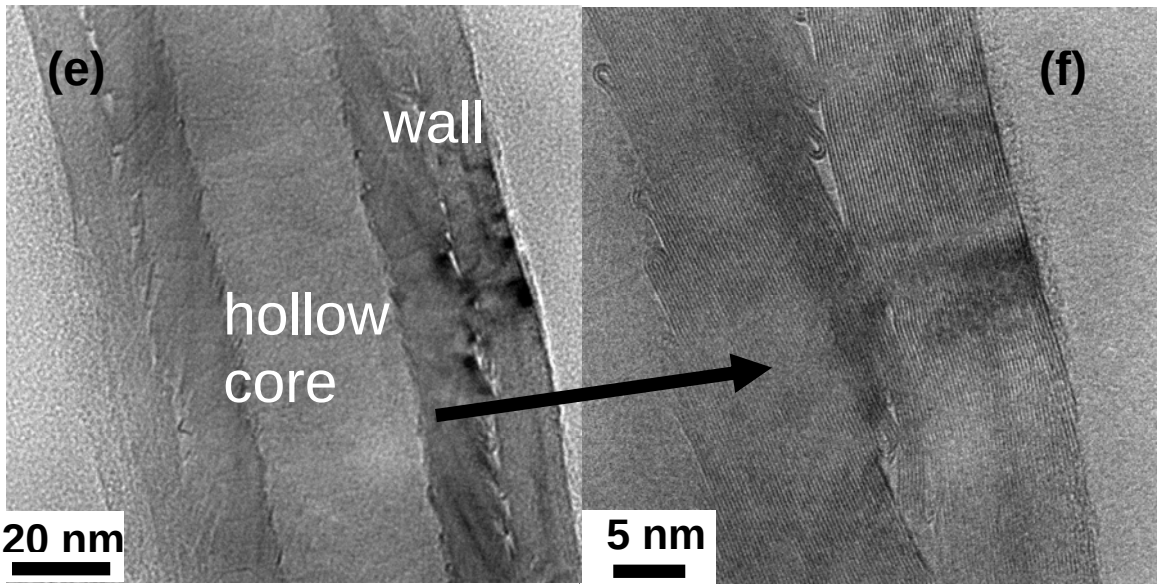

Figure 2.6. Transmission electron micrographs of double layer structure of (a)PR, (b)PR, (c)PRCVD, (d)PRCVD, (e)PRHT, and (f)PRHT fibers. (b), (d), and (f) are in high resolution for (a), (c), and (e), respectively.

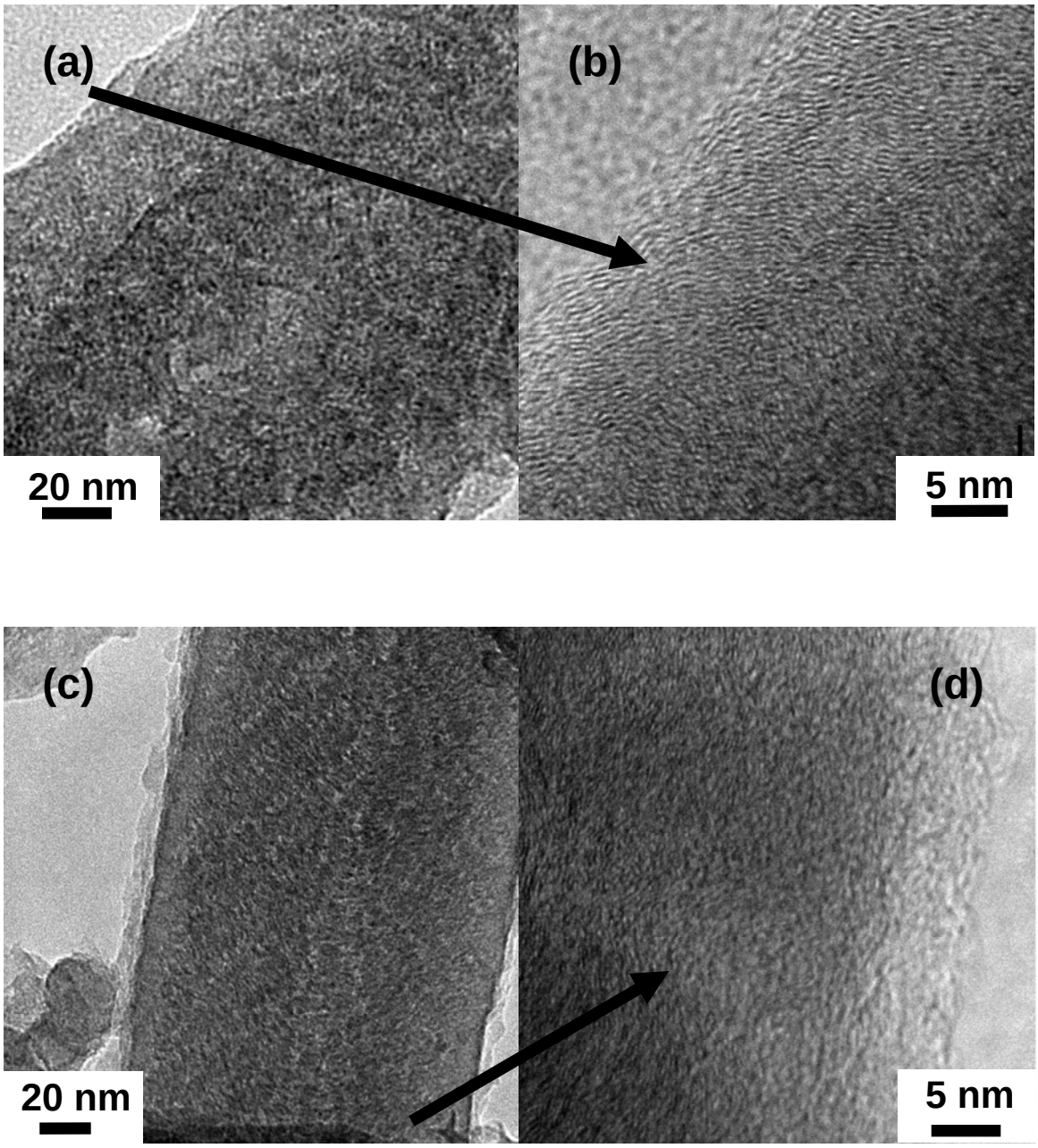
(a)
(b)
20 nm
5 nm
(c)
(d)
20 nm
5 nm

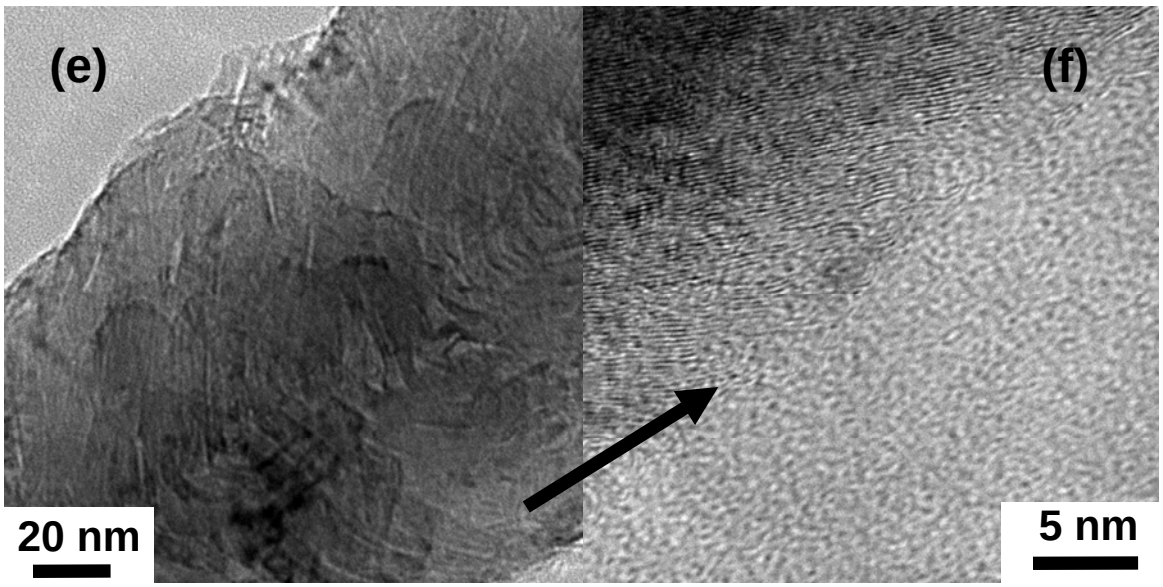

Figure 2.7. Transmission electron micrographs of (a)MJ, (b)MJ, (c)MJCVD, (d)MJCVD, (e)MJHT, and (f)MJHT fibers. (b), (d), and (f) are in high resolution for (a), (c), and (e), respectively.

There was a spatial discontinuity between graphene layers for MJHT (Figures 7e and f), but not for MJ. It is likely that an irregular reorganization and a decrease of the interlayer spacing resulted in a distinct spatial discontinuity. It is evident that crystallinity of MJHT (Figure 7e and f) is less than that of PRHT (Figure 6e and f). This is consistent with the more significant change of structure of PR fibers than that of MJ fibers during heat treatment.

The selected area electron diffraction (SAED) technique uses selected area aperture during TEM to analyze the microstructure. The advantage of this technique is that a much smaller area is needed than that for X-ray diffraction. Therefore, SAED can focus on an individual specimen, whereas X-ray diffraction provides structural information of the bulk specimen. SAED has been used to investigate the graphitic structure of carbon nanotubes [Belin and Epron, 2005; Le Brizoual et al., 2007] and carbon nanofibers [van Gulijk et al., 2006; Ono and Oya, 2006; Zheng et al., 2006; Lueking et al., 2007; Lin et al., 2007].

SAED patterns and corresponding bright field images of PR and PRHT fibers are shown in Figures 2.8a and 2.8b, respectively. PR fibers showed one set of arcs and two diffuse haloes, associated with (002), (100), and (110) planes. The inset bright field image indicated the orientation of PR fiber, and confirmed that the (002) arcs are parallel to the graphene layer of CNFs.

In contrast, in the SAED pattern of PRHT fiber, two sets of arcs associated with (002) and (004) planes were observed, indicating a higher order of crystalline structure of PRHT fiber. It is noted that (002) and (004) arcs also have superposed spots.

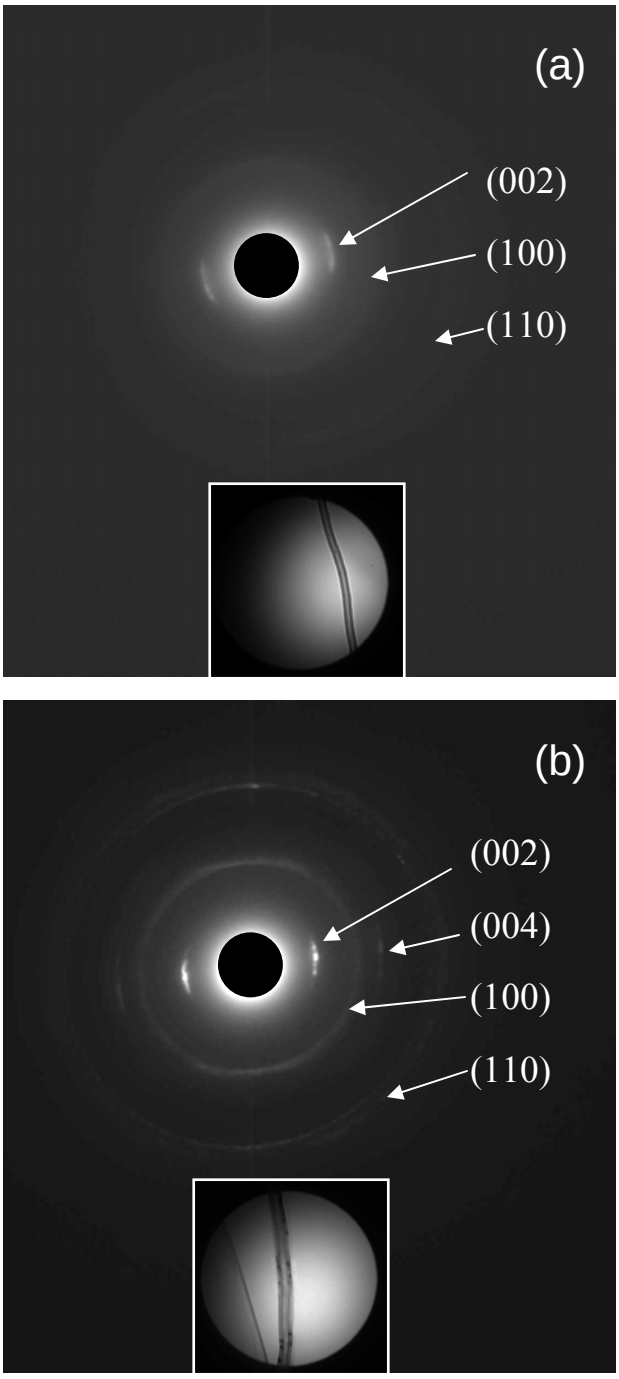

Figure 2.8. SAED patterns of (a) PR and (b) PRHT fibers. The insets show the corresponding bright field images.

Lin et al., claimed that more than one set of (002) diffraction spots are related to the arrangement of graphitic laminations in the microstructure [Lin et al., 2007]. Further, two diffraction rings, associated with (100) and (110) planes, were also observed. It was reported that these two diffraction rings are related with the random chiralities of graphene cones that are perpendicular to the electron beam [Lueking et al., 2007]. These are consistent with the fact heat treatment of PR led to enhancement of graphitic structure from X-ray, Raman, and TEM as described above.

To measure textural properties, N_2 adsorption-desorption isotherms at 77K were obtained. According to the IUPAC classification, all CNFs exhibit Type II characteristic (Figure 2.9) [Donohue and Aranovich,1998]. Using such isotherms, surface area was calculated (Table 2.2). MJ fibers possessed larger surface area (300 m^2/g) than did other CNFs. It is evident from pore size distribution and pore volume of various CNFs that MJ fibers have a large total pore volume (0.525 cm^3/g). However, significant reduction of surface area and pore volume was observed after CVD and heat treatment; the values were 51 m^2/g and 0.146 cm^3/g for MJCVD, and 30 m^2/g and 0.098 cm^3/g for MJHT, respectively. PR fibers had a significantly smaller surface area and pore volume (35 m^2/g and 0.069 cm^3/g) as compared with MJ fibers. However, there was no significant reduction of these values after CVD and heat treatment. In MJ fibers, the reduction of surface area and pore volume suggests that CVD and heat treatment lead to pore-filling and pore-collapsing, respectively.

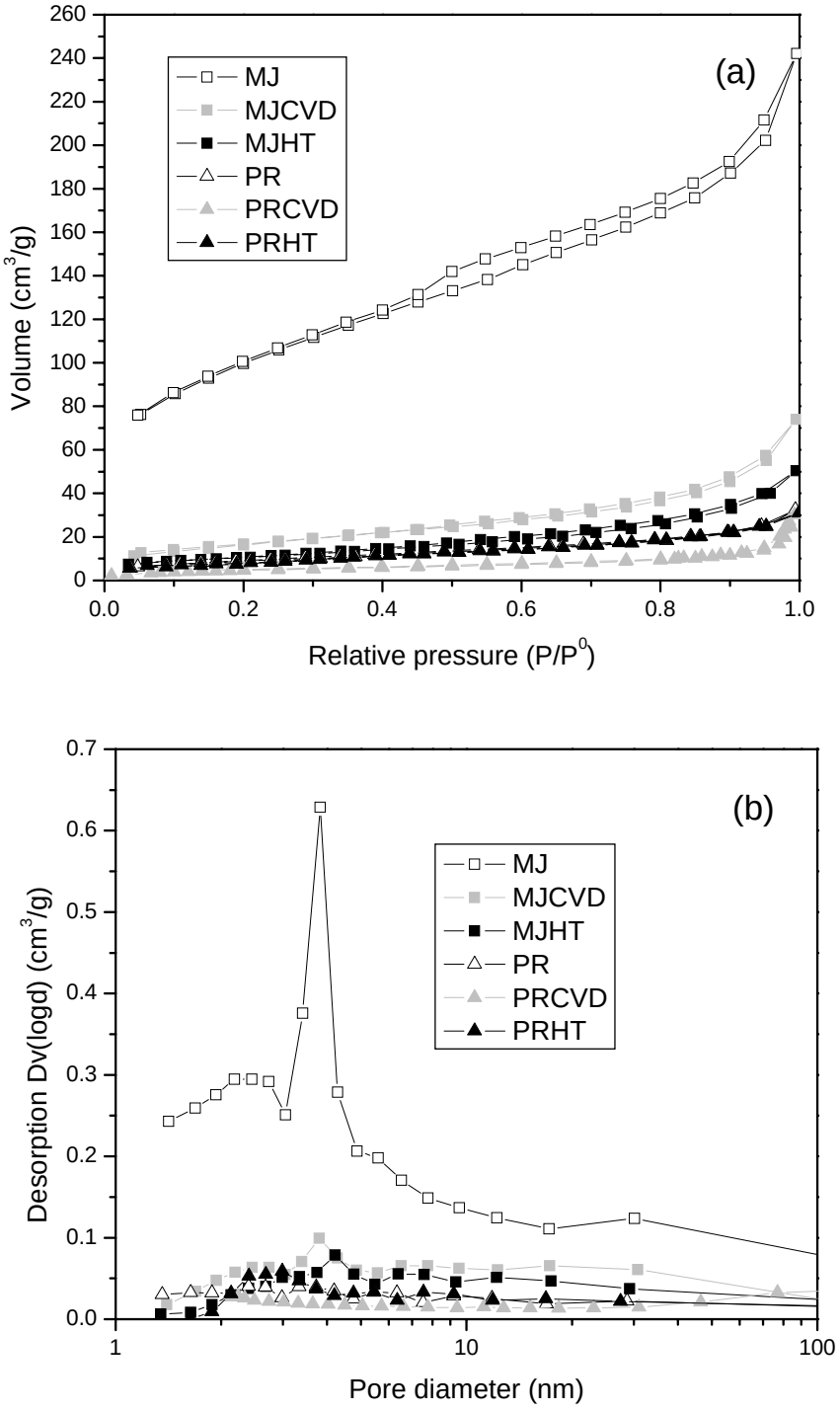

Figure 2.9. (a) N_2 adsorption-desorption isotherms and (b) pore size distributions of carbon nanofibers.

Table 2.2. Textural properties of carbon nanofibers

CNFs	BET surface area (m^2/g)	Total pore volume (cm^3/g)	Micropore volume (cm^3/g)	Mesopore volume (cm^3/g)
MJ	300	0.525	0.174	0.351
MJCVD	51	0.146	0.030	0.116
MJHT	30	0.098	0.019	0.079
PR	35	0.069	0.016	0.053
PRCVD	19	0.037	0.010	0.027
PRHT	29	0.062	0.014	0.048

PR and MJ fibers showed no significant difference of L_a (1.7±0.7 nm and 1.0±0.2 nm for PR and MJ, respectively) and L_c (3.1±0.3 nm and 2.9±0.1 nm for PR and MJ, respectively), indicating a similar degree of crystallinity (Table 2.1). However, after heat treatment, it was observed that PRHT fibers possess a higher crystalline order relative to MJHT fibers. It is likely that pore-collapsing by diffusion of carbon species may limit the graphitization of MJ fibers. Even after pore-collapsing due to heat treatment, all pores can not be filled, implying that pores trapped inside act as discontinuities. Hence, it is apparent that discontinuity is bigger as graphene layers are dense after reorganization.

In contrast, PR fibers inherently possess fewer pores that lead to a higher crystallinity without discontinuity. However, a distinct spatial discontinuity between inner and outer layer on double layer structure of PRHT fiber due to folding, which was

not evident in PR fibers, suggesting that discontinuity disrupts a perfect growth of crystalline structure of CNFs with heat treatment.

These surface and structural differences between PR and MJ fibers are relevant in composite applications. The enhanced graphitic structure of PR fibers (after heat treatment) indicates that PRHT fibers may be better-suited for EMI shielding application where highly conductive materials (>1×10^{-2} S/cm) are needed [Yang et al., 2005]. In this preliminary study, linear low density polyethylene nanocomposites with 10 wt% PRHT (~1.5×10^{-2} S/cm) showed two orders of magnitude higher conductivity than those with 10 wt% PR (~1.5×10^{-4} S/cm). In contrast, MJ fibers possess rough surfaces and porous structures (without subjecting them to surface activation treatment), which hinders development of graphitic structure during heat treatment. Therefore, composites based on these fibers can be used for electrodes of electrochemical application such as super capacitors or fuel cells where a large surface area and pore volume of conducting materials are crucial [Kim et al., 2004; Chai et al., 2005].

2.4. Conclusions

The microstructure of two different grades of CNFs, MJ (experimental) and PR (commercial), was investigated as a function of different thermal treatments. From Raman spectroscopy and XRD analysis, an enhancement of crystallite size was observed after heat treatment at 2200°C. The crystallite thickness increased from 1.6±0.1 nm to 10.9±0.5 nm for MJ fibers and from 3.1±0.3 nm to 11.7±0.4 nm for PR fibers; width increased from 1.0±0.2 nm to 3.1±0.5 nm for MJ fibers and from 1.7±0.7 nm to 8.0±0.7

nm for PR fibers, confirming an increase of crystalline size. Also, an increase in thermal oxidation stability for heat-treated CNFs was observed. BET adsorption isotherms showed a significant reduction of specific surface area for MJ fibers (300 m^2/g) after the heat treatment (51 m^2/g) and also after the CVD surface treatment (30 m^2/g), resulting from a decrease of pore volume (from 0.525 cm^3/g for MJ to 0.146 cm^3/g and 0.098 cm^3/g for MJCVD and MJHT, respectively). However, even after heat treatment, MJ fibers possessed a rougher surface than did PR fibers. In addition, TEM micrographs revealed a significant spatial discontinuity after heat treatment, resulting from reorganization of graphene layers due to pore-collapsing and folding of graphene layers for PRHT and MJHT fibers, respectively. These surface and structural changes in CNFs are important for ultimately controlling the electrical and electrochemical properties of nanocomposites because graphitic content and structure play an important role in the nanocomposite. In Chapters 3, PRCVD, PR, and MJ fibers were incorporated into linear low density polyethylene using intensive mixing. Also, PR and MJ fibers were used for preparing nanocomposites with thermotropic liquid crystalline polymers.

CHAPTER 3

INFLUENCE OF CARBON NANOFIBERS ON THE PROPERTIES AND CRYSTALLIZATION BEHAVIOR OF LINEAR LOW DENSITY POLYETHYLENE NANOCOMPOSITES

3.1 Introduction

Due to the significantly small length scale of nanofibers relative to carbon fibers, crystallization of polymer matrices in the presence of such nanoreinforcements has received significant attention in recent studies [Lozano and Barrera, 2001; Bhattacharyya et al., 2003; Manchado et al., 2005; Probst et al., 2004; Li et al., 2004]. Lozano et al. observed that 5 wt% CNF content led to a higher nucleation rate of polypropylene (PP), which was reflected as an increase in crystallization temperature by 8°C [Lozano and Barrera, 2001]. It was also observed that the addition of carbon nanotubes in various polymers such as polyethylene (PE) [McNally et al., 2005], polypropylene [Bhattacharyya et al., 2003; Manchado et al., 2005], polyvinyl alcohol [Probst et al., 2004], and ethylene-vinyl acetate copolymer [Li et al., 2004] increased the crystallization temperature without significantly affecting the degree of crystallinity or melting point (T_m). For example, T_m of medium density PE remained almost unchanged after the addition of 10 wt% MWNT (~127°C) [McNally et al., 2005].

Linear low density polyethylene (LLDPE) is widely used for packaging applications because of its film-forming properties, good barrier characteristics, and

desirable mechanical properties [Cherukupalli and Ogale, 2004]. These properties of LLDPE can be modified by the incorporation of various α–olefin co-monomers such as 1-butene, 1-hexene and 1-octene [Prasad, 1998]. However, incorporation of such co-monomers does not change the electrical properties to any appreciable extent. Therefore, in this study, two commercial grades of CNFs (PR and PRCVD) and one research grade (MJ) were incorporated into LLDPE to improve electrical conductivity. Electrical and mechanical properties of these nanocomposites were measured. However, the focus of this study is the effect of carbon nanofibers on the crystallization characteristics of LLDPE, as measured by thermal analysis, wide angle X-ray diffraction (WAXD), and electron microscopy. This Chapter is based on our work that was recently published [Lee et al., 2007b].

3.2. Experimental

3.2.1. Materials

Poly(ethylene-*co*-1-octene) (DOWLEX 2045 LLDPE, Dow Chemical) was used throughout this study as it is suitable for film applications. The properties of the resin as given by the manufacturer are: density of 0.920 g/cm^3, melt flow index (MFI) of 1.0 g/10 min, DSC melting point of 122°C, and vicat softening point of 108°C.

A Rheomix 600 mixer was used for intensive mixing of LLDPE and various contents of CNF (PRCVD, PR, and MJ fibers). 30 g of physically blended LLDPE and CNFs were fed into the device and mixed for durations ranging from 2 min to 20 min at

190°C. Shorter mixing times (2-6 min) resulted in lower percolation threshold and higher electrical conductivity, but also resulted in poorer spatial homogeneity of the nanocomposites. Consequently, the longer mixing time of 20 min was used for all subsequent studies. Next, the compounded forms of pure LLDPE (control) and nanocomposites were pressed in a Carver laboratory press at 190°C at a nominal pressure of 2.8 MPa applied for 5 min. Subsequently, the pressure was increased to 5.5 MPa for 3 min, and pressed samples were air-cooled to ambient conditions in approximately10 min.

3.2.2. Nanocomposite characterization

The static decay time was measured at 25°C using a static decay meter (Model 406D, Electro-Tech Systems, Inc.) to characterize the ability of molded samples to dissipate an induced surface charge. The test method was based on the Federal Test Method 101C, Method 4046, and Military Specification Mil-B-81705B that require 99 % of the induced charge to be dissipated in less than 2 s. The electrical resistivity was measured by a digital ohmmeter (Megohmmeter ACL 800) at ~25°C. The electrical measurements were conducted at two different voltages (10 and 100 V) to account for low and high resistances and corrected for specimen geometry (Appendix A3). Measurements were conducted at ten different locations on three replicates.

For mechanical testing, the compressed sheets were cut into dumbbell shaped specimens to dimensions of 7.5mm × 24.5 mm, with a thickness of 0.4 to 0.6 mm. The tensile properties were measured according to ASTM D 638 using an ATS universal

tensile tester 900 at ~25°C. The crosshead speed was 50 mm/min for all specimens, and five replicates were tested at each condition.

A Hitachi FE S-4300 scanning electron microscope (SEM) was used for examing cross-section of fractured nanocomposites. Specimens were cryo-fractured in liquid nitrogen. The specimens were coated with platinum for 1 min using a sputter coater, and then the cross-section was examined.

Pure LLDPE and its nanocomposites were also investigated by WAXD (Rigaku and XRD 2000 Scintag units) equipped with Cu Kα X-ray source. Diffracted patterns were captured on 2-D image plates, which were scanned using a Fuji BAS 1800 scanner. An exposure time of 30 min per image was utilized throughout the study. The Fraser-corrected WAXD diffractograms were analyzed using Polar® 2.6.8 software.

Thermal analysis was performed in a Perkin-Elmer differential scanning calorimeter (DSC). An indium standard was used for temperature calibration. Samples were heated to 190°C at a rate of 10°C/min and held at that temperature for 10 min to erase thermal history of samples. Subsequently, samples were cooled to 50°C at a rate of 0.5-10°C/min and then heated to 190°C again at a rate of 10°C/min for studying the effect of nanofibers on the non-isothermal crystallization. For isothermal crystallization, samples were rapidly cooled (40°C/min) from 190°C and held at 112-116°C for 60 min.

A Hitachi H 7600 and H 9500 transmission electron microscope (TEM) were used for investigating crystalline structure of LLDPE in pure and composite forms containing 15 wt% CNFs. To control thermal history of samples, they were held for 10 min at 190°C and cooled at a rate of 10°C/minin in a Perkin-Elmer DSC. Samples were chemically

treated with chlorosulphonic acid for 10 hrs at 25°C [Sawyer and Grubb, 1996; Defoor et al., 1992]. After cryo-microtoming at -50°C, samples were dispensed on a formvar/carbon film-supported copper grid. Subsequently, they were stained with 2% uranyl acetate for 2 hrs at 25°C [Sawyer and Grubb, 1996; Defoor et al., 1992].

The nominal thickness of polymer lamellae was measured in pure LLDPE and 15 wt% CNF nanocomposites. Seven replicate images were obtained for each composition, and the thickness of multiple lamellae (n=70) was computed by the use of image analysis software provided with the microscope.

3.3. Results and Discussion

3.3.1. Electrical and mechanical properties

The static decay time for a pure LLDPE and its composites is presented in Table 3.1. MJ composites with a CNF content of 5 wt% or lower showed an unacceptably long static decay time. For more than 10 wt% MJ fiber content, the nanocomposites showed a static decay time below 2 seconds for both positive and negative charges. Thus, MJ composites containing 10 wt% CNF content are static dissipative. In contrast, for PRCVD and PR fibers, about 20 wt% CNFs were needed to obtain a static decay time that was less than 2 seconds.

Figure 3.1 presents the dependence of volume resistivity on the CNF content. For composites containing up to 10 wt% MJ fibers, the volume resistivity did not change significantly from the pure LLDPE value. However, at 15 wt% MJ fiber content, the

volume resistivity decreased over 5 orders of magnitudes to 8.9×10^3 ohm-cm. No further significant change was observed at 20 wt% MJ fiber content. In contrast, for PR and PRCVD composites, the volume resistivity started to decrease only at a higher content of 20 wt%. As CNF content increased further, a gradual decrease of volume resistivity was observed. At 35 wt% CNF content, the PR and PRCVD composites possessed volume resistivities of 4.2×10^3 ohm-cm and 2.4×10^5 ohm-cm, respectively.

Table 3.1. Static decay time of LLDPE composites

Decay time (s)		∞	0.01
CNF content	MJ composites	0 ~ 5 wt%	> 10 wt%
	PR composites	0 ~ 20 wt%	> 25 wt%
	PRCVD composites	0 ~ 20 wt%	> 25 wt%

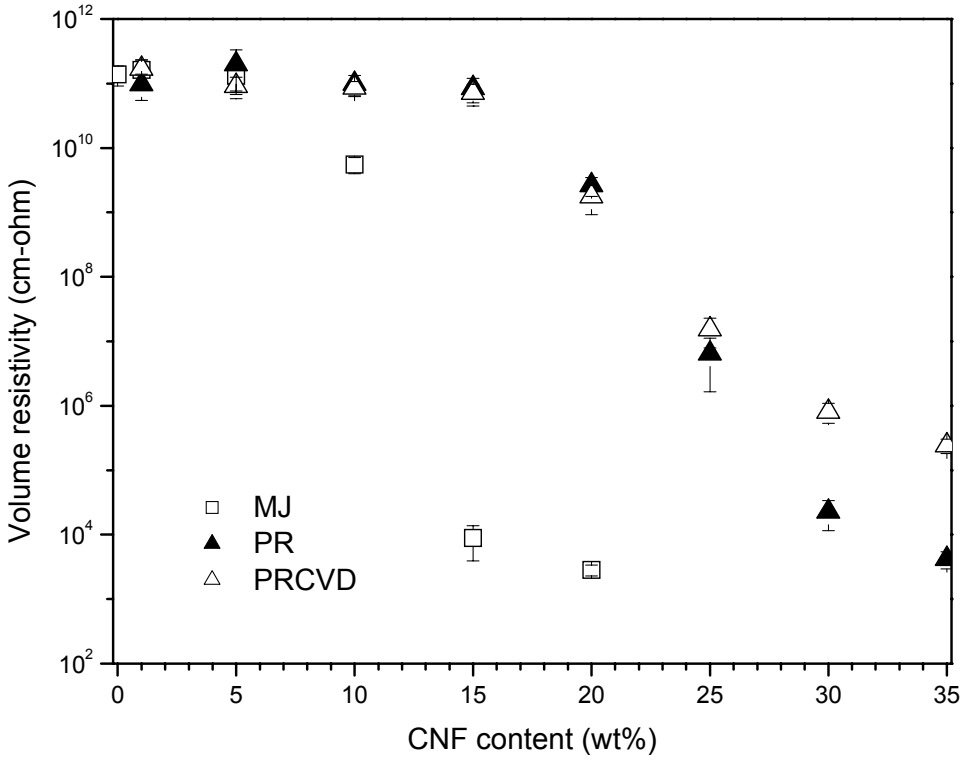

Figure 3.1. Volume resistivity of pure LLDPE and its composites.

Figure 3.2 displays mechanical properties of pure LLDPE and its composites containing up to 15 wt% CNF. As CNF content increased, tensile modulus increased for all three types of composites (Figure 3.2a), indicating that CNFs play a role of increasing stiffness of composite. It is likely that this is more significant in the presence of straight carbon nanofibers such as PR fibers due to their higher intrinsic stiffness. Tensile strength did not change significantly in going from pure LLDPE to composites containing 15 wt% CNF (Figure 3.2b). It has been reported that in a particular direction, tensile strength can be increased when CNFs are well oriented in the given direction [Kuriger et al., 2002a; Kuriger et al., 2002b]. It should be noted that tensile test samples used in this study were obtained from compressed molded plaques, implying that crystalline regions of LLDPE and CNFs in composites did not possess a preferred orientation.

Increasing CNF content for all composites led to decreasing strain-to-failure (Figure 3.2c). However, an interesting result was observed for composites containing MJ fibers in that even at 15 wt% fiber content, values as high as 460% were measured. In contrast, 15 wt% PR and PRCVD composites showed an approximate 100% strain-to-failure. This trend is counter-balanced by a higher increase of modulus for PR composites than for MJ composites. Incorporation of solid modifiers has been reported in the literature to significantly reduce strain-to-failure of resulting composites [Kumar et al., 2002; Zeng et al., 2004]. In composites, the decease in strain-to-failure of LLDPE depended on the type of CNFs, indicating a significance of modifiers on strain-to-failure of LLDPE.

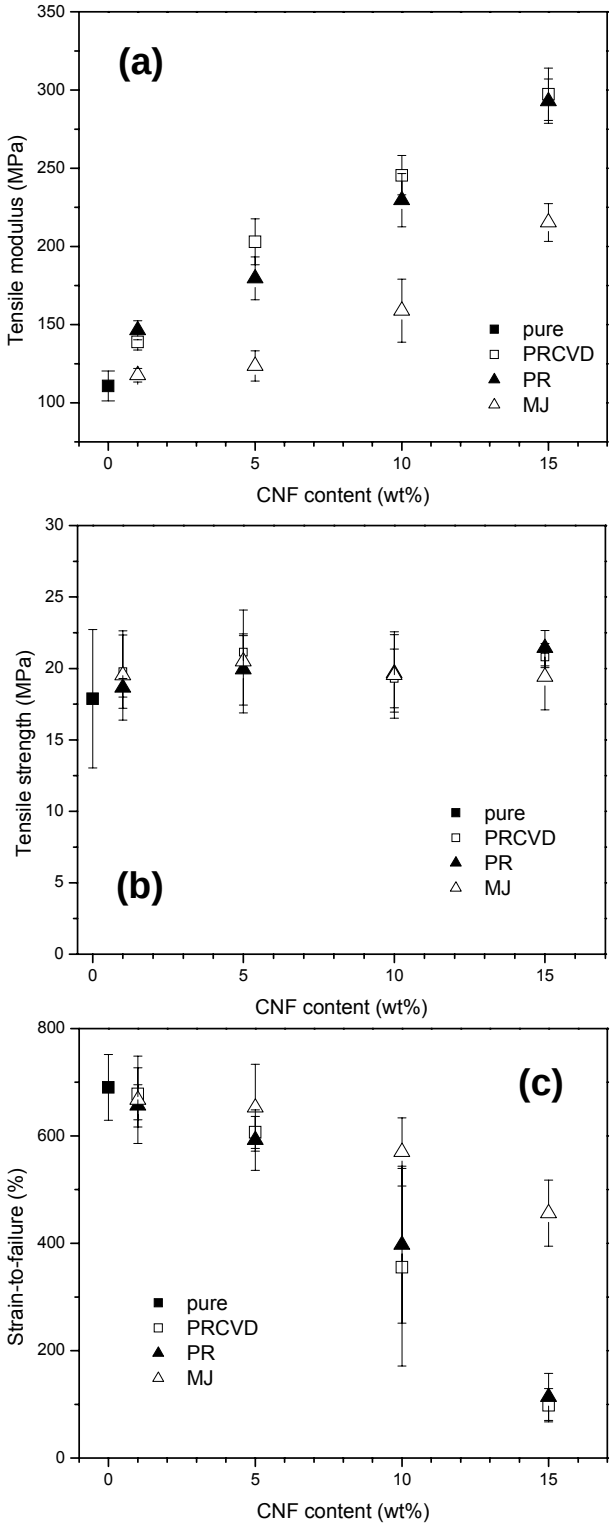

Figure 3.2. (a) Tensile modulus, (b) tensile strength, and (c) strain-to-failure of a pure LLDPE and its composites.

Interfacial bonding may have an important role in understanding the relatively higher strain-to-failure of MJ fiber. Surface morphology of CNFs influences the interfacial bonding with the matrix, which is critical for the development of mechanical properties of the composites. For better interfacial bonding with polymer matrices, fiber surface treatments such as oxidation treatment [Zhang et al., 2004], cryonic treatment [Zhang et al., 2004], and plasma treatment [He et al., 2005; Brandl et al., 2004] have been performed. Therefore, rough surfaces [Zhang et al., 2004] or chemical functional groups on the surface [He et al., 2005; Brandl et al., 2004] were obtained to influence interfacial bonding.

It is likely that interfacial bonding of MJ fibers with LLDPE matrix is better than that of PR fibers because MJ fibers possess a rougher surface. During deformation, e.g., tensile testing, this interfacial bonding of MJ composites, formed as a mechanical interlock, may prevent fibers from slipping past the LLDPE matrix, leading to elongation in an interphase area. After sufficient elongation of LLDPE in the interphase area, tensile stress transfers to the bulk matrix, which leads to a high strain-to-failure. In contrast, PR fibers possessing a smooth surface have a poor interfacial bonding with LLDPE. The interfacial bonds break before LLDPE is fully stretched during tensile testing. This interfacial debonding acts as defects, which propagate so that PR composites fail earlier than their MJ counterparts.

To investigate the dependency of electrical volume resistivity on CNF content, dispersion of CNFs in LLDPE was examined using SEM. Dispersion of nanometer scale modifiers in polymer matrices remains a significant research issue because strong van der

Waals bonding between nanofillers hinders their dispersion, which leads to agglomeration. This agglomeration may reduce the effect of CNFs on electrical conductivity of composites. SEM was performed on cross-sections of cryo-fractured composites containing 15 wt% each of PRCVD, PR, and MJ fibers. From Figures 3.3a-c, it is evident that CNFs are well dispersed in all composites and dispersion issue can be minimized as the source of different volume resistivities of different grades.

An interesting observation from insets of each micrographs is that PRCVD and PR composites showed holes, which may be introduced during cryo-fracture sample preparation, indicating that PRCVD or PR fibers pulled out. In contrast, MJ composites did not show any significant holes. It may be recalled from Chapter 2 (Figure 2.4) that MJ fibers are curled or coiled, whereas PRCVD and PR fibers are fairly straight. PRCVD and PR fibers pulled out during the sample failure. In contrast, MJ fibers will break rather than pull out because of their curled structure. This may explain the different morphology of cryo-fractured composites.

After cryo-microtoming of nanocomposites containing 15 wt% CNFs without staining, TEM was also performed to observe dispersion of CNFs. From Figures 3.4a-c, it is evident that CNFs are well dispersed in all composites. This is consistent with SEM analysis. Further TEM analysis will be presented later in section 3.3.4.

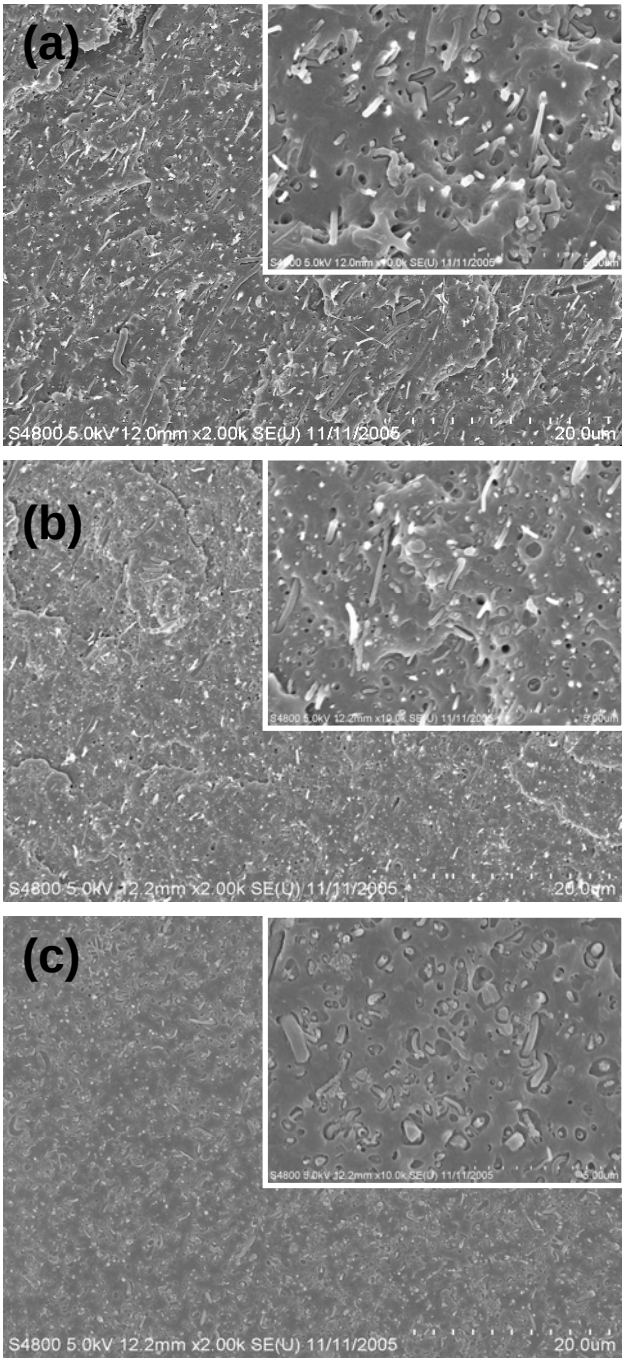

Figure 3.3. SEM micrographs of 15 wt% CNF/LLPDE composites containing: (a) PRCVD, (b) PR, and (c) MJ fibers. The inset micrographs are at a higher magnification.

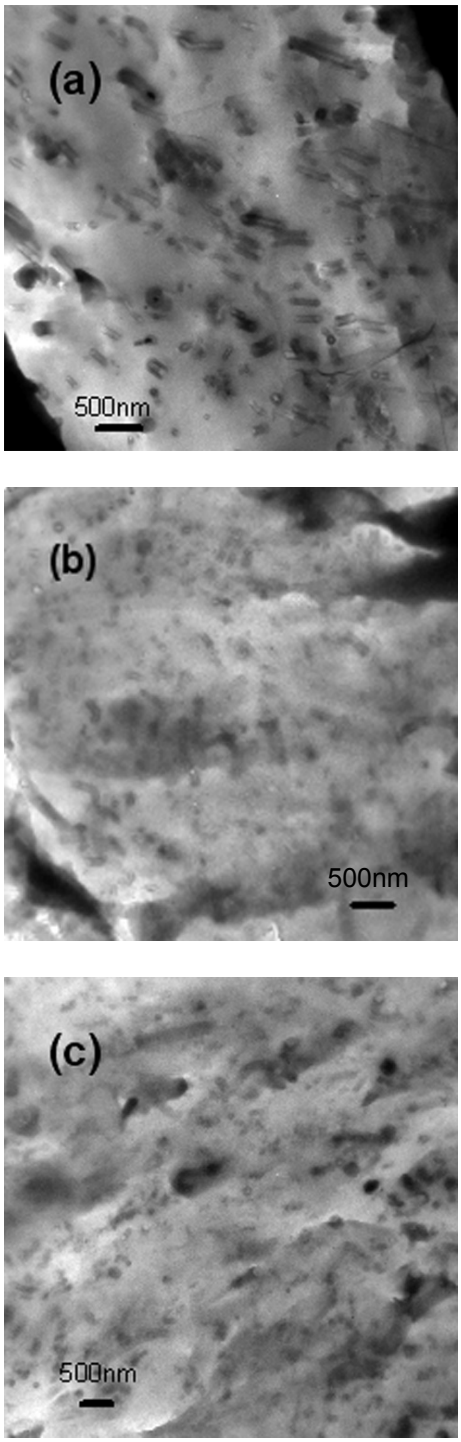

Figure 3.4. TEM micrographs of 15 wt% CNF/LLPDE composites containing: (a) PRCVD, (b) PR, and (c) MJ fibers.

The intrinsic volume resistivity of nanofibers in bulk is presented in Table 3.1. PRCVD fibers (1.71 ohm-cm) have higher volume resistivity than PR fibers (0.33 ohm-cm) and MJ fibers (0.43 ohm-cm). Also, SEM micrographs were used to measure nanofiber diameter, and the distribution is presented in Figure 3.5. As expected, the CVD layer led to thicker nanofibers, a lower aspect ratio, and a higher intrinsic volume resistivity in PRCVD fibers (as compared with PR fibers). This explains why PRCVD fiber composites showed a higher resistivity than did PR fiber composites.

However, MJ fibers were thicker than PR fibers and the intrinsic volume resistivity was higher than that of PR fibers (Table 3.2). But, MJ composites possessed a lower volume resistivity as compared with that of PR composites. Hence, microstructure of nanofibers can also play a role in the electrical behavior of composites. Because twisted/coiled MJ fibers have a higher probability to contact each other than do straight PR fibers, a lower percolation threshold can result from this higher degree of connectivity of MJ fibers, and can help to reduce volume resitivity of MJ composites.

Table 3.2. Properties of carbon nanofibers

	volume resistivity in bulk (Ω-cm)	diameter (nm)	length (μm)
PRCVD	1.71	148±60	10-100
PR	0.33	116±46	10-100
MJ	0.43	130±76	10-100

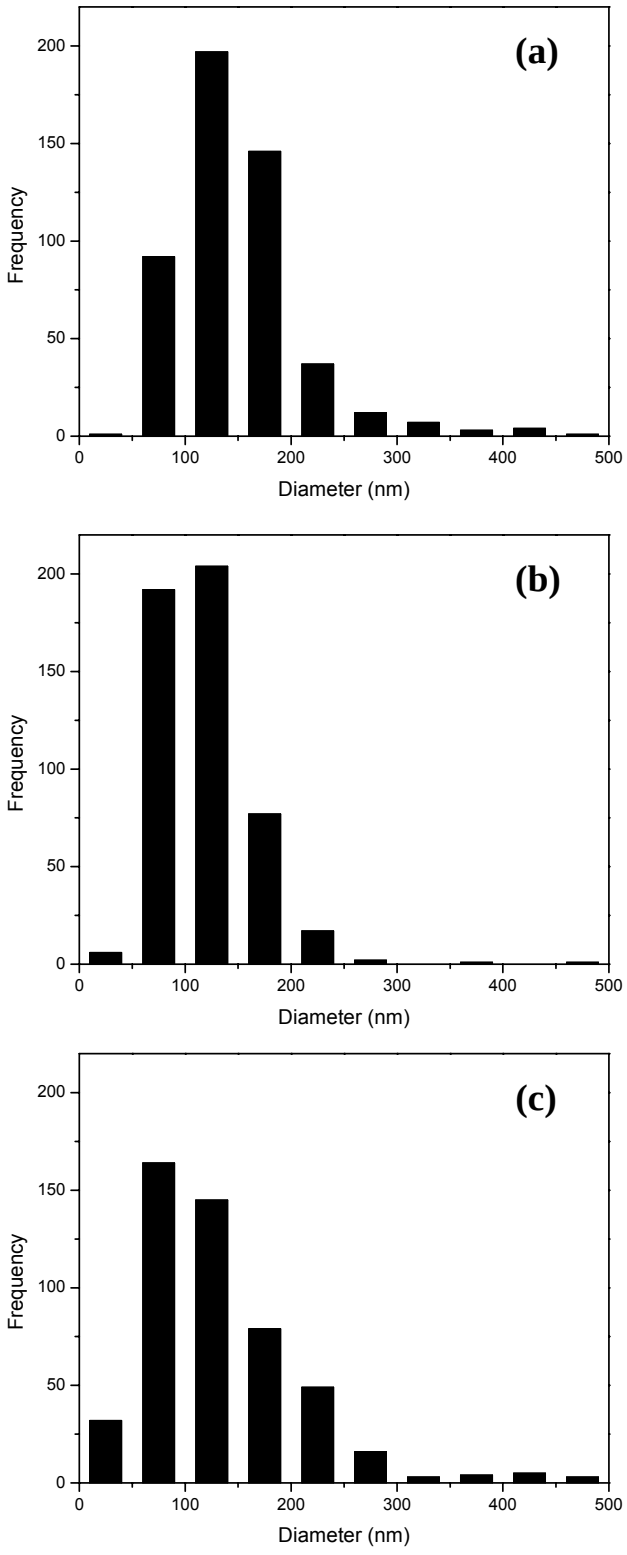

Figure 3.5. Histograms of diameter distribution of: (a) PRCVD (b) PR (c) MJ fibers.

3.3.2. Crystallization kinetics

To investigate additional effects that CNFs have on the LLDPE matrix, crystallization behavior of LLDPE in the presence of CNFs was investigated. Using non-isothermal DSC analysis, melting peaks from the first heating scan are displayed in Figures 3.6a-c. Pure LLDPE showed two melting peaks, one at 115°C and the other at 121°C. With the addition of PRCVD and PR fibers, the melting peaks remained essentially unchanged. But, for MJ composites, the lower temperature peak (115°C) started to shift to higher temperatures (~120°C), and a broad peak appeared at ~ 109°C for higher nanofiber contents. Thus, 15 wt% MJ composite displayed one sharp (121°C) and one broad (~109°C) melting peak.

Since the first heating scans reflect thermal history experienced by the nanocomposites during sample processing steps, and may vary from one process to another, second heating scans were also obtained to investigate the crystallization behavior intrinsic to the polymer/CNF material system. Samples were held at 190°C for 10 min after the first heating scan to remove prior thermal history and then slowly cooled at 10 °C/min. The cooling crystallization thermograms are presented in Figure 3.7, followed by the second heating scans at 10°C/min in Figure 3.8. During cooling, DSC thermograms of pure LLDPE ('pure' in Figures 3.7a, b, and c) display one sharp peak at 104.7°C followed by a broad tail (towards lower temperatures). Thermograms for PR composites, displayed in Figures 3.7a and b, also showed a sharp peak and a broad tail with a small shifting of the peak temperature to higher values (104.5→106.7°C for PRCVD and 104.5→107.9°C for PR, as in Table 3.3).

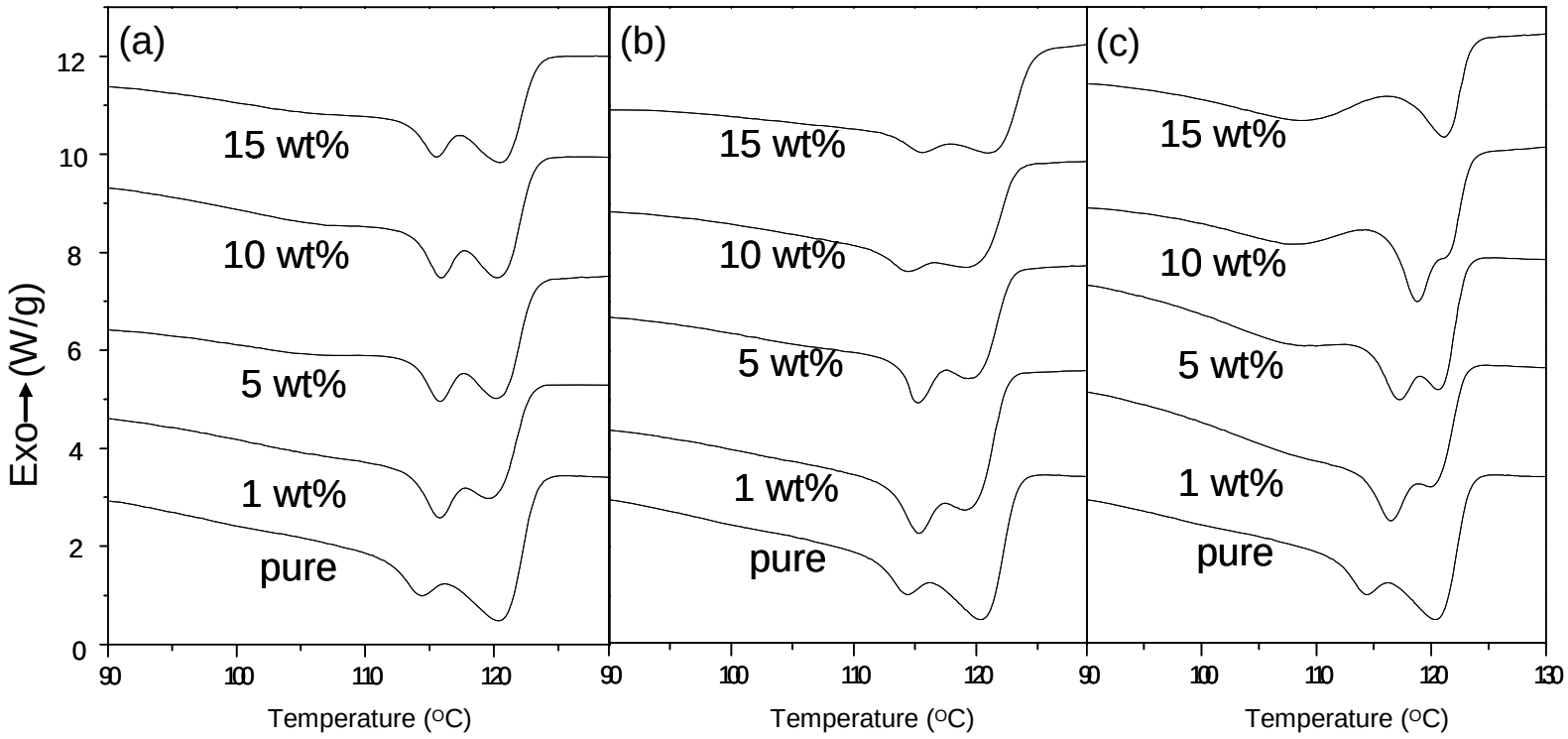

Figure 3.6. DSC thermograms (first heating) of pure LLDPE/ CNF composites at a heating rate of 10°C/min for: (a) PRCVD, (b) PR, and (c) MJ fibers.

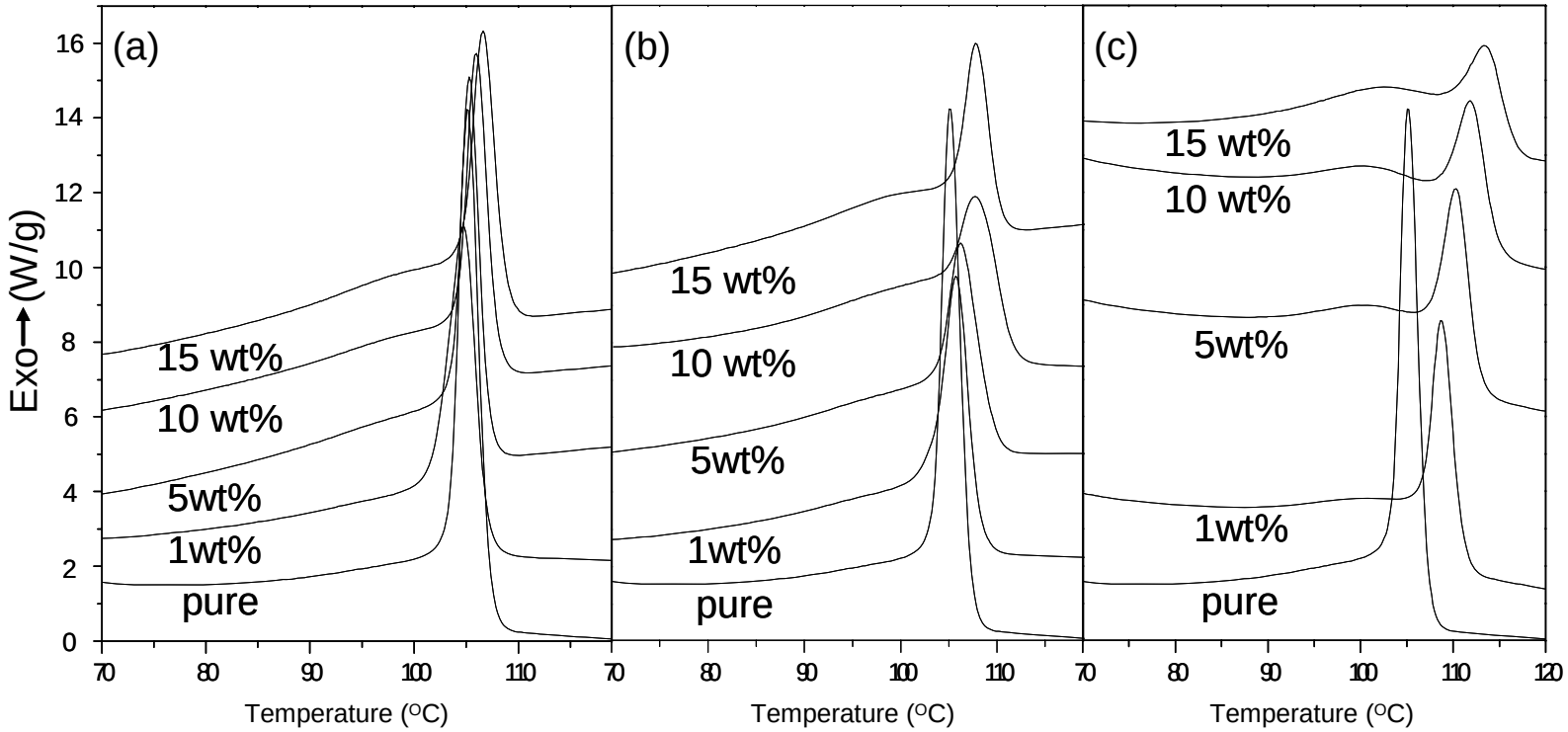

Figure 3.7. DSC thermograms (cooling) of pure LLDPE/ CNF composites at a heating rate of 10°C/min for: (a) PRCVD, (b) PR, and (c) MJ fibers.

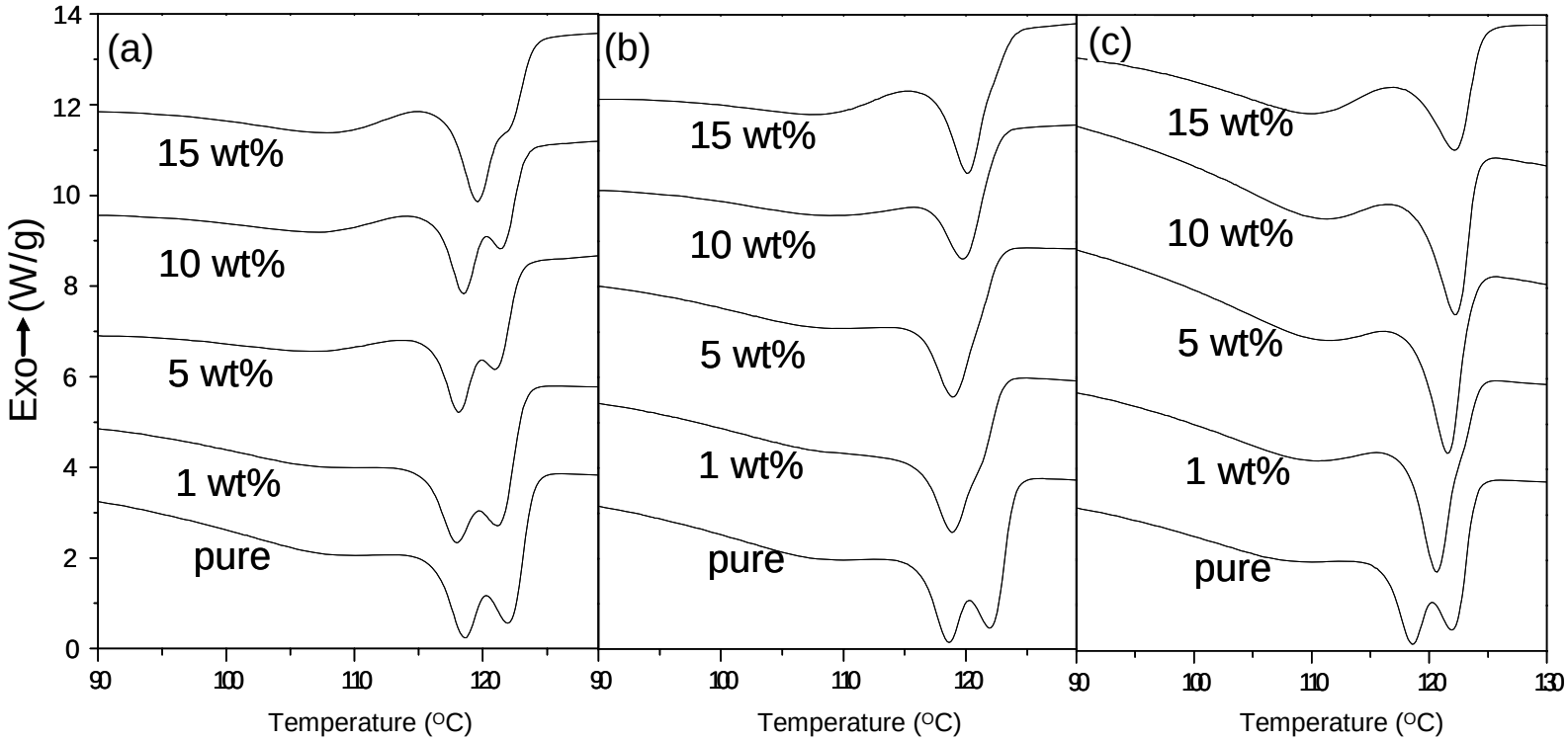

Figure 3.8. DSC thermograms (second heating) of pure LLDPE/ CNF composites at a heating rate of 10°C/min for: (a) PRCVD, (b) PR, and (c) MJ carbon nanofibers.

Table 3.3. The crystallization temperatures (T_c), melting points (T_m), and heats of crystallization measured by DSC for LLDPE and its composites containing PRCVD, PR and MJ fibers

Type	CNF content (wt%)	T_{c1}(℃)	T_{c2}(℃)	T_{m1}(℃) (shoulder)	T_{m2}(℃)	T_{m3}(℃)	ΔH_f(J/g_{poly})	*X* (%)
LLDPE	0	–	104.5±0.3	106.5±1.0	118.1±0.3	122.0±0.2	100.8±1.7	35.0±0.6
PRCVD	1	–	104.5±0.3	106.4±0.2	118.0±0.5	121.4±0.2	93.7±1.8	32.5±0.6
	5	–	105.2±0.3	107.1±0.5	118.3±0.2	121.4±0.2	94.5±2.0	32.8±0.7
	10	–	106.3±0.2	107.6±0.2	118.9±0.4	121.9±0.2	94.1±1.6	32.7±0.6
	15	–	106.7±0.2	107.6±0.4	119.2±0.3	122.1±0.1	94.3±1.9	32.7±0.7
PR	1	–	105.7±0.1	106.6±0.2	118.5±0.2	weak shoulder	95.2±1.4	33.0±0.5
	5	–	106.4±0.7	107.4±0.7	119.0±0.4	weak shoulder	92.1±1.5	32.0±0.5
	10	97.7±0.9	107.9±0.4	108.3±0.2	120.1±0.2	weak shoulder	97.2±1.6	33.8±0.6
	15	98.2±0.4	107.4±0.4	108.2±0.3	119.7±0.4	weak shoulder	94.8±1.0	32.9±0.4
MJ	1	99.5±1.0	109.1±0.5	109.0±0.2	120.6±0.1	weak shoulder	99.3±1.1	34.5±0.4
	5	100.0±0.2	110.3±0.1	109.6±0.2	–	121.4±0.13	99.0±5.1	34.4±1.8
	10	100.4±0.2	112.0±0.1	109.9±0.3	–	122.1±0.12	99.3±1.7	34.2±0.5
	15	101.8±0.1	113.6±0.2	110.2±0.5	–	122.4±0.05	99.3±4.9	33.2±1.7

In contrast, for MJ composites, a sharp peak (109.1-113.6°C) and another broad peak (99.5-101.8°C) were observed. It is evident that increasing CNF content shifted the peak temperature of crystallization to significantly higher values, and the broad tail of pure LLDPE became a broad peak.

Thermograms from second-heating are presented in Figure 3.8, and the measured transition temperatures (T_m) and heats of fusion (ΔH_f) are summarized in Table 3.3. Pure LLDPE displayed melting peaks at three temperatures: 106.5, 118.1 and 122.0°C. For all PRCVD composites, the three melting peaks were observed with an insignificant increase to higher temperatures. However, for PR composites, as nanofiber content increased, the meting peaks shifted to higher temperatures (106.6→108.2°C for the broad peak and 118.5→120.1°C for the sharp peak). Thus, 15 wt% PR composites showed a broad peak at ~108°C and a sharp peak at ~120°C.

For 1 wt% MJ composite, a broad lower melting peak at 109.0°C, a sharper melting peak at 120.6°C, and a shoulder at 122.2°C were observed (Figure 3.8c). It is likely that each of the melting peaks of pure LLDPE shifted to higher temperatures with the addition of MJ fibers. For 5 wt% and higher content of MJ fibers, two melting peaks were observed in DSC scans: one broad and one sharp. With an increase in CNF content, the broader peak at low temperature gradually became prominent without significant change in peak temperature (~109°C). In contrast, the sharp melting temperature increased (120.6→122.4°C) with increasing CNF content.

After deconvolution of DSC thermograms, the relative area under the broad melting peak (109°C) was calculated to be 73.5±1.3, 72.9±0.3, 76.9±0.2, and 80.8±0.5%

for pure LLDPE, PRCVD, PR, and MJ composites (1 wt%), respectively (Table 3.4). At 15 wt% CNFs, the values were found to be 75.9±1.0, 78.5±0.4, and 83.6±1.1 for PRCVD, PR, and MJ, respectively (Table 3.4). Representative deconvoluted thermograms for pure LLDPE and 1 wt% and 15 wt% composites are displayed in Figure 3.9. This indicates that with increasing CNF content, the broad melting peak became bigger whereas the sharp melting peak became smaller.

Table 3.4. The relative area of melting peaks after deconcolution of DSC thermograms for LLDPE and its composites containing PRCVD, PR, and MJ fibers

Type	CNF content (wt%)	% area (T_{m1})	% area (T_{m2})	% area (T_{m3})
LLDPE	0	73.5±1.3	14.9±0.4	11.6±1.7
PRCVD	1	72.9±0.3	16.2±1.6	10.9±1.3
	15	75.9±1.0	19.5±2.3	4.6±1.7
PR	1	76.9±0.2	21.8±0.6	1.4±0.6
	15	78.5±0.4	19.4±0.8	2.1±0.9
MJ	1	80.8±0.5	18.5±0.5	0.7±0.2
	15	83.6±1.1	–	16.4±1.1

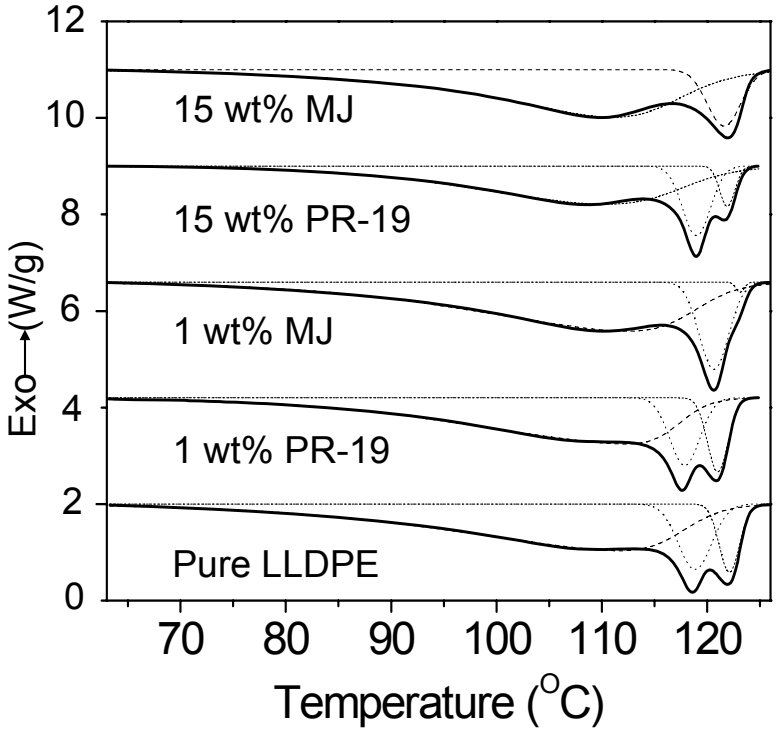

Figure 3.9. Representative deconvoluted thermograms (second heating) of pure LLDPE and its composites.

It has been reported in the literature that DSC endotherms of LLDPEs prepared by Ziegler-Natta catalyst display multiple melting peaks [Prasad, 1998; Springer et al., 1986; Schouterden et al., 1987; Puig et al., 2001]. The α–olefin short-chain branches are not introduced at regular intervals in the main LLDPE chain, and the intra- and inter-molecular heterogeneity leads to multiple melting peaks [Prasad, 1998]. The broader melting peak can be attributed to thinner lamellae of highly branched chain segments, whereas the sharper peaks arise from the long thick lamellae containing little or no branches [Prasad, 1998; Springer et al., 1986; Schouterden et al., 1987; Puig et al., 2001]. Defoor et al. observed by transmission electron microscopy (TEM) that thickest lamellae of LLDPE were mostly formed during the initial stage of the crystallization process [Defoor, 1992]. Later, at lower temperatures, thinner lamellae fill up the space between thick lamellae [Defoor, 1992]. In addition, depending on the α–olefin used as the co-monomer, a broad melting peak with a lower melting point around 106-110°C and higher peaks in the range of 120-124°C have also been observed [Prasad, 1998].

Further, for samples obtained after a slow cooling rate, the disappearance of the sharp melting peak of LLDPE prepared by Ziegler-Natta catalyst systems has been reported in the literature [Prasad, 1998]. Even though two sharp melting peaks for these LLDPEs were observed after a fast cooling rate of 10°C/min, only one melting peak appeared after a cooling rate of 5°C/min [Prasad, 1998]. The double melting peaks (generated during fast-cooling) can be attributed to melt-recrystallization, which is the reorganization of meta-stable lamellae into more stable thicker lamellae [Prasad, 1998]. A similar melting behavior was observed for LLDPE in Figure 3.10: for samples cooled

at the slow rate of 0.5°C/min, one sharp melting peak was observed, but an additional shoulder appeared in melting peaks for samples that had been cooled at moderate rates of 1 and 2.5°C/min. Further, two distinct melting peaks were observed for samples that had been cooled at the faster rates of 5 and 10°C/min.

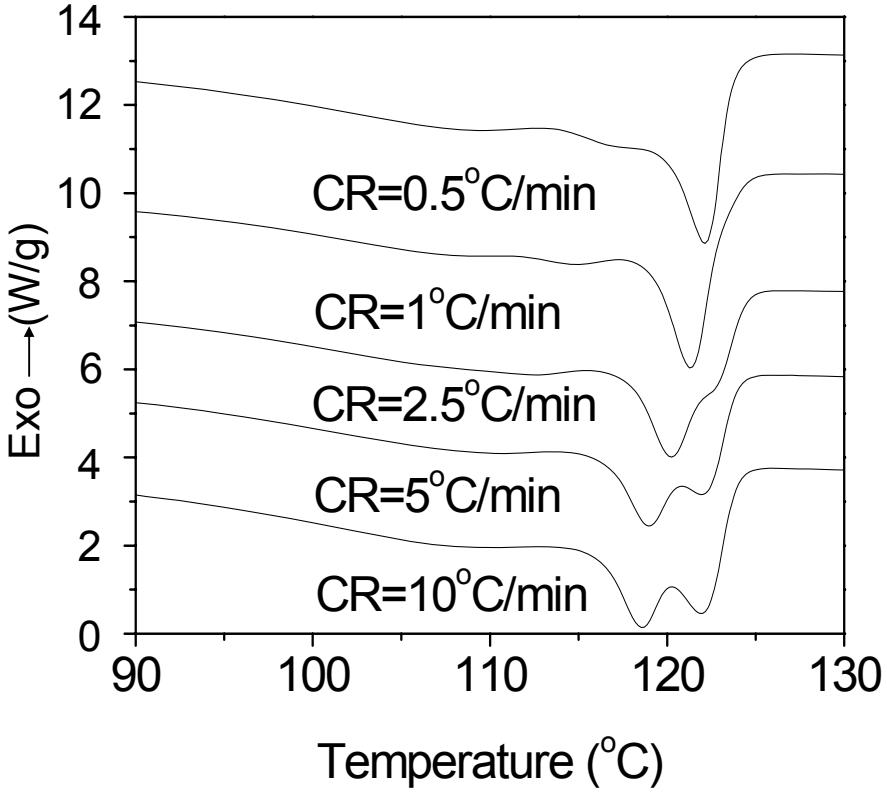

Figure 3.10. DSC thermograms (second heating) of pure LLDPE at a heating rate of 10°C/min after various cooling rates (CR).

For MJ composites, the 118°C melting peak shifted towards higher temperature, but became smaller. This suggests that CNFs lead to the development of some thicker, but fewer, LLDPE lamellae. However, the observation that the broad melting peak (109→110°C) became bigger with increasing CNF content suggests that CNFs also tend to generate additional thinner LLDPE lamellae. Note that as CNF content increases, the broad peak becomes more intense in the cooling scan as well (Figure 3.7c). It is evident that thin lamellae, likely associated with a broad melting peak in the second heating scan, were formed at lower temperature during cooling with the addition of CNFs.

Non-isothermal crystallization kinetics were modeled using the non-isothermal Avrami analysis for pure LLDPE and its composites containing 1 wt% of CNFs. The extent of isothermal crystallization, *X(t)*, may be related to time as:

$$1 - X(t) = \exp(-Z_t t^n)$$

where n is the Avrami crystallization exponent, and Z_t is a crystallization rate constant [Sperling, 2001]. For non-isothermal crystallization, the modified time t is related to temperature T as $t = (T_o - T)/\phi$ where T_o is the onset temperature of crystallization and ϕ is the cooling rate. From the Avrami plots (Figure 3.11), n values were calculated to be 2.87±0.01, 2.90±0.11, and 2.83±0.05 for pure LLDPE, 1 wt% PRCVD, and 1 wt% PR composites, respectively. The crystallization exponents for pure LLDPE and PR composites were statistically not different (at 95% confidence interval). Also, these values were similar to those reported in the literature for polyethylene, a range of 1.7-3.8 [Gupta et al., 1994; Rabesiaka and Kovacs, 1961]. However, MJ composite showed two slopes that led to two crystallization exponents: the steeper curve led to values of

2.61±0.03, whereas the shallower curve resulted in 1.13±0.03. It is evident that the second slope resulting from the broad peak (99.5°C) observed in Figure 3.7c indicates slower crystallization.

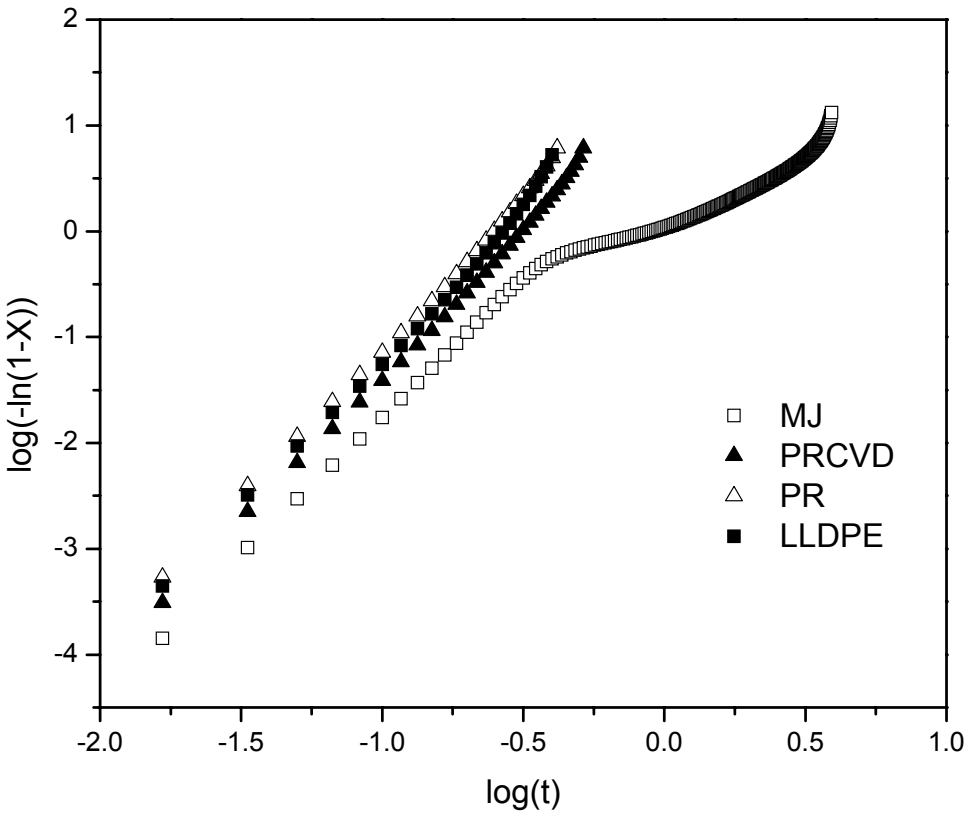

Figure 3.11. Avrami plots of pure LLDPE and 1 wt% composites containing PRCVD, PR, and MJ fibers.

From the second heating scans, the crystallinity of all samples was determined by dividing the ΔH_f^o of crystallization by ΔH_f^o value of 288 J/g for LLDPE [Mirabella and Bafna, 2002], and the results are summarized in Table 3.3. The normalized ΔH_f values reported are based on the polymer content (since fibers do not crystallize). The overall crystallinity of the LLDPE phase (35.0-32.7%) did not change significantly with increasing CNF content (Table 3.3).

Isothermal crystallization of pure LLDPE and 1 wt% composites was conducted in the temperature range from 112 to 116°C. When samples were quenched to the desired temperature, there was a lag between the sample temperature and programmed temperature. This temperature transience has also been reported in the literature and results from the heat capacity of materials and non-isothermal crystallization [Feng and Kamal, 2005]. Therefore, the initial non-isothermal heat effects are subtracted from the overall heat effects [Feng and Kamal, 2005]. By following this procedure, corrected isothermal scans, such as those plotted in Figure 3.12, were obtained. However, due to the removal of initial heat effects, the crystallinity value from isothermal scans is less than that measured from non-isothermal crystallization. For poly(ethylene-*co*-1-hexene) synthesized by metallocene catalyst, Janimak and Stevens [1999] observed that the crystallinity measured from isothermal scans at 110°C was about half of that measured from non-isothermal scans. Since the crystallinity measured from isothermal scans was about a quarter of that measured from non-isothermal scans in the present study, it is believed that these isothermal results do not accurately represent crystallization kinetics, and will not be discussed further.

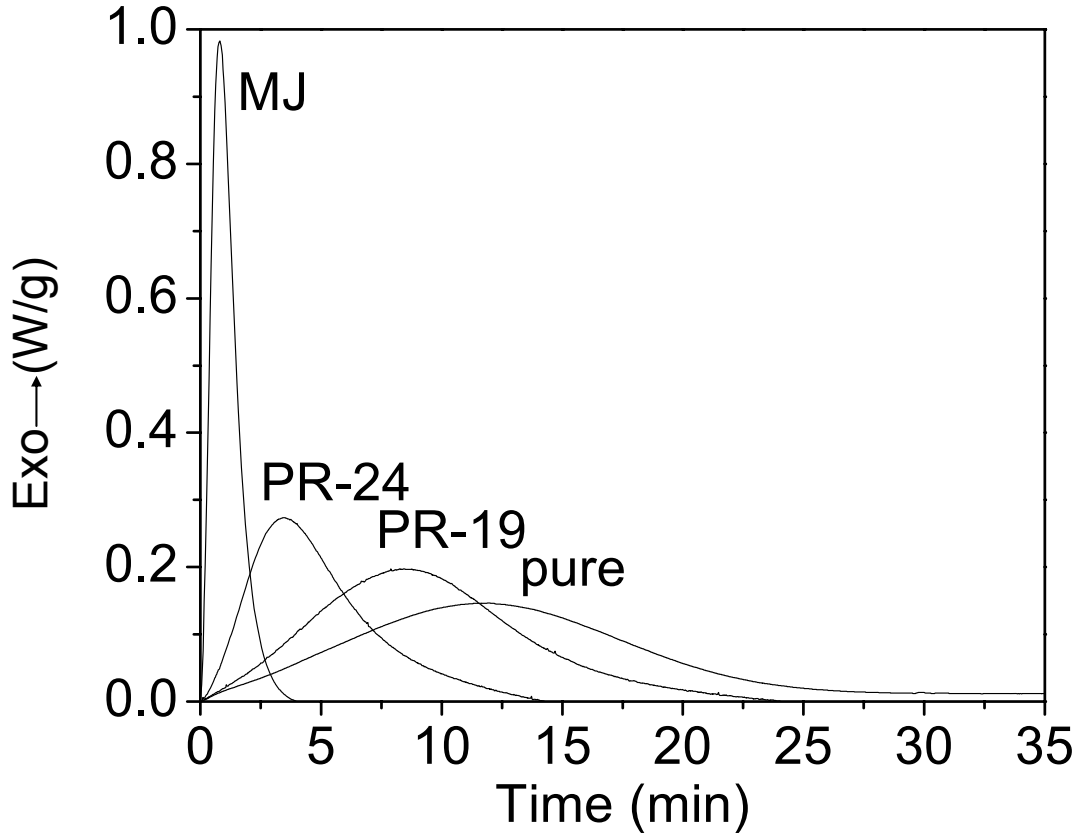

Figure 3.12. Isothermal crystallization exotherms at 114°C for pure LLDPE, and 1 wt% composites containing PRCVD, PR and MJ fibers.

The integrated azimuthal profiles (2θ scans) from WAXD of pure LLDPE, 1 wt% and 15 wt% MJ composites are displayed in Figure 3.13a. The peaks associated with (110), (200) and (020) planes of orthorhombic LLDPE crystals appear at 2θ values of 21.7±0.2°, 24.1±0.2° and 36.5±0.2°, respectively. For 15 wt% MJ composites, a peak appears at $2\theta \approx 26°$ from the (002) graphene planes of CNFs, but the peak positions for LLDPE did not change significantly for any CNF composites. Further, as illustrated in Figure 3.13b for 1 wt% CNF content, no measurable change of peak positions was observed with different CNFs. These diffractograms indicate that CNFs did not significantly affect the orthorhombic crystal structure of LLDPE.

Overall crystallinity of LLDPE was also calculated by WAXD in pure polymer samples and those containing 1 wt% CNFs, based on the sum of (110) and (200) peak areas as a ratio of the total area [Aggarwall and Tilley, 1955; Orsini et al., 1963; Beach and Kissin, 1984]. The degree of crystallinity was found to be 36±2, 34±2, 34±3, and 35±2%, for pure LLDPE, PRCVD, PR and MJ 1 wt% composites, respectively. These WAXD-based values are consistent with those obtained from DSC (Table 3.3), and indicate that there was not any appreciable difference in the overall degree of crystallinity with the addition of various CNFs.

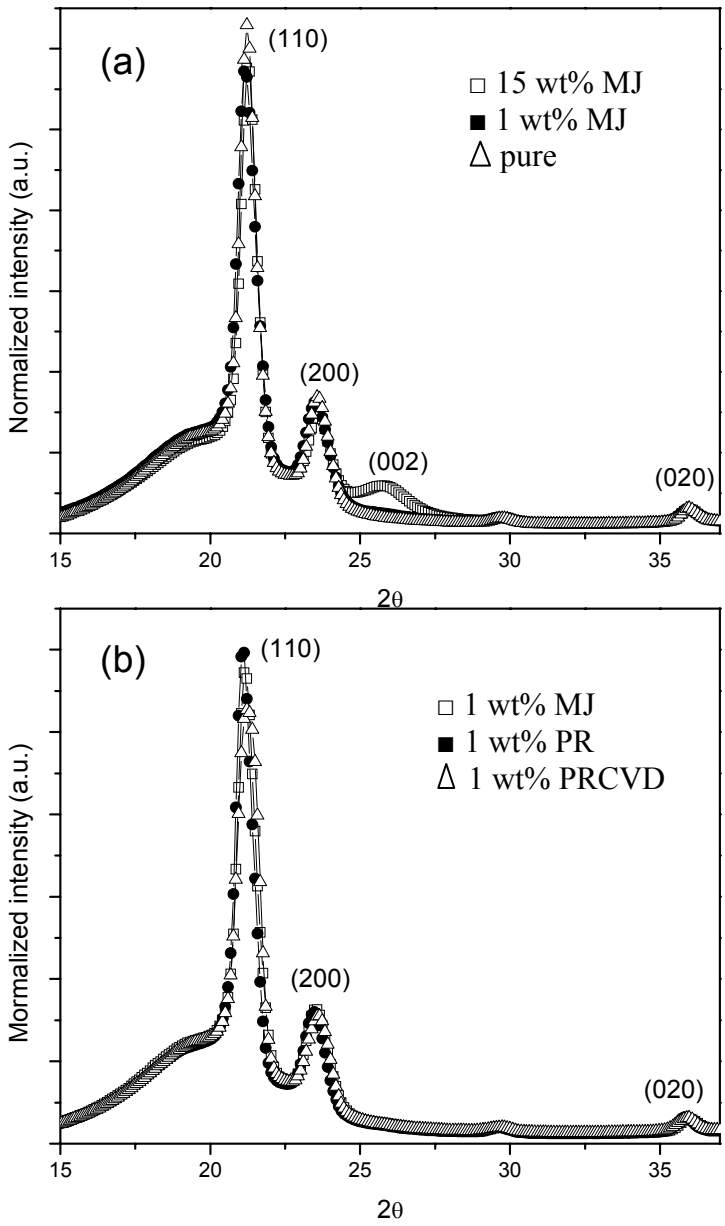

Figure 3.13. Integrated azimuthal profiles (2θ plots) for: (a) pure LLDPE, and 1 wt% and 15 wt % MJ composites and (b) LLDPE/1 wt% composites containing PRCVD, PR and MJ fibers.

3.3.4. Microstructure and morphology

Figures 3.14a-h display TEM micrographs of LLDPE lamellar structure in pure and composite forms (15 wt% of PR-19, PR-24, and MJ CNFs) at two different magnifications. Lamellae growing perpendicular to the surface of CNFs were observed in nanocomposites, indicating the presence of transcrystallinity. The nominal thickness of polymer lamellae were 10.0±1.3 nm, 10.2±1.5 nm, 10.3±1.9 nm, and 10.3±2.0 nm for pure LLDPE, PRCVD, PR, and MJ nanocomposites, respectively. These values were not significantly different in the pure versus nanocomposite form. However, a broader distribution of LLDPE lamellar thickness was observed in nanocomposites compared to that in the pure state (Figure 3.15a-d). This is also consistent with results reported by Wu et al. [Wu et al., 2002] who showed the preferential crystalline growth of HDPE at the end of carbon fibers was a consequence of surface roughness. Thus, as expected, surface topography of the nanoreinforcement plays an important role in the crystallization behavior of the polymer.

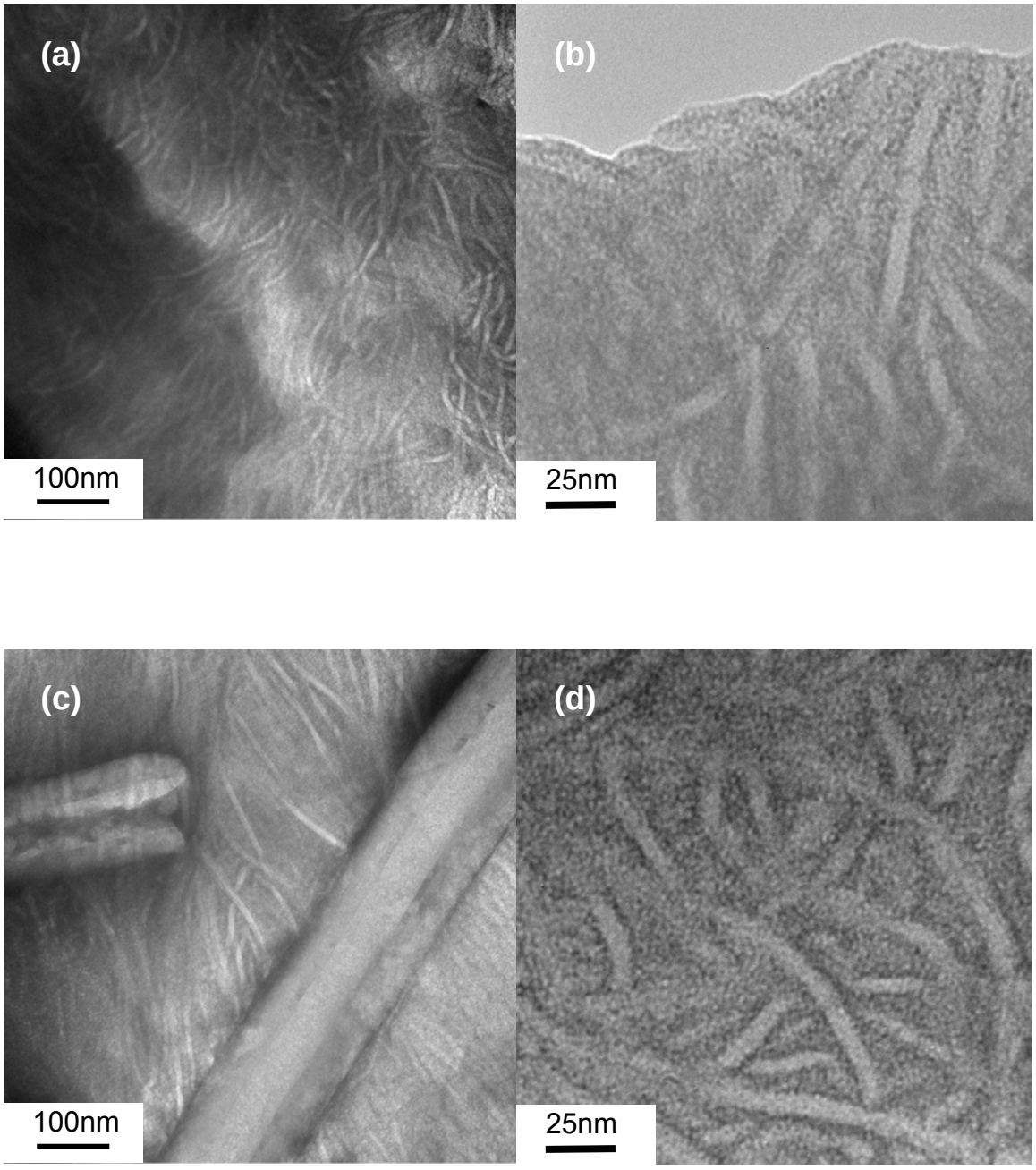
(a)
100nm
(b)
25nm
(c)
100nm
(d)
25nm

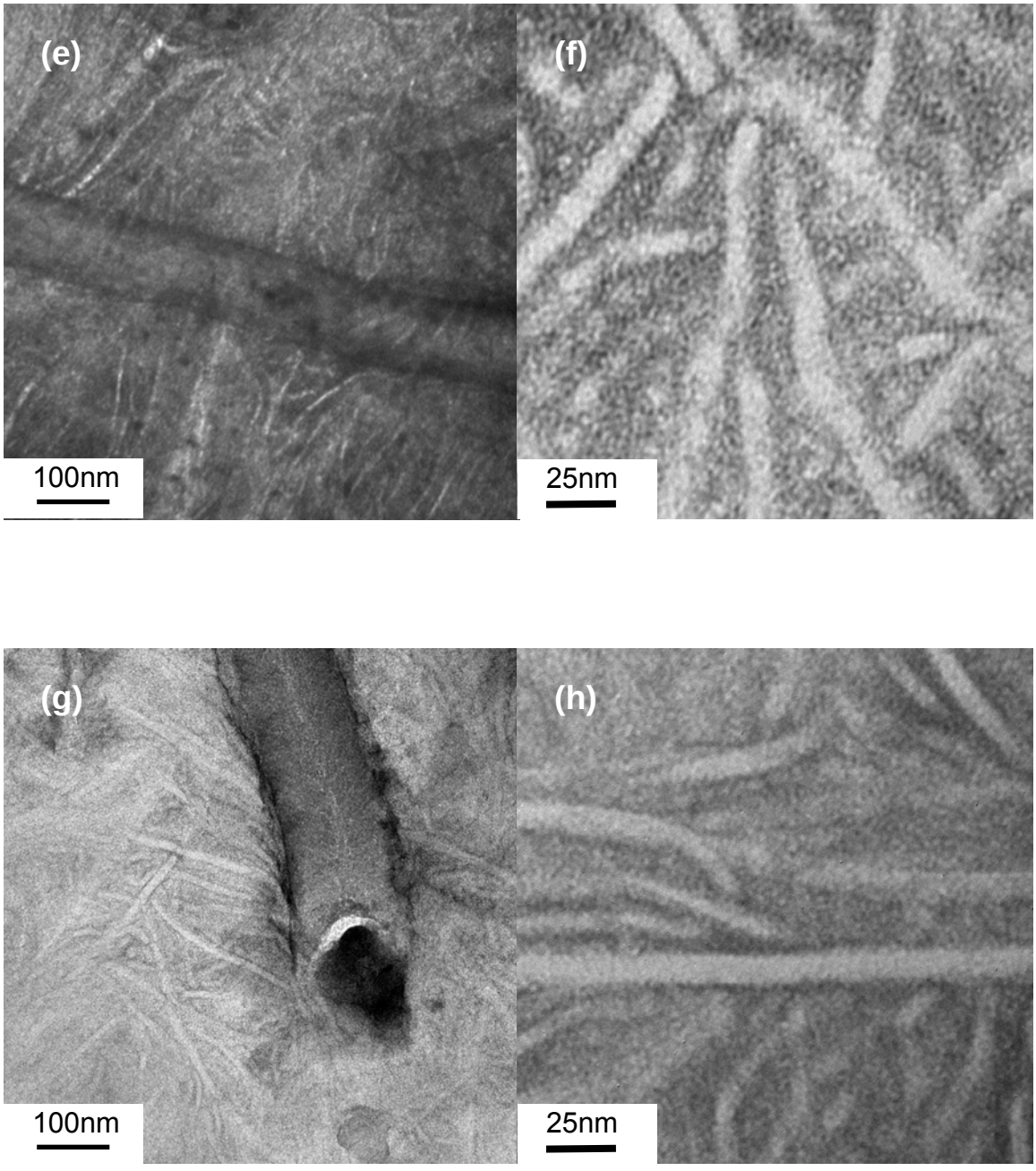

Figure 3.14. Transmission electron micrographs of: (a) pure LLDPE, and LLDPE/15 wt% composites containing (c) PR-19, (e) PR-24 and (g) MJ fibers. (b), (d), (f), and (h) are in high resolution for (a), (c), (e), and (g), respectively.

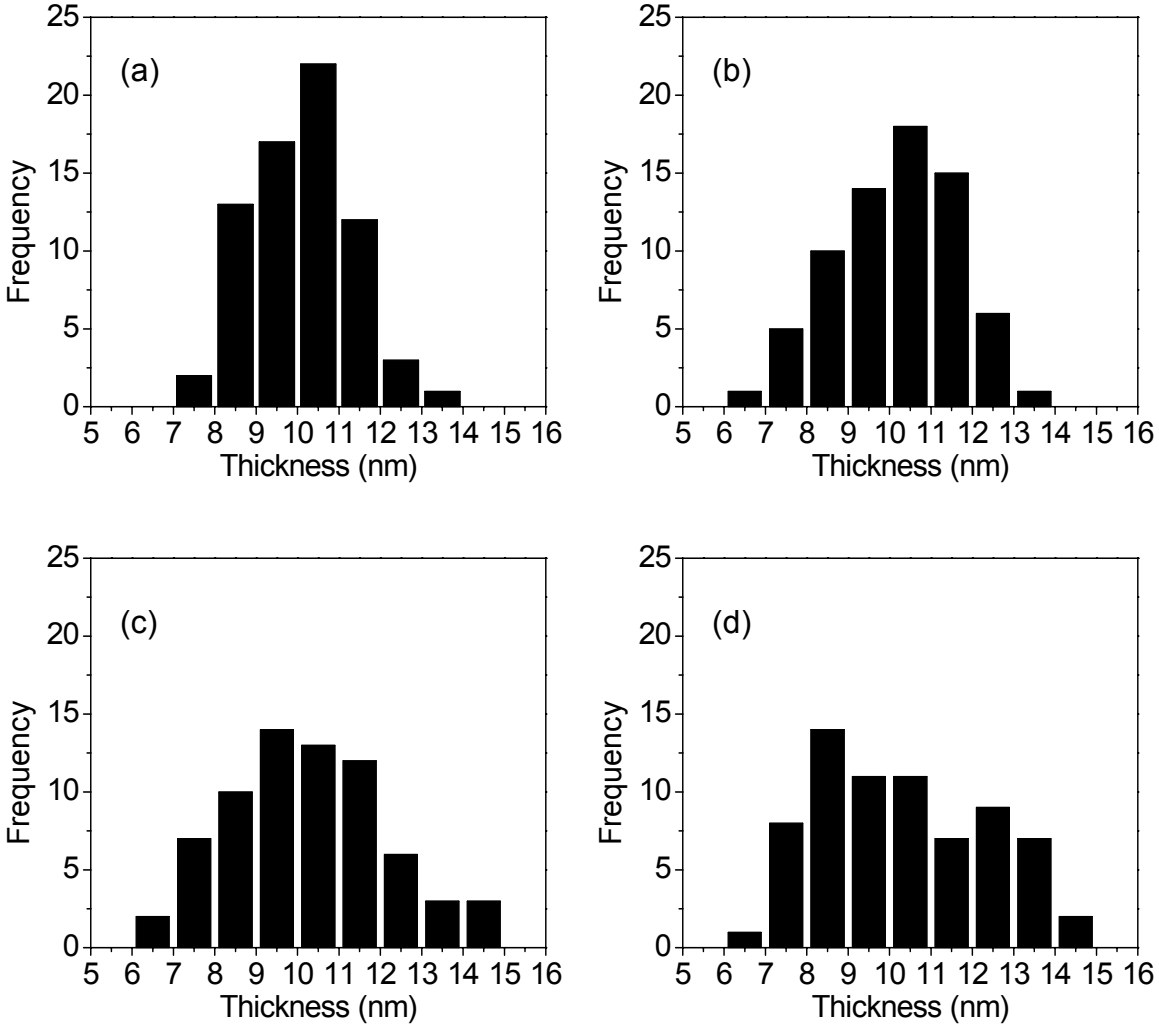

Figure 3.15. Histograms of thickness distribution of LLDPE lamellae in: (a) pure, and 15 wt% composites containing (b) PRCVD, (c) PR, and (d) MJ fibers.

3.4. Conclusions

A significant drop in volume resistivity was observed for nanocomposites starting with 15 and 25 wt% of MJ and PR fiber contents, respectively. It was observed that twisted/coiled MJ fibers led to better inter-fiber connectivity and reduced percolation threshold, compared to fairly straight PR fibers. Strain-to-failure decreased from 690% for pure LLDPE to 460% and 120% for 15 wt% MJ and 35 wt% PR composites, respectively. This indicates that the interfacial bonding of the LLDPE matrix with MJ fiber is better than that with PR fibers, resulting from the rougher surfaces of MJ fibers.

WAXD results indicate that the overall crystallinity of LLDPE did not change significantly in the LLDPE/CNF nanocomposites. Non-isothermal DSC analysis of nanocomposites indicated that 15 wt% PRCVD composites exhibited three melting peaks, similar to those for pure LLDPE. However, one of the three melting peaks for LLDPE disappeared in the presence of MJ fibers. Further, the observation that the broad melting peak becomes more intense with increasing MJ fiber content suggests that MJ fibers lead to thinner LLDPE lamellae. TEM micrographs of nanocomposites revealed transcrystalline growth of LLDPE on CNF surface, and a slightly broader distribution of lamellar thickness. In Chapter 2, STEM studies revealed a rougher surface morphology of the MJ fibers relative to that of PR fibers. A larger specific surface area of MJ fibers relative to that of PR fibers (BET studies of Chapter 2) and the rougher surface of MJ fibers contribute toward the different crystallization behavior of the nanocomposites.

CHAPTER 4

EFFECT OF CARBON NANOFIBERS ON THE ANISOTROPY OF AN AROMATIC THERMOTROPIC LIQUID CRYSTALLINE POLYMER

4.1 Introduction

In contrast to flexible-chain polymers (viz. LLDPE), semi rigid-rod thermotropic liquid crystalline polymers (TLCPs) provide unique properties such as high strength and low oxygen/water vapor permeability. These superior properties make them promising candidates for high performance molding and extrusion applications [Foldberg et al., 2003]. The degree of uniaxial orientation is typically very high, and this preferred orientation of the nematic phase imparts excellent tensile strength to TLCPs [Donald and Windle 1992]. The alignment of nematic domains has been reported even in moderately weak flows in prior studies (shear rates ~$1s^{-1}$) [Guo et al., 2005].

Fourier transform infrared microspectroscopy [Kaito et al., 1991] and wide angle X-ray diffraction (WAXD) [Kaito et al., 1991; Saengsuwan et al., 2003; Sun et al., 1991; Romo-Uribe and Windle 1996] studies on copolyester TLCPs indicate that the degree of orientation can be very high along the flow/processing direction. WAXD analysis of copolyester TLCPs fibers has revealed pseudohexagonal and orthorhombic structures depending upon the annealing conditions [Sun et al., 1991].

Unfortunately, this severe anisotropy of TLCP poses significant challenges for film applications since the high degree of orientation in the longitudinal direction leads to a high tensile strength in the longitudinal direction, but a low strength in the transverse

direction. Thus, an imbalance of in-plane properties, including tear resistance, is observed for such TLCP films. Another challenge faced in using TLCPs is their low electrical conductivity, which is inadequate for sensitive electronics packaging applications that need electrostatic dissipative materials. In this chapter, the role of carbon nanofibers (PR and MJ fibers) was investigated for the purpose of controlling the microstructure of the TLCP. The primary focus of this study was enhancing electrical conductivity while reducing anisotropy in the TLCP matrix. This chapter is based on a published paper [Lee et al., 2005]

4.2. Experimental

4.2.1. Materials

Two commercial grades of TLCPs were used in this study: Vectran V400P and Vectra A950 provided by Ticona, the technical polymers business of Celanese A. G.. Vectran V400P is an aromatic copolyester composed of 1,4-hydroxybenzoic acid (HBA), 2,6-hydroxynaphthoic acid (HNA), and other comonomers that provide selected meta-linkages [Linstid 2001]. Vectra A950 consists the composition of a random copolyester of 73 mol% 1,4-HBA and 27 mol% 4,6-HNA [Lin and Winter, 1988]. The molecular weight of Vectra A950 is approximately 30,000 and the polydispersity index is approximately 2. MJ and PR fibers were used as carbon nanofibers to incorporate into TLCPs. Details on these fibers were reported in Chapter 2.

4.2.2. Processing

TLCP pellets were vacuum dried for 24 h at 110°C before mixing. A Rheomix 600 mixer was used for intensive mixing of TLCP and 0.1-15 wt% of MJ fibers for 20 min at 210°C. Pure TLCP pellets without any nanofibers were also processed under the same condition; these samples served as the control material.

The compounded materials, both pure TLCP and nanocomposites, were extruded into rods using a circular die of 2.7 mm diameter at a low wall shear rate of 2 s^{-1} at 230°C. The diameter of the extruded rods was close to 2.7 mm since no draw-down was imposed. A compression press (Carver model 30-12-2T) was used for processing of the polymeric rods into molded samples using a rectangular mold cavity (150 mm × 14 mm × 0.3 mm). A compression temperature of 210°C, pressure of ~ 4 MPa, and a holding time of ~ 4 min was used for all of the molded samples. These conditions mimic those encountered in thermoforming processes that are used to produce packaging products. Further, we note that Vectran V400P polymer can be processed at temperatures as low as 210-250°C [Guo et al., 2005; Linstid et al., 2001], in contrast to the injection molding grade TLCP copolyesters (such as Vectra A950) that need to be processed at temperatures exceeding 300°C.

To prepare extrudates, the pure TLCP and the nanocomposites containing MJ fibers were extruded under identical conditions in a capillary rheometer (Instron Instruments) at 250°C using a circular die of 500 μm diameter. The nominal wall shear-rate was 55 s^{-1} for all extrudates. The extrusion temperature was slightly higher than that used in the molding process because it was not possible to extrude the nanocomposite

containing 5 wt% nanofibers at the lower temperatures of 210-230°C. A draw-down ratio of ~ 3 was used for all materials resulting in samples with a diameter of ~ 275 μm.

Also, V400P and A950, and their composites containing PR fibers, were extruded using a single screw extruder. A circular die of 1 mm diameter (L/D=10) was used at an apparent shear rate of 500 s^{-1}. For V400P, the temperature profile was 170, 200, 250, and 250°C in the feed, two metering sections, and die, respectively. The temperature profile for A950 was 230, 260, 300, 300°C. Extrudates were not post-drawn, and their nominal diameter was ~0.8mm.

4.2.3. Characterization

The static decay time was measured at 25°C using a static decay meter (Model 406D, Electro-Tech Systems, Inc.) to characterize the ability of molded samples to dissipate an induced surface charge. The test method was based on the Federal Test Method 101C, Method 4046, and Military Specification Mil-B-81705B that require 99 % of the induced charge to be dissipated in less than 2 s. The electrical resistivity was measured by a digital ohmmeter (Megohmmeter ACL 800) at 25°C. The electrical measurements were conducted at two different voltages (10 and 100 V) to account for low and high resistances and corrected for the specimen geometry. Ten replicate specimens were used for all electrical measurements.

To measure the mechanical properties, the extrudates for a pure V400P and its composites containing 0.1, 1, and 5 wt% MJ fibers were prepared. The tensile properties of extrudates were measured using an ATS Universal Tensile Tester 900 at 25°C. The

crosshead speed was 50 mm/min for all specimens. The tensile property of each extrudates was an average of the tensile data from at least eight specimens.

Thermal analysis was performed in a Perkin-Elmer differential scanning calorimeter (DSC). Samples were heated to 350°C at a rate of 20°C/min and held at that temperature for 10 min to erase thermal history of samples. Subsequently, samples were cooled to 50°C at a rate of 20°C/min and then heated up to 350°C again at a rate of 20°C/min for studying the effect of nanofibers on the non-isothermal crystallization.

The orientation in pure TLCP and composites was observed from the azimuthal intensity distribution of wide angle X-ray diffraction (WAXD) patterns obtained from an Osmic Micromax Cu K X-ray source with a collimator pinhole size of 0.3 mm. The distance from the sample to the detector was 10 cm. Diffracted patterns were captured on 2-D image plates, which were scanned using a Fuji BAS 1800 scanner. An exposure time of 30 min per image was utilized throughout the study. The Fraser-corrected WAXD diffractograms were analyzed using Polar® 2.6.5 software. Two replicate scans were performed on all samples.

4.3. Results and Discussion

4.3.1. Electrical and mechanical properties

As presented in Table 4.1, composites containing MJ fiber contents below 5 wt% displayed a static decay time greater than 2 s for both positive and negative charges, indicating that the material is static dissipative starting only at 5 wt % content of the MJ

fibers. Further, Figure 4.1 displays the dependence of volume resistivity on the MJ fiber content. At 5 wt% MJ fiber content, a significant volume resistivity drop (over 3 orders of magnitudes) occurred, which corresponds to the onset of percolation. Thus, static decay time test and volume resistivity showed consistent results in that 5 wt% MJ fiber content represents percolation threshold.

Table 4.1. Static decay time of pure V400P and MJ composites

CNF content (wt%)		0 ~ 4	5 ~ 15
Decay time (s)	Positive charge	∞	0.01
	Negative charge	∞	0.01

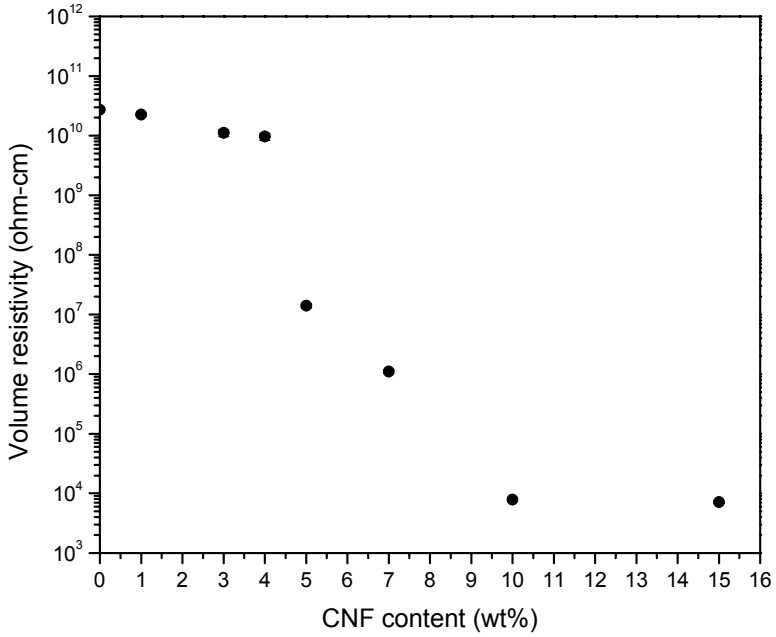

Figure 4.1. Volume resistivity of pure V400P and MJ composites.

Tensile modulus and strength as mechanical properties for pure V400P and its composites (0.1, 1, and 5 wt% of MJ fibers) were measured (Figure 4.2). There was no significant change in tensile modulus and strength in going from pure V400P to 1 wt% MJ composites. As the MJ fiber content was increased up to 5 wt%, tensile modulus decreased from 70 GPa to 38 GPa and tensile strength from 420 MPa to 200 MPa, respectively. A similar trend for strain-to-failure was observed in that elongation at break value was 1.5% for pure, 0.1 wt%, and 1 wt% MJ composites, which decreased to 1.1% for 5 wt% MJ composites.

One of the interesting characteristics of TLCP is the severe uniaxial orientation along the flow direction, which results in superior tensile properties of TLCPs. Significantly higher tensile properties were obtained for V400P specimens as compared to those of flexible-chain polymers. It should be recalled from Chapter 3 that tensile modulus and strength of LLDPE were 110 MPa and 20 MPa, respectively. However, the tensile properties of composites containing 5 wt% MJ fibers were drastically reduced, indicating that the structure of V400P changed significantly in the presence of MJ fibers.

To investigate structural changes of TLCPs with the addition of MJ fibers, non-isothermal DSC analysis of pure V400P and MJ composites was conducted. Thermograms are displayed in Figure 4.3 with baselines shifted vertically for convenience. From heating and cooling scans, it is evident that the glass transition occurs at 110°C for pure V400P, but no melting or crystallization transitions were observed during the heat up or cool down.

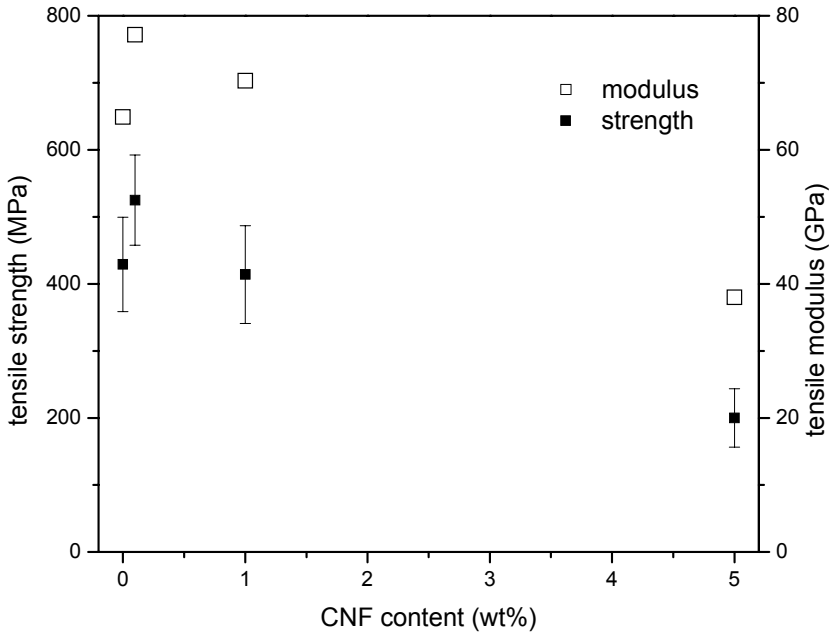

Figure 4.2. Tensile properties for pure V400P and MJ composites.

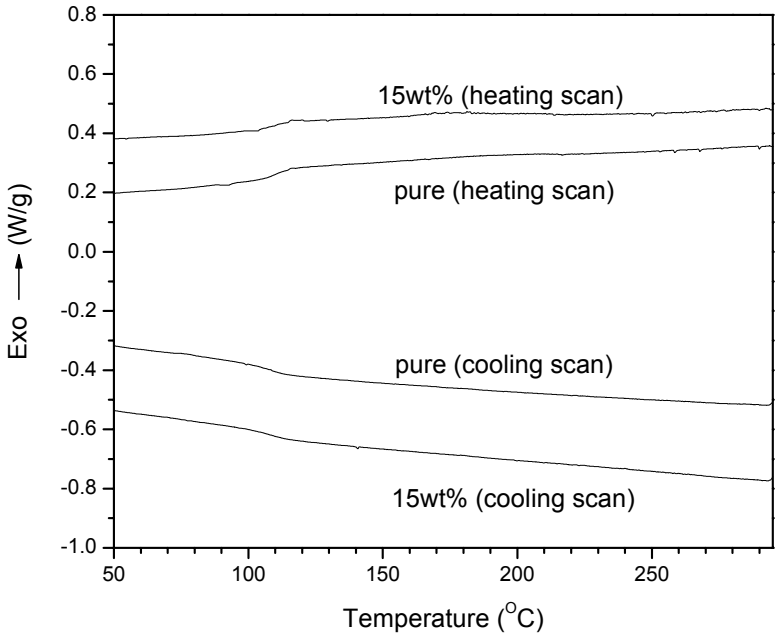

Figure 4.3. The DSC thermograms for pure V400P and 15 wt% MJ composite at a rate of 20 °C/min.

This indicates a non crystalline structure for solid V400P, which is consistent with that reported in earlier studies [Linstid et al., 2001; Guo et al., 2005]. Composites containing 15 wt% MJ fibers also showed only one transition at 110°C. These thermograms suggest that the effect of MJ fibers on thermal behavior of V400P is not significant.

4.3.2 Wide angle X-ray diffraction analysis

The 2D diffraction images for pure V400P and its composites containing 0.1 wt%, 1 wt%, and 5 wt% MJ fibers are displayed in Figures 4.4 and 4.5. Further, in Figure 4.6, the highest scattering intensity of the diffracted 2θ peak for pure V400P and MJ composite samples was observed around 2θ of 19.8° in all cases. For Vectra A950, literature studies indicate that this peak results from (110) planes associated with pseudo-hexagonal (PH) packing of TLCP polymer chains [Sun et al., 1991]. This structure is also referred to as orthorhombic form III, in which the lattice parameters are related as $a = \sqrt{3}b$.

A distinct (200) peak was not observed in the vicinity of $2\theta \approx 20°$, but a shoulder appeared in the 2θ region of 26-28° due to (211) planes. For V400P composite containing 5 wt% MJ fibers, there was a distinguishable peak in the broad shoulder region that was associated with graphene (002) planes from carbon nanofibers. It is noted that the location of the (110) peak for the extruded samples of neat Vectran V400P and MJ composites is similar to that observed for their molded counterparts.

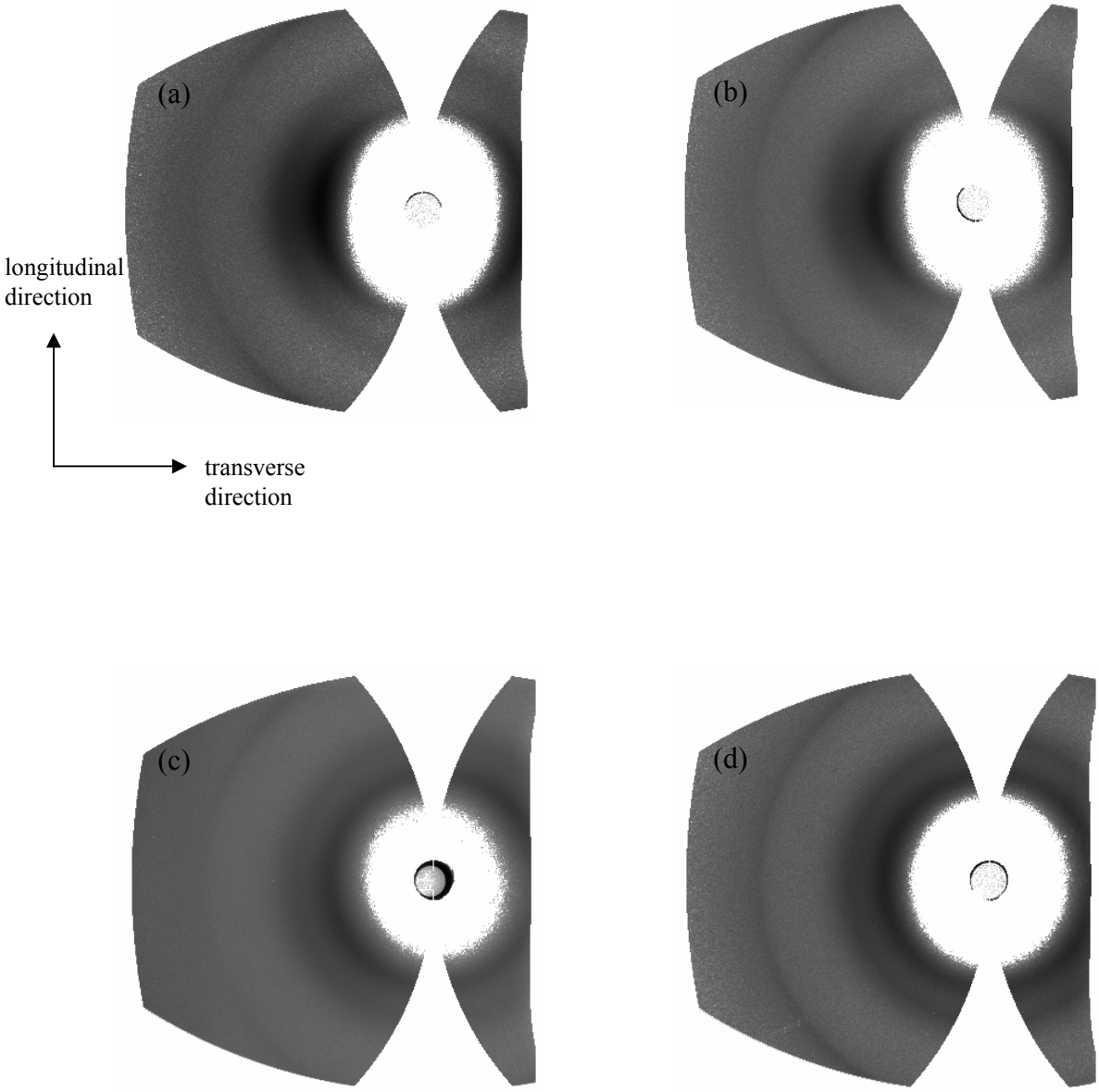

Figure 4.4. Wide angle x-ray diffraction patterns of molded samples from: (a) pure TLCP, (b) 0.1 wt%, (c) 1 wt% and (d) 5 wt% MJ composites.

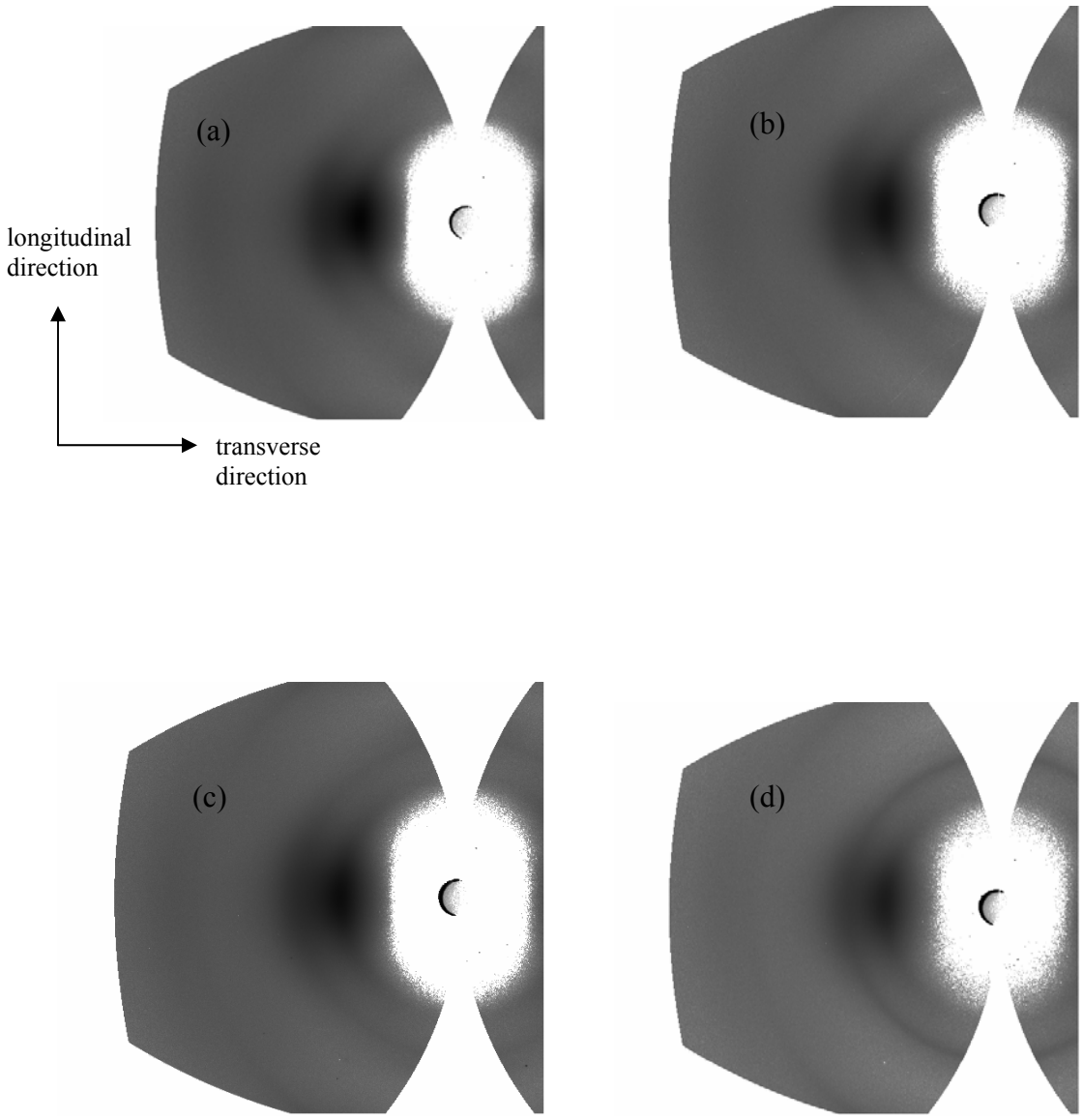

Figure 4.5. Wide angle x-ray diffraction patterns of extrudates from: (a) pure TLCP, (b) 0.1 wt%, (c) 1 wt% and (d) 5 wt% MJ composites.

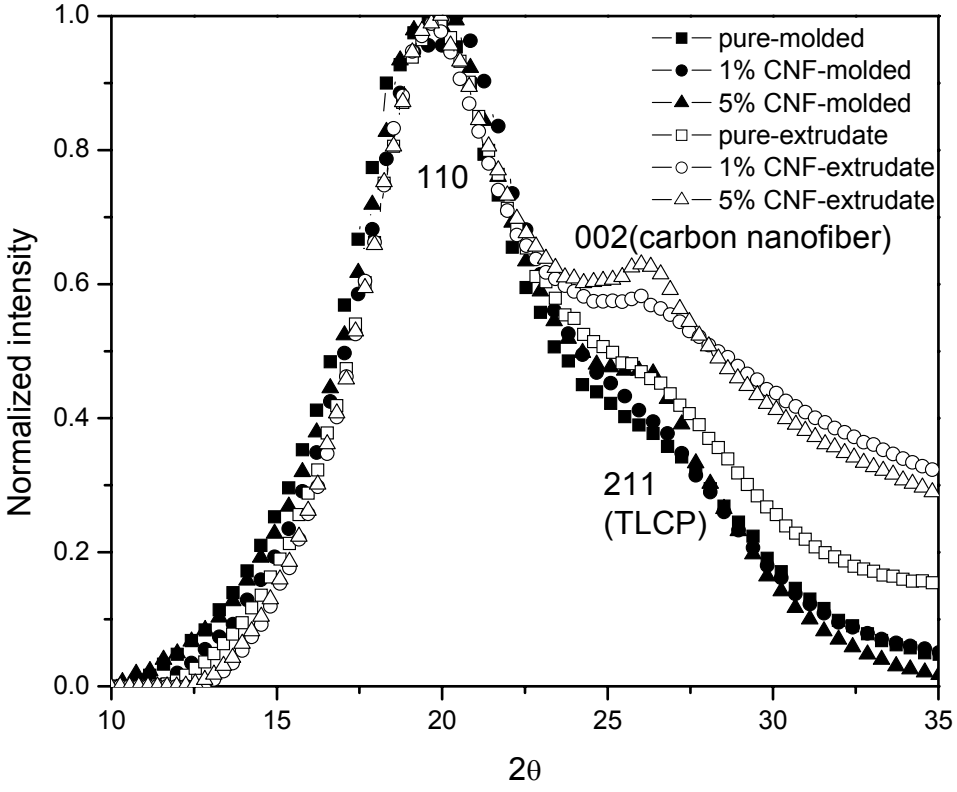

Figure 4.6. Radial (2θ) intensity profiles of molded and extruded samples from pure, 1 wt% and 5 wt% MJ composites.

The (200) peak associated with orthorhombic form I in Vectra A950 was never observed in Vectran V400P for the extruded samples that were also subjected to significant

extensional flow during draw down. The (200) peak did not develop in Vectran V400P samples even after annealing, in contrast to what has been observed for Vectra A950 type TLCPs [Sun et al., 1991; Wilson et al., 1993].

In the diffraction patterns of the molded samples (Figure 4.4), the (110) plane formed an intense arc for pure TLCP. In contrast, for the same set of planes, broader arcs were observed at 0.1 and 1 wt% MJ fiber contents that finally evolved to a uniform ring at a MJ fiber content of 5 wt%. It is noted that the shorter the arc length, the higher is the orientational order. Quantified azimuthal intensity profiles for (110) peak are displayed in Figure 4.7, which show that intensity profiles of pure TLCP and 0.1 wt % MJ fiber-modified TLCP were concentrated in the equatorial region. Higher contents of MJ fibers led to broader profiles. Therefore, the orientation of TLCP chains becomes less severe with higher content of MJ fibers.

The equatorial (110) peak was used to evaluate axial orientation of the samples. The second order Legendre polynomial or Herman's orientation parameter, is defined for orientation of polymer molecular chain as $f = 0.5\ (3\langle\cos^2\varphi\rangle - 1)$, where $\langle\cos^2\varphi\rangle$ is the ensemble-average value of the cosine squared of the angle φ between the longitudinal sample direction and a molecular chain axis [Dees and Spruiell, 1974]. According to this equation, the orientation factor can range from -0.5 to 1.0. For a random orientation, the value is zero. Further, 1.0 and -0.5 indicate perfectly oriented molecules parallel and perpendicular to the longitudinal direction, respectively.

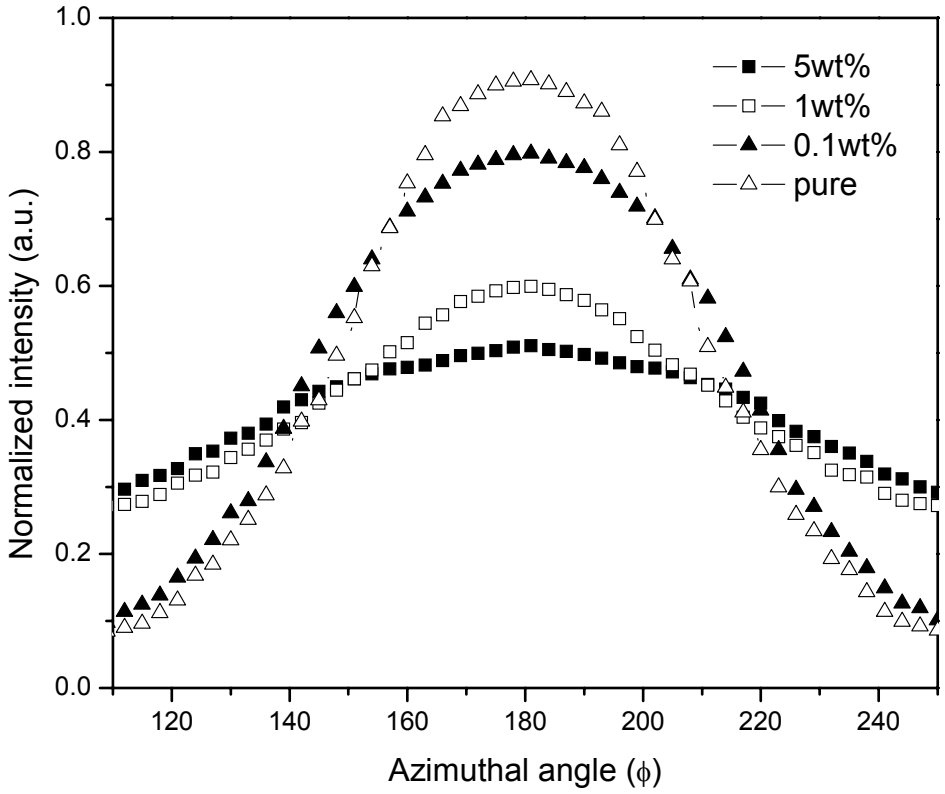

Figure 4.7. Azimuthal intensity profiles at 2θ = 19.8° of molded samples: pure V400P, 0.1 wt%, 1 wt% and 5 wt% MJ composites.

Herman's orientation parameter in the longitudinal direction was calculated for molded and extruded samples using POLAR software based on PH packing of V400P chains. The *f* values, displayed in Table 4.2, ranged between 0.51 (pure V400P) and 0.20 (5 wt% composites) for molded samples. At 1 wt % MJ fiber content, a significant decrease of the orientational order was observed. The 1 wt % and 5 wt % MJ composites showed lower *f* values than those displayed by pure V400P and dilute composites.

For extrudates, the azimuthal profiles were significantly sharper than those for molded samples, and the orientation parameter ranged from 0.85 for pure V400P to 0.71 for 5 wt% MJ composite as shown in Figure 4.8. The higher orientational order observed for extrudates (than for molded samples) may be attributed to flow-induced orientation and is well documented for strong flows, i.e., high shear rates and/or extensional flow field [Saengsuwan et al., 2003; Romo-Uribe and Windle, 1996]. However, for a given type of flow, we found that the addition of MJ fibers results in a reduced orientation order.

Table 4.2. Herman's orientation parameter for molecular alignment of pure V400P and its composites containing MJ fibers

CNF wt %	0	0.1	1	5
molded sample	0.51	0.50	0.27	0.20
extrudate	0.85	0.79	0.73	0.71

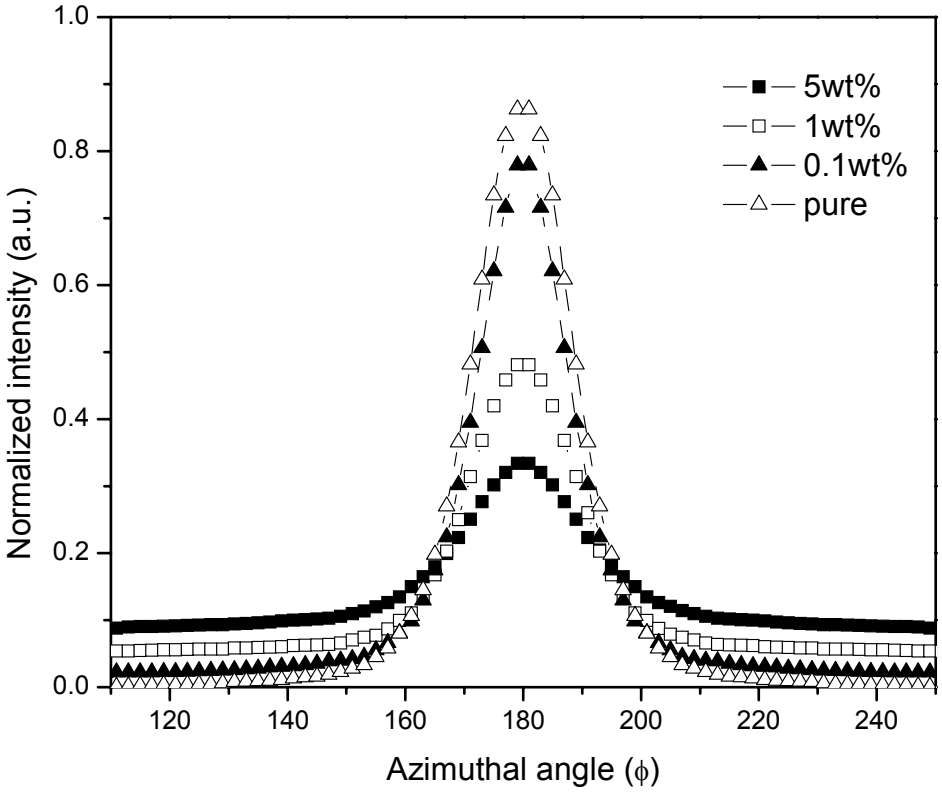

Figure 4.8. Azimuthal intensity profiles at 2θ = 19.8° of extrudates from pure TLCP, 0.1 wt%, 1 wt% and 5 wt% MJ composites.

Using Polar™ image analysis software, isotropic intensity distribution $I(\theta,\phi)$ could be resolved and the residual anisotropic intensity distribution obtained. Figures 4.9a and b display normalized radial distribution plots of the extruded samples with resolved anisotropic scattering intensity for pure V400P and V400P containing 5wt% MJ fibers, respectively. For pure V400P samples, there was no significant difference between total and anisotropic intensity profiles, indicating primarily anisotropic distribution of V400P molecules. In contrast, after subtracting isotropic contributions for 5 wt% MJ composite, the intensity of anisotropic (110) reflection ($2\theta \sim 19.8°$) due to V400P molecules decreased. Therefore, it is evident that incorporation of MJ fibers reduces anisotropy for the (110) planes. Further, it is noted that the carbon (002) peak almost disappeared from the resolved anisotropic profile. Thus, it can be inferred that the carbon nanofibers do not have a significant preferred orientation, and help in reducing the preferred orientation of neighboring TLCP molecules.

A decrease of molecular alignment in TLCP, in the presence of nanofibers, can also explain the drop in tensile strength that was observed earlier. Addition of nanofibers prevents the TLCP matrix from forming a highly ordered structure and reduces the anisotropy. A reduction of anisotropy of in-plane properties has also been reported in the literature for aromatic copolyesters (HBA/HNA and HBA/isophthalic acid (IA)/hydroquinone (HQ)) in the presence of glass fibers [Chivers and Moore, 1991].

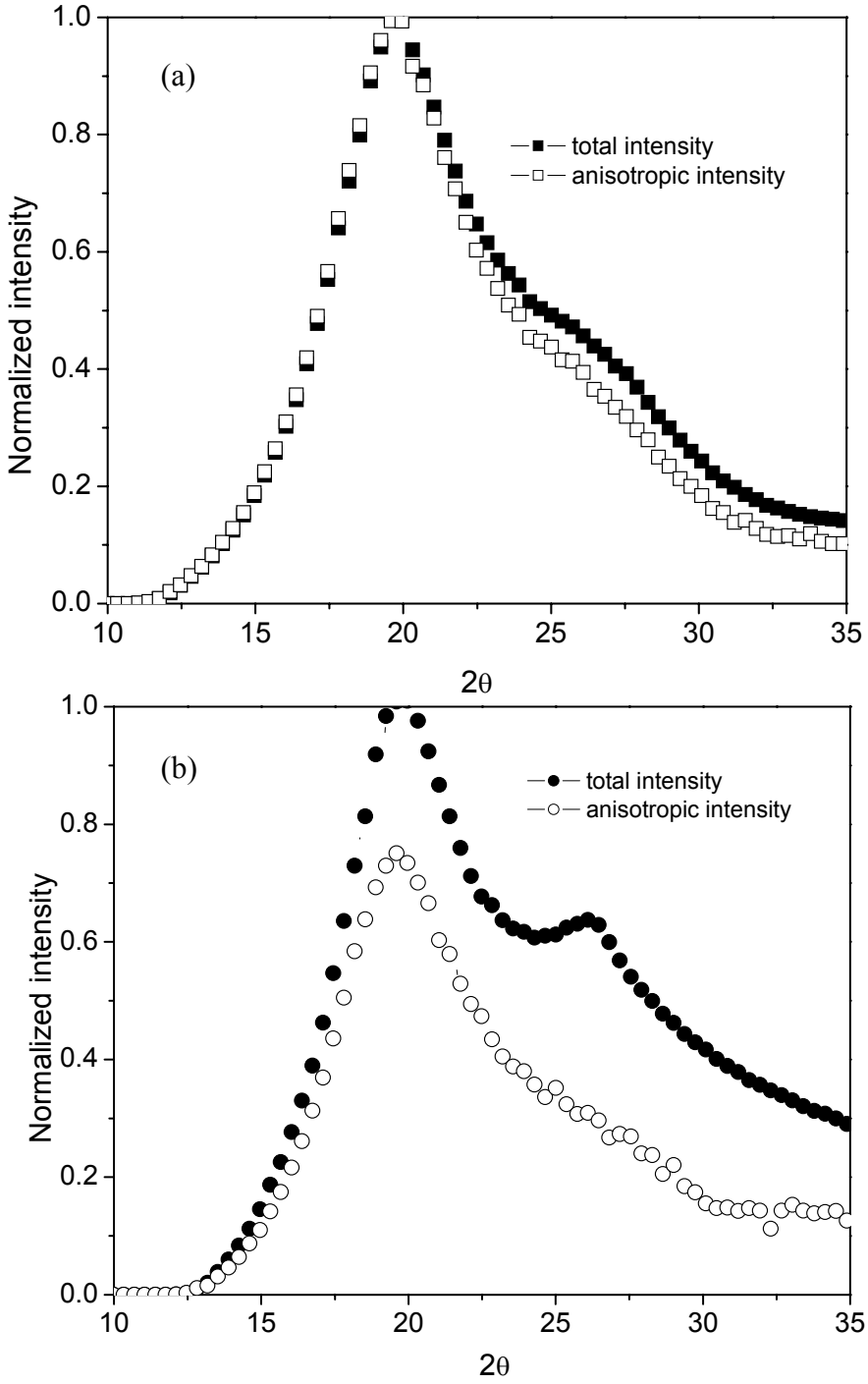

Figure 4.9. Radial (2θ) intensity profiles of extrudates for: (a) pure TLCP, (b) 5 wt% MJ composites.

The reduction of TLCP orientation is likely a consequence of surface anchoring of the nematic phase on the nanofiber surface. It has been reported that the molecular orientation of TLCP in TLCP/fiber composites was anchored by the carbon and glass fiber surfaces [Bhama and Stupp, 1990; Lee et al., 1994]. Furthermore, this observation is consistent with that reported in an earlier study [Cho et al., 2003], where it was shown that the incorporation of carbon nanotubes in discotic liquid crystalline pitch precursor disrupted the severe radial orientation of the disc-like molecules and produced a more random orientation in the plane. Therefore, it is hypothesized that, for a given set of processing conditions, the microstructure of TLCP can be rendered less anisotropic due to the surface anchoring afforded by inclusions such as carbon nanofibers.

To further generalize these observations, WAXD analyses were performed for other combinations of carbon nanofibers and TLCPs. V400P and A950, and their composites containing PR fibers, were extruded using a single screw extruder. It is noted from Chapter 2 that PR fibers were straight as compared with curly MJ fibers. A circular die of 1 mm diameter (L/D=10) was used at an apparent shear rate of 500 s^{-1}. These shear rates were calculated from measured values of throughput and die diameter: $\dot{\gamma}_{wa} = 4Q/\pi R^3$. For V400P, the temperature profile was 170, 200, 250, and 250°C in the feed, two metering sections, and die, respectively. The temperature profile for A950 was 230, 260, 300, 300°C. Extrudates were not post-drawn, and their nominal diameter was ~0.8mm.

In Figure 4.10, individual 2D diffraction images of extrudates processed at 500 s^{-1} of shear rate are presented for pure V400P and its composites containing 1, 5, and 10

wt% PR nanofibers. For pure V400P and 1 wt% PR composite, the (110) plane formed an intense arc. In contrast, the same reflection produced broader arcs at 5 wt% PR composite that finally evolved to a uniform ring at a PR fiber content of 10 wt%. It is noted that the shorter and more intense is the arc length, the higher is the orientational order.

Next, Figure 4.11a displays integrated (2θ) intensity profiles of pure V400P and its PR composites. These profiles are similar to those observed for MJ fiber/V400P composites. The highest scattering intensity was observed at 2θ of ~19° in all cases. Further, at 2θ of 26-28° for pure V400P and 1 wt% composites, a shoulder appeared. In contrast, for 5 and 10 wt% composites, a distinguishable peak associated with graphene (002) planes from carbon nanofibers was observed. The azimuthal intensity profiles for (110) peak, presented in Figure 4.11b, showed that higher contents of nanofibers led to broader profiles.

Figure 12 displays individual 2D diffraction images of A950 and its composites containing PR fibers prepared at 500 s^{-1} of shear rate. For pure A950, two peaks were observed in integrated (2θ) intensity profiles (Figure 13a). At a 2θ of 27°, distinct peaks due to (211) planes appeared, whereas V400P showed only a shoulder. It is likely that comonomers added for synthesizing V400P weaken the degree of packing of polymer chains. It should be noted that the equatorial reflection is most intense for pure A950 samples than its composites. As observed in V400P and its composites, addition of PR fibers into A950 led to a reduction of the intensity of the equatorial peak and a uniform ring. These rings were more intense compared to V400P.

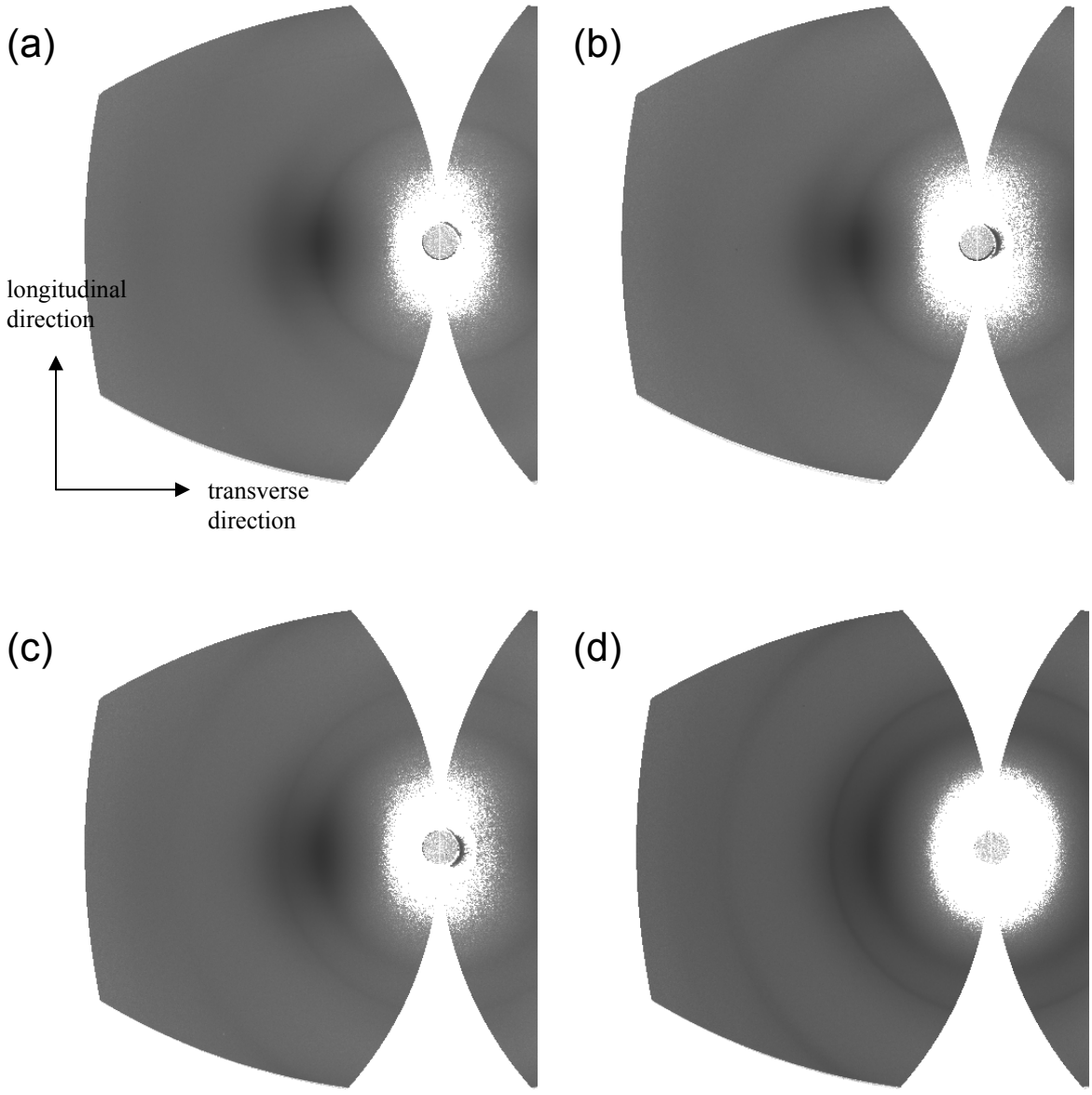

Figure 4.10. Wide angle x-ray diffraction patterns of the extrudates from: (a) pure V400P, (b) 1 wt%, (c) 5 wt%, and (d) 10 wt% PR composites.

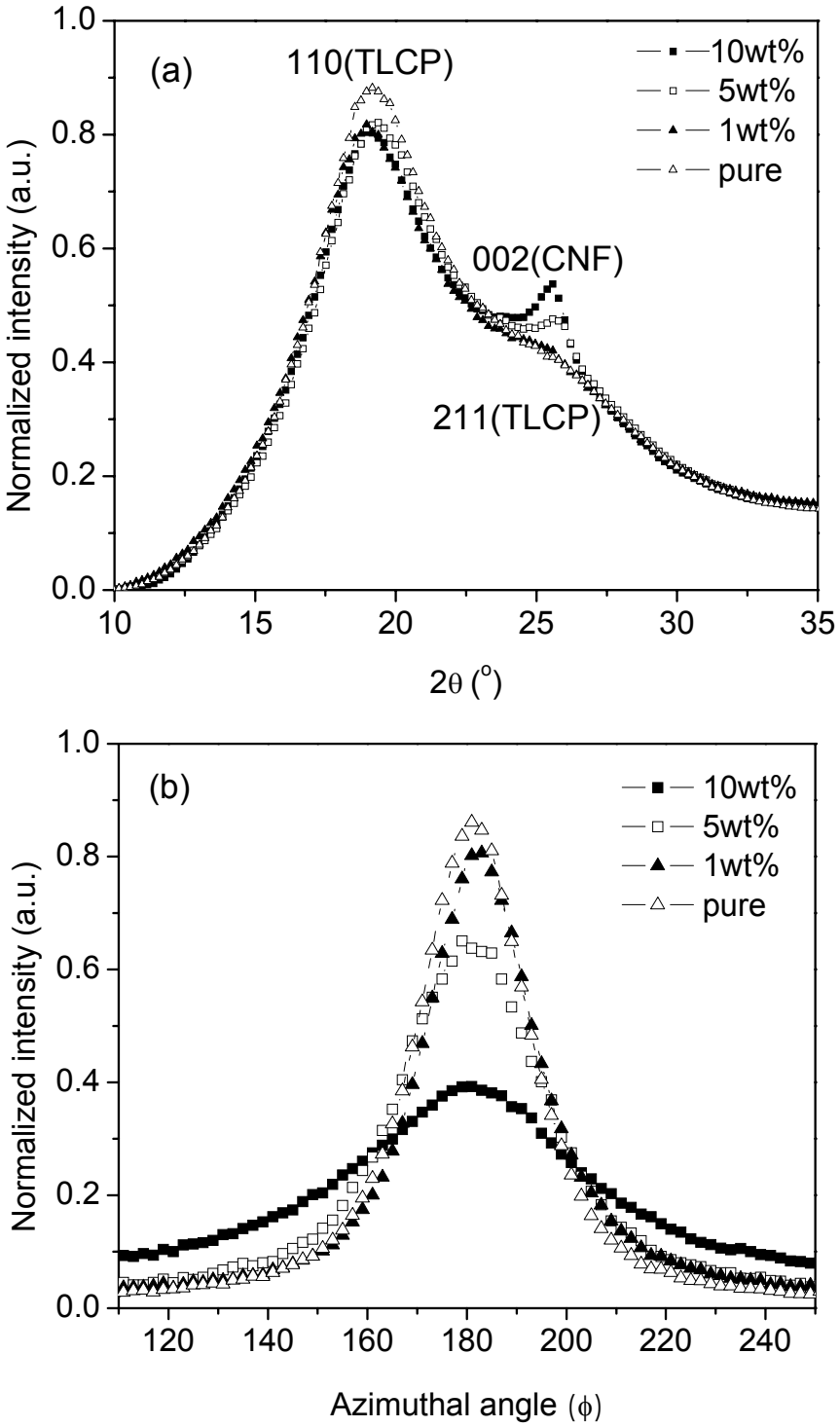

Figure 4.11. (a) Radial (2θ) intensity profiles and (b) azimuthal intensity profiles at 2θ ~ 19° of extrudates: pure V400P, 1 wt%, 5 wt%, and 10 wt% PR composites.

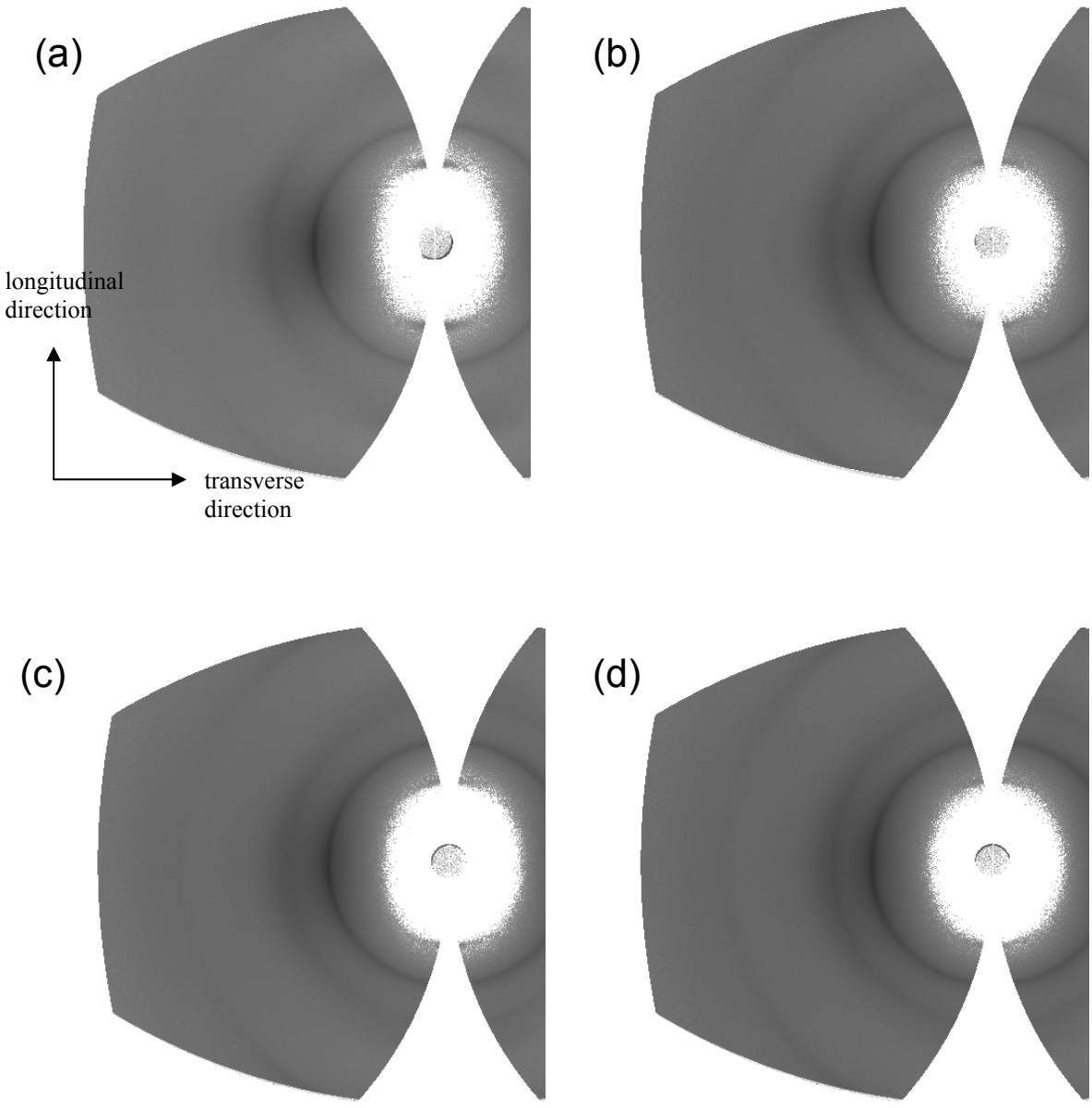

Figure 4.12. Wide angle x-ray diffraction patterns of extrudates: (a) pure A950, (b) 1 wt%, (c) 5 wt%, and (d) 10 wt% PR composites.

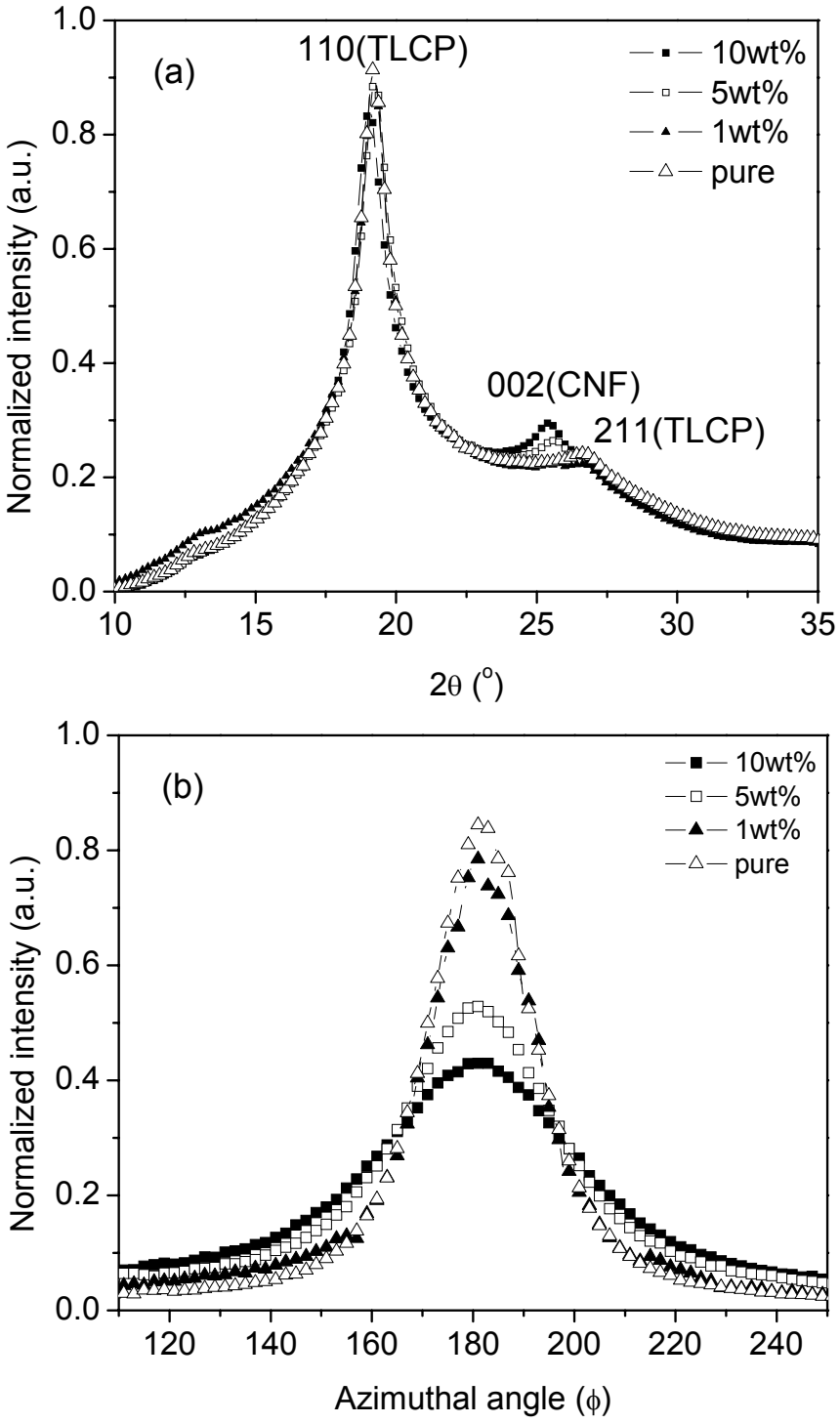

Figure 4.13. (a) Radial (2θ) intensity profiles and (b) azimuthal intensity profiles at 2θ ~ 19° of extrudates: pure A950, 1 wt%, 5 wt%, and 10 wt% PR composites.

For 5 and 10 wt% composites, an intense peak at a 2θ of 26°, associated with graphene (002) planes from CNFs, revealed the (211) peaks into a shoulder.

Using the equatorial (110) peak, Herman's orientation parameter (*f*) in the longitudinal direction was calculated for V400P, A950, and their composites containing PR fibers. From the *f* values, a significant difference between V400P and A950 composites was not observed. Further, compared to MJ fiber/V400P composites (Table 4.2), a smaller decrease of *f* values in PR fiber/V400P composites was observed at the same content of CNF, even though pure TLCPs showed a similar degree of orientation. This may result from the straight morphology of PR fibers, which are probably oriented more along a given flow direction, compared to MJ fibers. However, it should be noted that these results confirm that CNFs decrease molecular orientation of TLCPs.

Table 4.3. Herman's orientation parameter for V400P, A950, and their composites containing PR fibers

TLCP	pure	1wt%	5wt%	10wt%
V400P	0.86	0.84	0.80	0.74
A950	0.85	0.82	0.80	0.75

4.3.3 Microstructure

Figure 4.14a displays a cross section of a pure V400P sample cryo-fractured under liquid nitrogen at a low magnification (X100). It is interesting to note that the cross section was not circular, but was deformed. Various sheet-like structures appeared. It is likely that tensile force applied during testing, which can lead to a severe orientation in the longitudinal direction, led to these structures.

In higher magnification SEM micrographs, additional features were observed. Figure 4.14b displays a typical fibrillar structure. Further, tape-like structure was observed in Figure 4.14c. These are layered sheets made by aligned bundle of fibrils. In Figure 4.14d, fibrils, having a diameter of 2-5μm became tapered at the end, indicating necking resulting from tensile forces.

Sawyer et al. have described the microstructure of TLCPs, which were copolyester TLCPs composed of 2,6-naphthyly and 1,4-phenyl units [Sawyer et al., 1987]. They observed a fibrillar structure in the longitudinal direction. Fibrillar structure was described as a structure that is fiber-like with high aspect ratio, but does not possess fiber symmetry. Further, they observed tape-like structures, which are uniaxially oriented sheets. According to the hierarchical model [Sawyer et al., 1987], TLCPs possess bundles of macro fibrils (5 μm), fibrils (0.5 μm), and micro fibrils (0.05 μm), in decreasing order of their size. SEM micrographs of pure TLCP samples from present study also revealed macro fibrils. Sawyer et al. reported that these fibrillar structures and the length of fibrils observed with fractured surface correlated with the strength of the material.

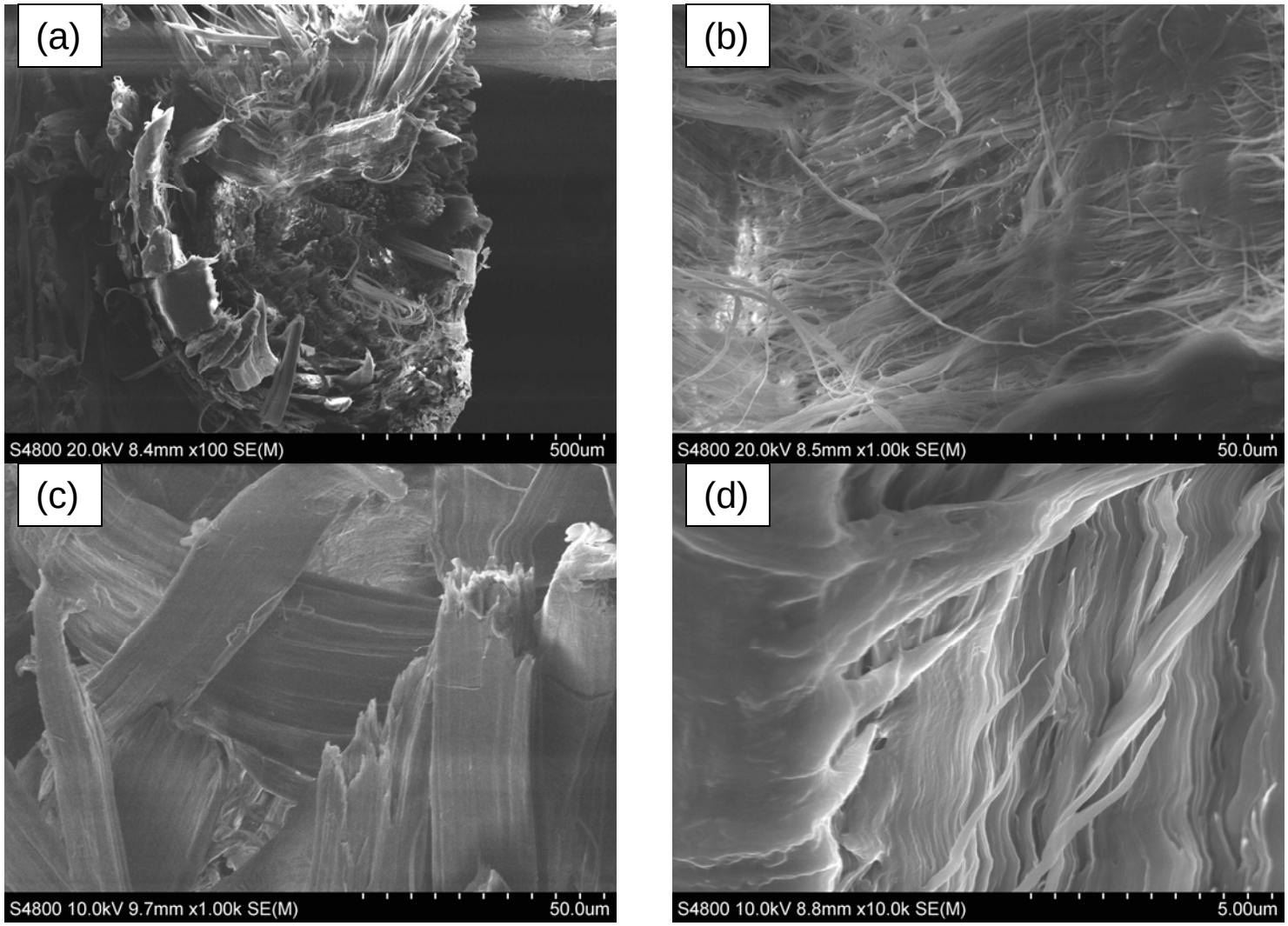

Figure 4.14. SEM micrographs of pure V400P at various magnifications: (a) 100, (b) 1K, (c) 1K, and (d) 10K

Figures 4.15a-d display cross-sections of composites containing 10 wt% of PR fibers. Samples were prepared by cryo-fracturing in liquid nitrogen. From Figure 4.15a, it is evident that the cross-section is circular and intact, as compared to that for pure V400P. Further, fibrillar and tape-like structures, which were observed for pure V400P, did not appear to any appreciable extent (Figures 4.15a and b). Therefore, it is inferred that the highly oriented structure along longitudinal direction, one of TLCP characteristics, was modified in the presence of PR fibers. However, in higher magnification micrographs of composites (Figure 4.15c and d), micro fibrils (0.05 μm) of V400P were observed even though their aspect ratio was not high. PR fibers were distinguished by uniform diameter and hollow core, whereas V400P fibrils were tapered at the end. It is evident that PR fibers pulled out from V400P matrix even though the other side of PR fibers was wetted by the V400P matrix.

These morphological changes confirm the effect of CNFs in disrupting the severe orientation that can otherwise develop in TLCPs. From WAXD results, it was confirmed that CNFs led to a reduction of the degree of orientation of TLCPs. SEM micrographs further confirm that macro fibrillar structure of TLCPs was not significant in the presence of CNFs, even though micro-fibrillar structure existed.

To further verify these results, pure A950 and its composites containing 10 wt% of PR fibers were also examined and SEM micrographs are presented in Figures 4.16a-d and 4.17a-d. Pure A950 showed distinct macro size fibrils and tape-like structures, which were similar to those of pure V400P. These structures were longitudinally oriented.

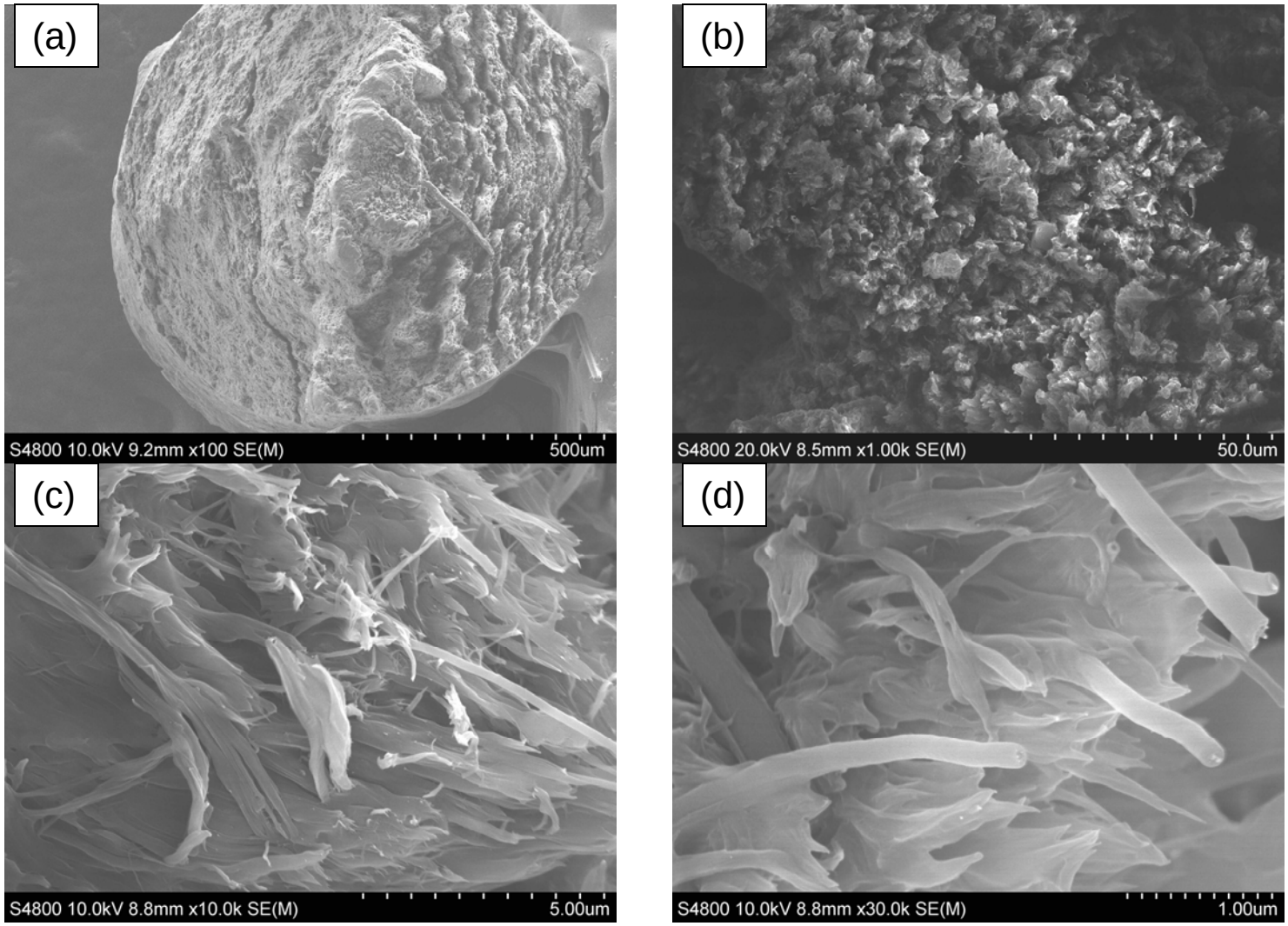

Figure 4.15. SEM micrographs of V400P/10 wt% PR fibers at various magnifications: (a) 100, (b) 1K, (c) 10K, and (d) 30K.

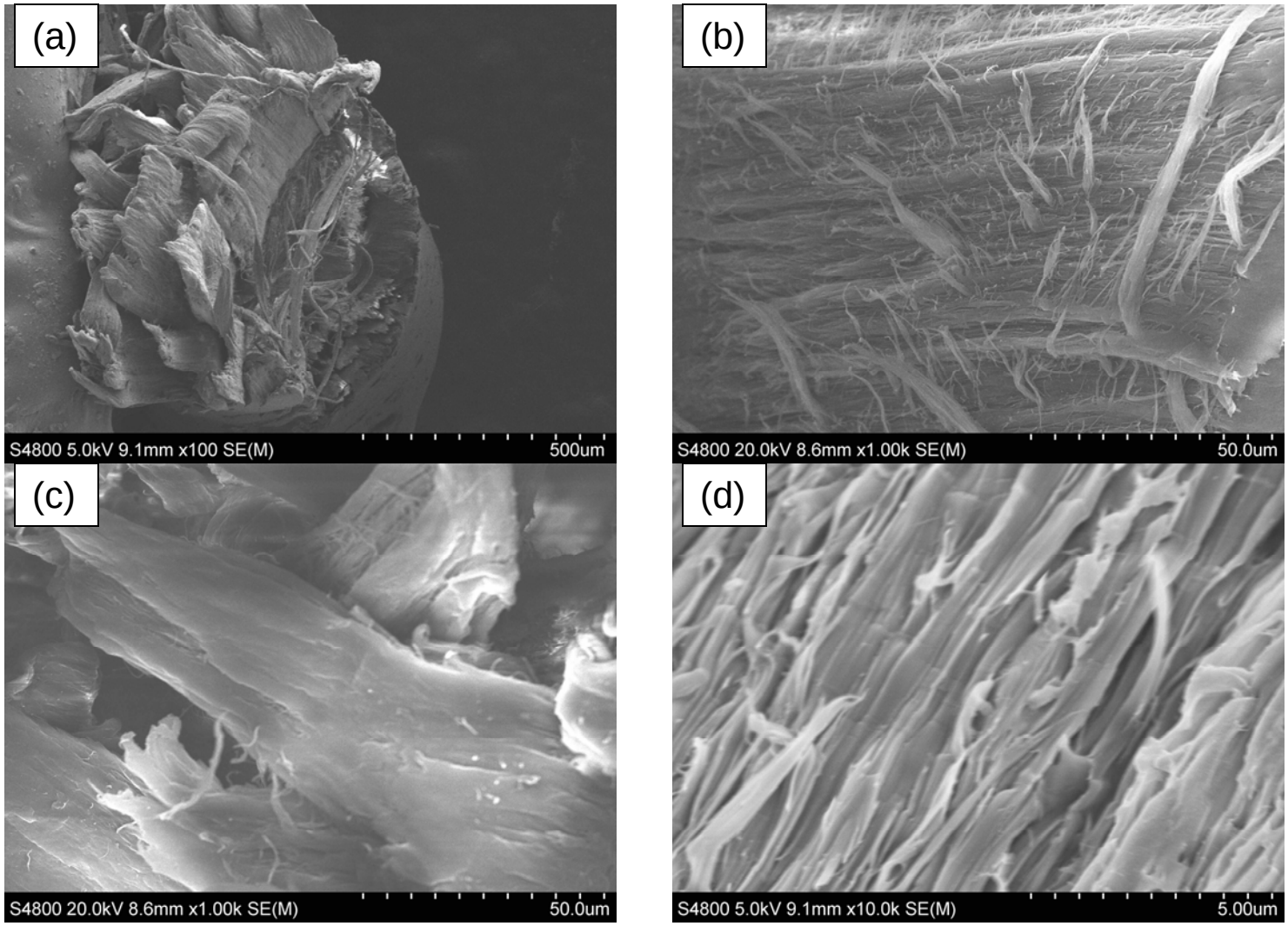

Figure 4.16. SEM micrographs of pure A950 at various magnifications: (a) 100, (b) 1K, (c) 1K, and (d) 10K.

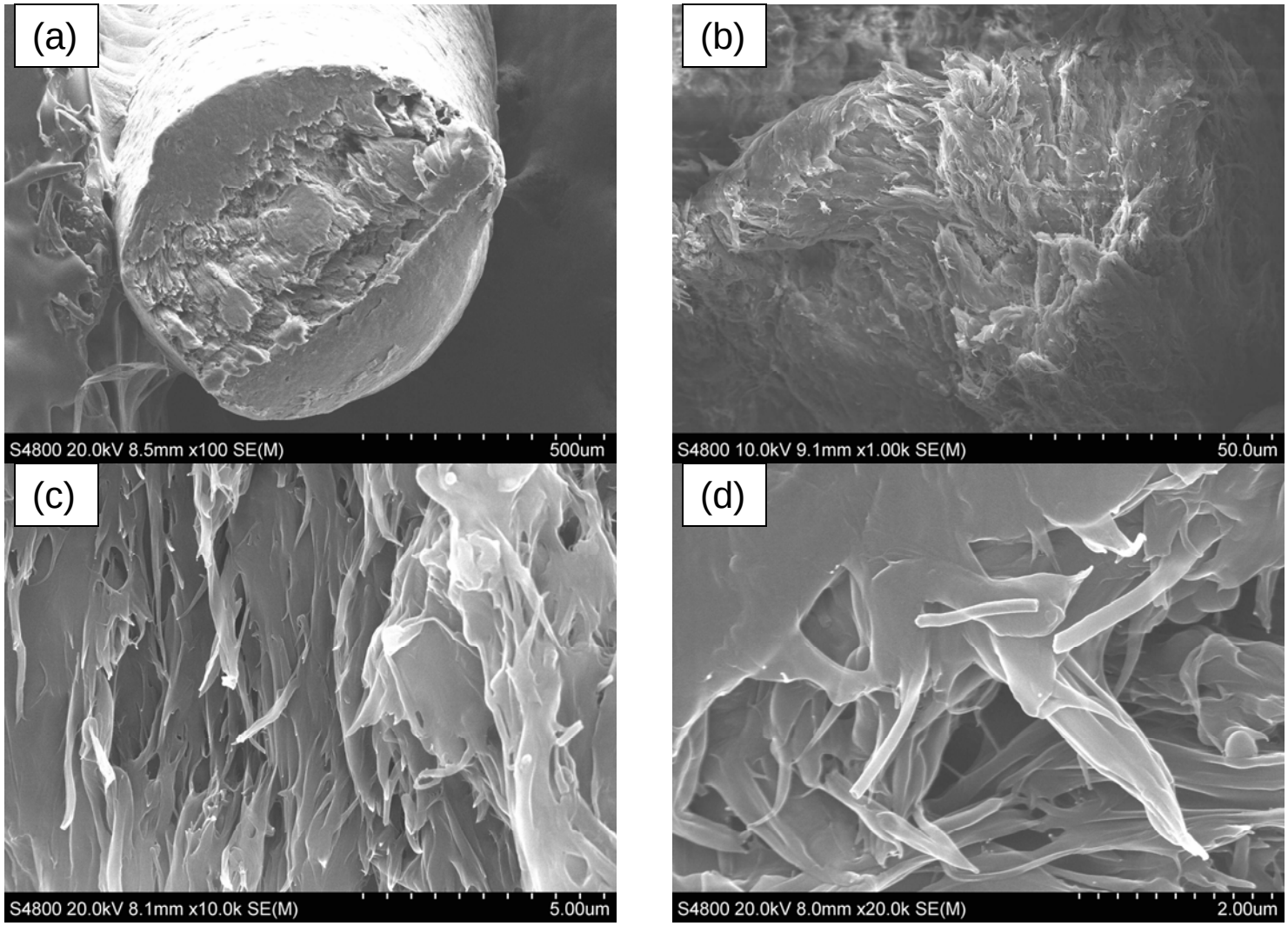

Figure 4.17. SEM micrographs of A950/10 wt% PR fibers at various magnifications: (a) 100, (b) 1K, (c) 10K, and (d) 20K.

In contrast, such highly oriented fibrillar and tape-like structures were not observed in composites.

For observing structure at higher magnification, transmission electron microscopy (TEM) analysis was performed. Extrudates of pure TLCPs and their 10 wt% PR composites were cryo-microtomed in the perpendicular direction using a diamond knife under liquid nitrogen. Figure 4.18a displays bright field images for pure V400P at low magnification. Contrast in bright field image of TEM results from thickness variation. Bright and dark sections indicate thin and thick regions, respectively. These are artifacts of cutting (white lines), which also resulted in folding of layers (black lines) perpendicular to longitudinal direction, as illustrated by the arrow on the micrographs in Figure 4.18a.

It should be noted that at higher magnification, micrographs were obtained from relatively homogeneous areas to avoid artifacts noted above. In Figure 4.18b, banded structures were observed even though they are small and weak. These are more significant in Figure 14.8c, and finally very fine wavy structures appeared in Figure 14.8d.

The fibrillar hierarchy described above has been reported in prior literature studies [Sawyer and Jaffe 1986; Sawyer et al., 1993]. Microstructure of TLCPs has also been studied using other techniques such as scanning tunneling microscopy (STM) [Sawyer et al., 1993] and TEM [Donald and Windle, 1983; Donald et al., 1983; Sawyer and Jaffe 1986; Sawyer et al., 1993; Taylor et al., 2003; Chan and Gao, 2005].

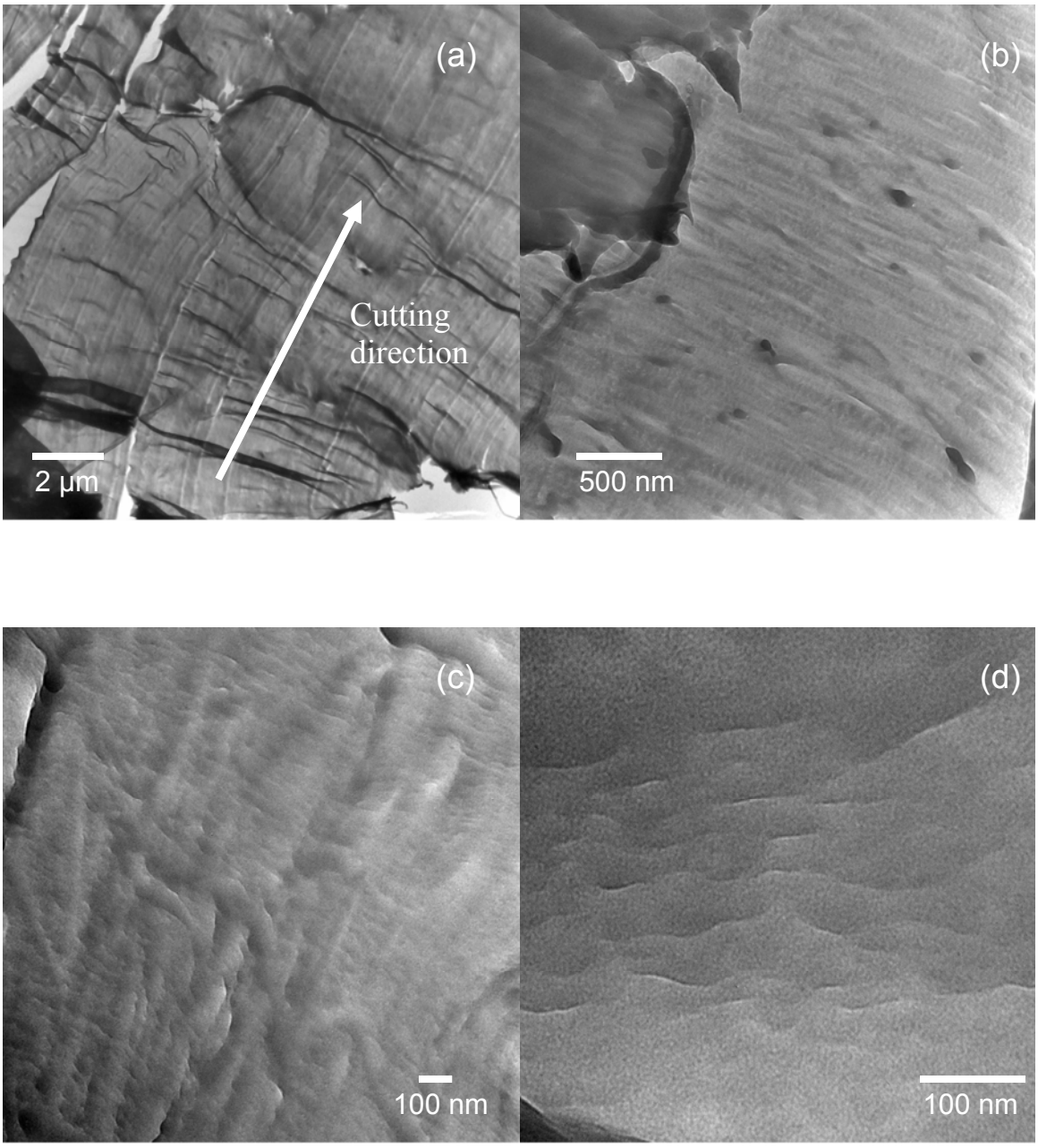

Figure 4.18. TEM micrographs of V400P at various magnifications: (a) 15K, (b) 50K, (c) 100K, and (d) 300K.

From TEM micrographs, the most interesting feature of TLCPs observed was the banded structure which is associated with a serpentine path or "meander of the molecules" at a periodicity of 500 nm [Donald and Windle, 1983]. Donald and Windle observed bands of alternating diffracting (bright) and non-diffracting (dark) regions. Further, these bands were normal to the shear direction. In contrast, bright field imaging did not show clear banded structures. Banded structures of Vectra grade TLCPs have also been reported by other scientists [Sawyer and Jaffe 1986; Sawyer et al., 1993; Taylor et al., 2003; Chan and Gao, 2005]. Sawyer and Jaffe observed the periodicity of the microbands with a size of 100 nm from as-spun fibrils by TEM [Sawyer and Jaffe 1986]. Figure 4.18d indicates that these microbands were observed in the present results as a wavy path of molecules. Width of the dark bands was 10~50 nm, which is relatively smaller than those from literature studies.

Sawyer and coworkers confirmed periodic microbanded structures by STM, which is capable of imaging down to 1 nm. Further, three-dimensional images of Vectran fibers by STM revealed that microfibrils possessed tape-like structure with width of 10~50 nm and thickness of 2~10 nm rather than a round fibrous structure [Sawyer et al., 1993]. Using these observations, an expanded hierarchical fibrillar structure model with more detailed microfibril sizes, shapes and order was suggested [Sawyer et al., 1993]. Because the TEM micrographs reported here are two-dimensional, information about thickness of microstructure can not be obtained from Figure 14.8d. However, width of dark bands (10~50 nm) is consistent with results from STM micrographs by Sawyer and coworkers [Sawyer et al., 1993].

TEM micrographs of composites containing 10 wt% PR fiber content are shown in Figures 4.19a-d. Artifacts such as cutting lines and folding by microtoming appeared at a low magnification (Figure 4.19a), which were also observed for pure V400P. From Figures 4.19b and c, it was evident that PR fibers were fairly dispersed, but they are not oriented along one direction, indicating that the flow field applied for sample preparation is not strong enough to align discontinuous PR fibers in V400P matrix. This may disrupt the anisotropy of V400Ps. In Figure 4.19c, several microbands were observed. However, Figure 4.19d suggests that microbands were not significantly observed in the vicinity of PR fibers, indicating a disruption of periodicity of banded structures.

Samples for pure A950 and its composites containing 10 wt% PR fibers were also investigated, and TEM micrographs are presented in Figures 4.20a-d and 4.21a-d, respectively. There was not a significant difference in the micrographs for pure V400P and pure A950 (Figures 4.20a-d). The width of banded structures was observed in the range of 20-50nm (Figure 4.20d). Further, TEM micrographs of A950 composites revealed the disruption of banded structures of TLCPs by PR fibers (Figure 4.21c), while banded structures were observed in the area devoid of PR fibers (Figure 4.21d). These results confirm the disrupting effect of CNFs on microstructure of TLCPs, which was also observed for V400P composites.

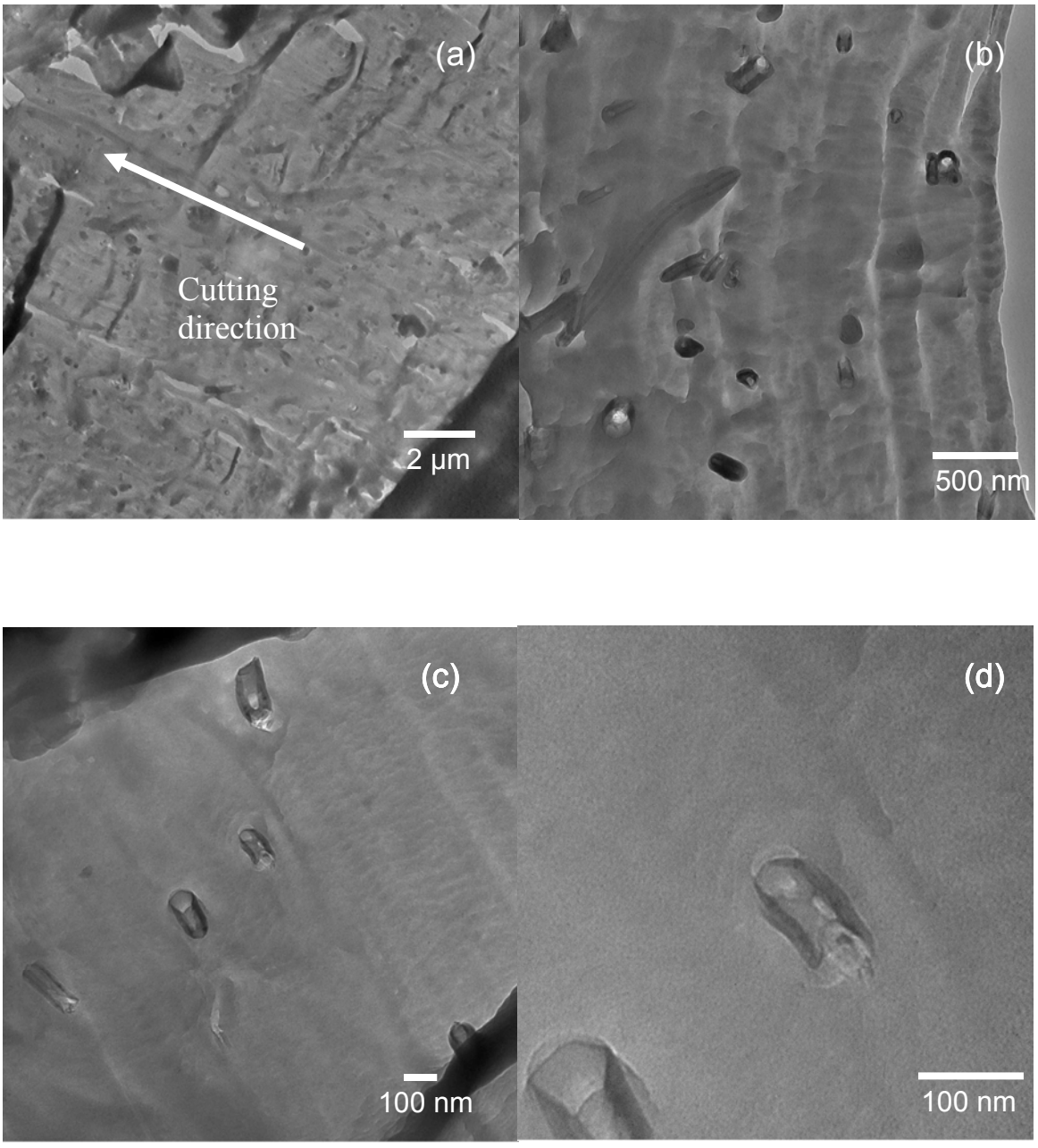

Figure 4.19. TEM micrographs of V400P/10 wt% PR fibers at various magnifications: (a) 10K, (b) 50K, (c) 100K, and (d) 300K.

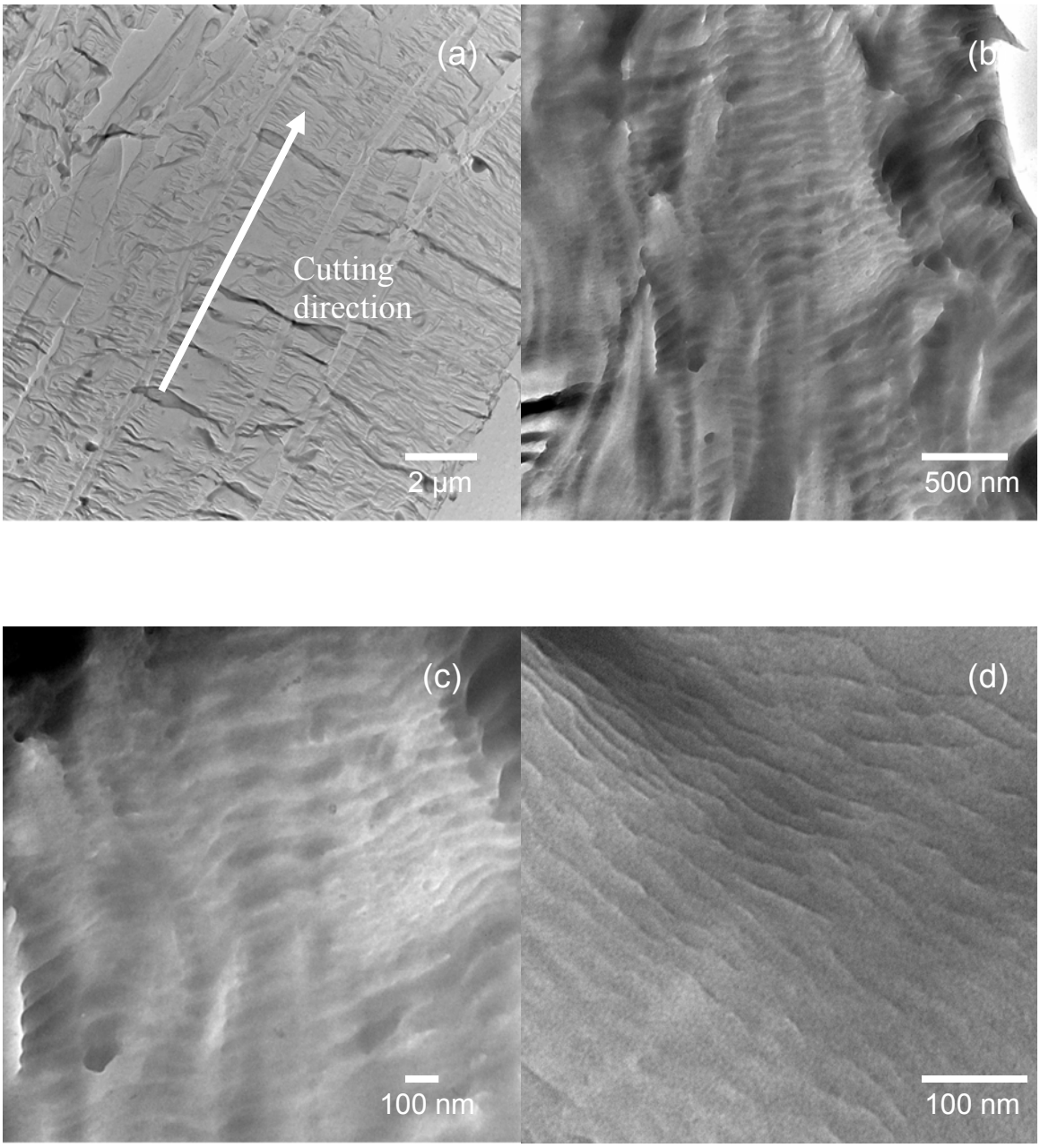

Figure 4.20. TEM micrographs of A950 at various magnifications: (a) 10K, (b) 50K, (c) 100K, and (d) 300K.

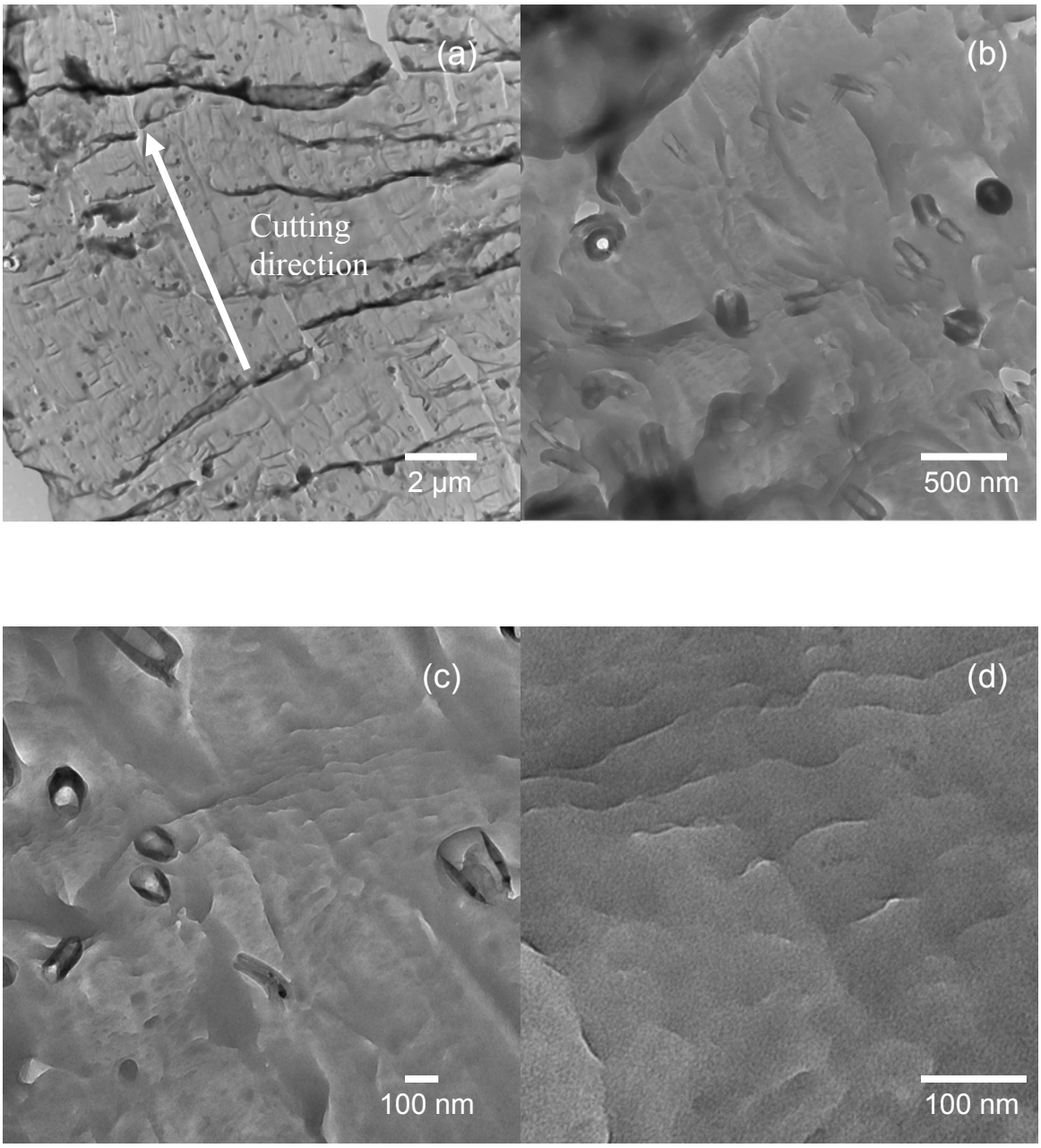

Figure 4.21. TEM micrographs of A950/10 wt% PR fibers at various magnifications: (a) 10K, (b) 50K, (c) 100K, and (d) 300K.

4.4. Conclusions

The incorporation of MJ fibers in a thermotropic liquid crystalline polymer (V400P) improved the electrical conductivity of the resulting nanocomposite. The electrical percolation threshold was observed in the V400P composite at approximately 5 wt% MJ fiber. A decrease in tensile modulus from 70 GPa for a pure V400P to 38 GPa for 5 wt% MJ composites was observed. Also, tensile strength decreased from 420 MPa for pure V400P to 200 MPa for 5 wt% MJ composites. The preferred orientation of V400P molecules was studied by WAXD and, as expected, was found to be higher for samples processed in strong flows. However, the V400P molecular orientation distribution broadened with increasing MJ fiber content. WAXD studies showed a decrease of Herman's orientation parameter from 0.85 for pure TLCP to 0.71 for 5 wt% MJ composites. These phenomena were also confirmed for other grades of CNF (PR fiber) and TLCP (A950).

The disruption of molecular orientation of TLCPs was inferred by SEM and TEM analysis. SEM micrographs revealed a fibrillar structure for pure TLCPs at a macro-scale (2-5 μm). However, this structure was not observed in composites at the same scale even though micro-size fibrils (0.05 μm) were found with the addition of PR fibers. TEM micrographs displayed banded structures of pure TLCPs, but these structures were not significant in the vicinity of PR fibers. These results indicate that PR fibers can help to reduce the severe anisotropy that is otherwise observed for TLCPs. In summary, the nanofiber solid surface constrains the nematic phase, a phenomenon also referred to as

“surface anchoring”, and helps reduce the severely high degree of molecular order in the TLCP matrix, and reduces anisotropy in the nanocomposite.

CHAPTER 5

CONCLUSIONS AND RECOMMENDATIONS

The objective of this research was to investigate the effect of nano-modifiers such as carbon nanofibers (CNFs) on crystalline and orientational structure of linear low density polyethylene and thermotropic liquid crystalline polymers processed by extrusion. This chapter summarizes results obtained from Chapters 2, 3, and 4. Finally, recommendations for future work are provided at the end of the chapter.

5.1 Conclusions

First, the microstructure of two different grades of CNFs, MJ (experimental) and PR (commercial), was investigated as a function of different thermal treatments. From Raman spectroscopy and XRD analysis, an enhancement of crystallite size was observed after heat treatment at 2200°C. The crystallite thickness increased from 1.6±0.1 nm to 10.9±0.5 nm for MJ fibers and from 3.1±0.3 nm to 11.7±0.4 nm for PR fibers; width increased from 1.0±0.2 nm to 3.1±0.5 nm for MJ fibers and from 1.7±0.7 nm to 8.0±0.7 nm for PR fibers, confirming an increase of crystalline size. Also, an increase in thermal oxidation stability for heat-treated CNFs was observed. BET adsorption isotherms showed a significant reduction of specific surface area of MJ fibers (300 m^2/g) after the heat treatment (51 m^2/g) and also after the CVD surface treatment (30 m^2/g), resulting from a decrease of pore volume (from 0.525 cm^3/g for MJ to 0.146 cm^3/g and 0.098 cm^3/g for MJCVD and MJHT, respectively). However, even after heat treatment, MJ

fibers possessed a rougher surface than did PR fibers. It is concluded that these surface and structural changes in CNFs are controlled by heat treatment, which can play an important role in the nanocomposite.

In Chapter 3, these CNFs were incorporated into linear low density polyethylene (LLDPE) using intensive mixing. It was observed that electrical volume resistivity of composites decreased with the addition of CNFs ($>1\times10^{12}$, 8.9×10^{3}, and 4.2×10^{3} ohm-cm for pure LLDPE, 15 wt% MJ, and 35 wt% PR composites, respectively). Tensile modulus increased from 110 MPa for pure LLDPE to 200 MPa and 300 MPa for 15 wt% MJ and 15 wt% PR composites, respectively. However, the tensile strength remained fairly unchanged at about 20 MPa. Strain-to-failure decreased from 690% for pure LLDPE to 460% and 120% for 15 wt% MJ and 15 wt% PR composites, respectively. It was inferred that the interfacial bonding of LLDPE matrix with MJ fibers is better than that with PR fibers, resulting from the rougher surface of MJ fibers.

Crystallization behavior of LLDPE nanocomposites is reported in the presence of three types of CNFs (MJ, PR and PRCVD). WAXD results indicate the orthorhombic crystal structure of LLDPE from (110), (200), and (020) planes. Overall crystallinity of LLDPE (approximately 35%), calculated using WAXD diffractograms, did not change significantly in any of the LLDPE/CNF nanocomposites. Non-isothermal DSC analysis of nanocomposites indicated that 15 wt% PRCVD composites exhibited three melting peaks at 107.6°C, 119.2°C, and 122.1°C, similar to those for pure LLDPE. However, one of the three melting peaks for LLDPE disappeared in the presence of MJ fibers. Further, the observation that the broad melting peak becomes more intense with increasing MJ

fibers content suggests that MJ fibers lead to thinner LLDPE lamellae. TEM micrographs of nanocomposites revealed transcrystalline growth of LLDPE on CNF surface, and a slightly broader distribution of lamellar thickness. It is concluded that a larger specific surface area of MJ fibers relative to that of PR fibers (BET studies of Chapter 2) and the rougher surface of MJ fibers contribute toward the different crystallization behavior of the nanocomposites.

In Chapter 4, the incorporation of MJ fibers in a thermotropic liquid crystalline polymer (TLCP) improved the electrical conductivity of the resulting nanocomposite. The electrical percolation threshold was observed in the V400P composite at approximately 5 wt% MJ fiber. A decrease of tensile modulus from 70 GPa for a pure V400P to 38 GPa for 5 wt% MJ composites was observed. Also, tensile strength decreased from 420 MPa for pure V400P to 200 MPa for 5 wt% MJ composites. The preferred orientation of V400P molecules was measured by WAXD and, as expected, was found to be higher for samples processed in strong flows. However, the V400P molecular orientation distribution broadened with increasing MJ fiber content. WAXD studies showed a decrease in Herman's orientation parameter from 0.85 for pure V400P to 0.71 for 5 wt% MJ composites. These phenomena were also confirmed for other grades of CNF (PR fiber) and TLCP (A950).

The disruption of molecular orientation of TLCPs was inferred by SEM and TEM analysis. SEM micrographs revealed a fibrillar structure for pure TLCPs at a macro-scale (2-5 μm). However, this structure was not observed in composites at the same scale even though micro-size fibrils (0.05 μm) were found with the addition of PR fibers. TEM

micrographs displayed banded structures of pure TLCPs, but these structures were not significant in the vicinity of PR fibers. These results indicate that PR fibers can help to reduce the severe anisotropy that is otherwise observed for TLCPs. It is concluded that the nanofiber solid surface constrains the nematic phase, a phenomenon also referred to as "surface anchoring", and helps reduce the severely high degree of molecular order in the TLCP matrix, and reduces anisotropy in the nanocomposite. In summary, surface and structural changes in CNFs are important for ultimately controlling the electrical, mechanical properties, and microstructure of nanocomposites because graphitic content and structure play an important role in the nanocomposite.

5.2 Recommendations for Future Work

The following are the proposed recommendations for future research based on the current study:

In Chapter 2, the change of surface structure of CNFs resulted from heat treatment due to a decrease of pore volume and reorganization of graphitic structure. It was concluded that surface structure of CNFs plays an important role for composite properties. In Chapter 3, the dependence of mechanical properties on surface structure of CNFs with a different origin was observed. However, heat treated CNFs were not incorporated into polymer. For future work, polymer composites containing CNFs heat treated to ultrahigh temperatures should be prepared and their effect on interfacial bonding and resulting mechanical properties should be studied.

As discussed in Chapter 3, shorter mixing times (2-6 min) resulted in lower percolation threshold and higher electrical conductivity, but also resulted in poorer spatial homogeneity of the nanocomposite. Consequently, 20 min of mixing time was used for this study. Intensive mixing used in this study results in breaking CNFs, and this effect becomes severe with a longer mixing time although more uniformly dispersed CNFs can be obtained. Therefore, a study on mixing variables such as mixing time and mixing temperature is necessary to study the degree of dispersion and breakage of CNFs. Also, that study can be directed toward maximizing the effect of CNFs on enhancing electrical properties of composites.

In Chapter 4, WAXD diffractograms provided overall orientation of composites, which decreased significantly in the presence of CNFs. Orientation obtained from XRD is an average value for the extrudates (due to the beam size of 0.5 mm diameter). However, to understand how CNFs work for reducing the severe anisotropy of TLCPs, an interfacial region between CNFs and TLCPs should be investigated. Selected area electron diffraction (SAED) can focus on a small area around 2 μm in diameter, allowing for investigating the microstructure of TLCP in the vicinity of CNFs. Therefore, SAED introduced in Chapter 2 to observe structure of CNFs could be extended to polymer composites.

The influence of nano-modifiers on TLCPs should be studied in biaxial flow system. In the present study, we considered only uniaxial flow process such as extrusion and fiber spinning, which can induce a highly oriented molecular orientation of TLCPs. However, in the case of TLCP films that experience biaxial flow, the incorporation of

CNF can lead to less severe orientation and more balanced in-plane properties of TLCPs. This may help TLCP films overcome imbalanced mechanical properties, resulting from the anisotropic nature of TLCPs.

One of the interesting characteristics of TLCPs is that in a steady state flow, they display a "three-region" flow curve. Regions I and III (at a low and high shear rate, respectively) are referred to as shear thinning in which the viscosity decreases with increasing shear rate. In intermediate plateau region II, the viscosity is independent of shear rate. Shear thinning behavior at a low shear rate, region I, has been observed only in LCPs, whereas regions II and III are common for flexible polymers. This rheological phenomenon has been explained by a process of continuous textural evolution of LCPs with increasing shear rate. Therefore, a study of the rheological behavior of TLCP/CNF composites can also provide the evolution of microstructure of TLCPs and a systematic understanding of the influence of CNF on this microstructural evolution of TLCPs.

The evolution of microstructure of pure V400P and its composites during fiber spinning should be investigated thoroughly by on-line characterization system available in the Center for Advanced Engineering Fibers and Films (CAEFF). Fiber spinning involves an extensional uniaxial flow during the draw-down step, in addition to the shear flow studied for extrudates in Chapter 4. Evolution of diameter, velocity, temperature profiles, and orientational structure of pure V400P and its composites needs to be investigated thoroughly.

Results of microstructure evolution from on-line characterization study are of value in validating modeling results obtained from simulation work on complex flows

incorporating Rey's constitutive equations. Simulation coding can be developed by collaborative interaction with the modeling group in the Center for Advanced Engineering Fibers and Films (CAEFF).

APPENDICES

APPENDIX A

The Detailed Experimental Procedure

A1. Tensile Testing

Tensile properties such as tensile modulus, tensile strength, and strain-at-break to evaluate mechanical performance of pure polymers and their composites were measured using an ATS universal tensile tester 900 at 25°C. For calculating tensile modulus, tensilestrength, and stain at break, using following equations.

$$\varepsilon = \frac{\Delta L}{L} \tag{1}$$

$$E = \frac{\sigma}{\varepsilon} \tag{2}$$

$$\sigma = \frac{F}{A} \tag{3}$$

where ε , ΔL, L, E, σ, F, and A are a strain, a displacement, an initial length of sample, tensile modulus, tensile strength, force, and a cross sectional area of sample, respectively. However, the measured displacement is not only from the elongation of a sample but also from the elongation of system such as a loading and a griping. Therefore, compliance test can help for removing the system elongation. The measured displacement is described by a following equation.

$$\Delta L_m = \Delta L + \Delta L_s \tag{4}$$

where ΔL_m, ΔL_s, and ΔL are the measured displacement, the system displacement, and the sample displacement. Further, if a compliance ($C = \Delta L/F$) is introduced, the equation (4) can be modified with a following equation.

$$C_m = C + C_s \tag{5}$$

where C_m, C_s, and C are the measured compliance, the system compliance, and the sample compliance, respectively. Equation (5) can be described with modulus as a following

$$C_m = C + C_s = \mathrm{C} + \frac{\Delta L \cdot A}{F \cdot L}\frac{L}{A} = \mathrm{C} + \frac{1}{E}\frac{L}{A} \tag{6}$$

From the equation (6), a slope and an intercept correspond an inverse modulus and the system compliance in plot C_m vs. L/A. Therefore, the modulus from only sample can be obtained without a system influence. For this compliance test, the tensile test should be conducted with at least three different gauge lengths. Figure A.1 can be referred for the following procedure.

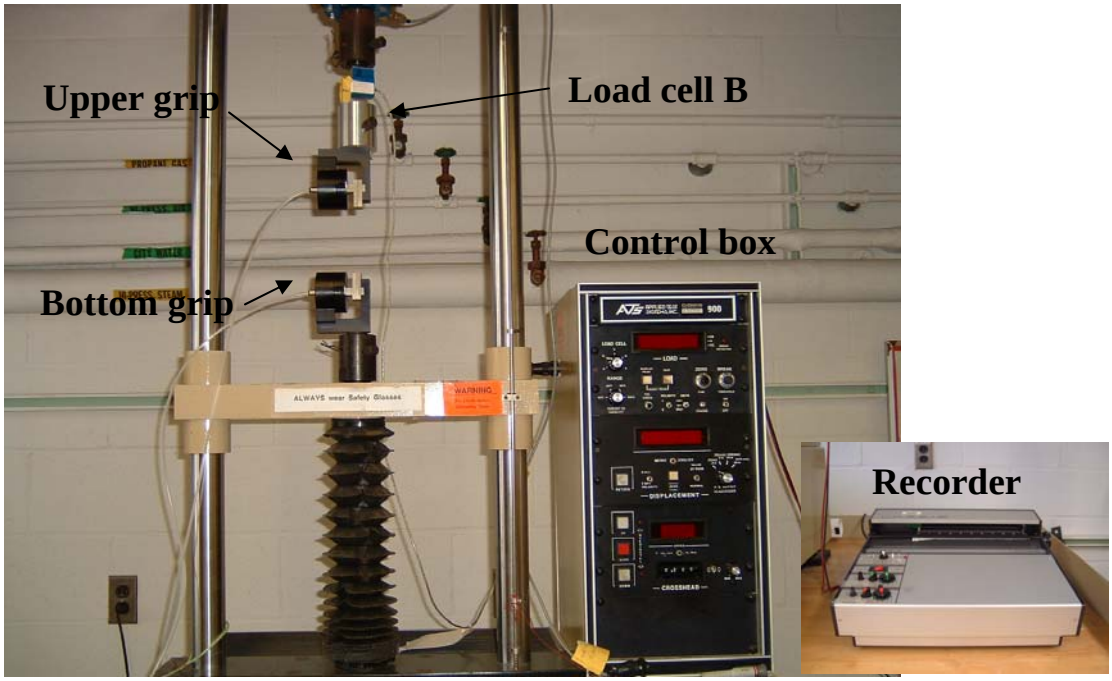

Figure A.1. A photograph of the ATS universal tensile tester 900.

A2. Static Charge Decay

The pure polymers and their composites were characterized for their ability to dissipate an induced surface charge within a specified time. The test method was based on the Federal Test Method 101C, Method 4046, and military specification Mil-B-81705B that require this time frame to be less than 2 seconds to dissipate 99 percent of the induced charge. A static decay meter (Model 406D, Electro-Tech Systems, Inc) was used to measure the static decay time. Figure A.2 can be referred for following this procedure.

1. Press the “POWER” button and set “HIGH VOLTAGE” off.

2. Allow 15 min for warm-up.

3. Place STM-1 test module in sample holder electrodes

4. Insert white banana plug into jack on chassis.

5. Cage cover is down and select “+ HIGH VOLTAGE”.

6. Rotate “HIGH VOLTAGE ADJUST” for “+5KV” on “CHARGING VOLTAGE” meter.

7. Select “MANUAL” mode and “10% CUTOFF”.

8. “SAMPLE CHARGE” meter was set to "0" by adjusting “ZERO” control.

9. Press “CHG” button and adjust “FULL SCALE” control (STM-1 position) for setting “+5KV” reading on “SAMPLE CHARGE” meter.

10. Press “ZERO/STBY” button and recheck "0" setting.

11. Press “CHG” button. When “SAMPLE CHARGE” meter reads “+5KV”, press “TEST” button. Decay time should equal time on STM-1±0.05 sec.

12. Repeat steps 8-11 for -5KV. Measured decay time should be within 0.2sec of time measured at +5KV

13. Select desired “CUTOFF” and press “CHG” button.

14. Check “SAMPLE CHARGE” meter read "0".

15. Place a 3" X 5" aluminum foil in test cage electrodes.

16. Select “+5KV” and adjust “FULL SCALE” control (“NORM” position) for “+5KV” reading on “SAMPLE CHARGE” meter.

17. Do not readjust this control when testing samples.

18. Remove foil and place test sample in sample holder electrodes.

19. Press “ZERO/STBY” button and adjust “ZERO” setting.

20. Press “CHG” button. When “SAMPLE CHARGE” meter reads full scale, press “TEST” button.

21. Record measures decay time displayed on the screen.

22. Repeat steps 14-21 for “-5KV”.

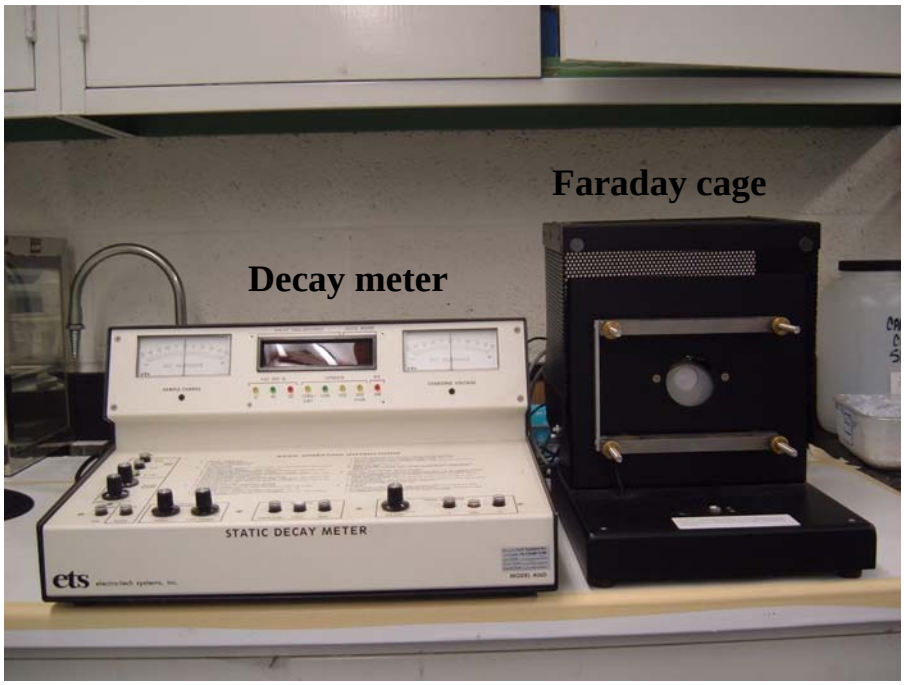

Figure A.2. A photograph of the static decay meter.

A3. Surface resistivity

Surface resistivity was measured according to EOS/EDS-S11.11 using ACL 800 Megaohmeter (ACL Staticide, USA). Surface resistivity is not a basic material property

even though volume resistivity is a material property. With an assumption that material is thin and homogeneous, surface resistivity converts into volume resistivity using following equation

$$\sigma_S = \sigma_V \cdot t$$

where σ_s, σ_v, and t are surface resistivity, volume resistivity, and sample thickness.

To distinguish surface resistivity from a simple resistivity, ohms/square is used for the unit of surface resistivity. Figure A.3 can be referred for following this procedure.

1. Surface of testing sample should be clean and free of contaminants before testing
2. Place the Megaohmmeter on the sample surface.
3. Select desired voltage either 10 or 100 volts using switch in the unit.
4. Press and hold the test button with 5 lbf for ~15 sec.
5. Record surface resistivity (ohm/in^2) on the screen.

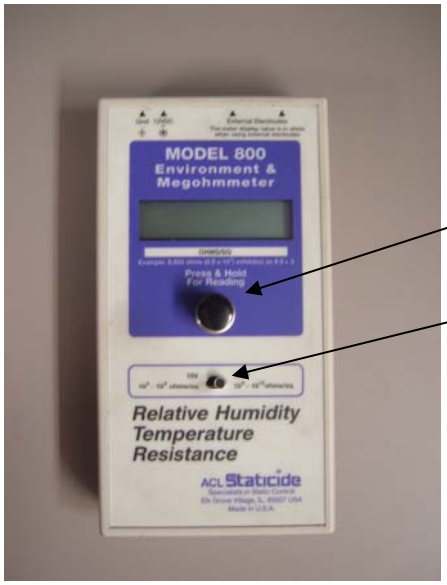

Test button

Switch for voltage selection

Figure A.3. A photograph of the Megaohmmeter.

A.4 Scanning Electron Microscopy

Morphology of carbon nanofibers, polymers, and their composites was observed using Scanning Electron microscope (Hitachi FE S-4300, Japan).

1. Stick a double-stick carbon tape on an aluminum stub and place samples on the surface of the carbon tape.
2. Mark beside of samples to distinguish between the different samples on one stub.
3. Use the Hummer® 6.2 Sputtering system in the Electron Microscope Facility for coating pure polymers or their composites with platinum.
4. Before coating, check if the main power is off, voltage is zero and gas switch is off.
5. Place the stub in the chamber.
6. Turn on the main power and check if the chamber is on the right position.
7. Allow the vacuum to reach ~40 millitorr.
8. Turn on the gas switch, and open the valve until the gas (argon) pressure in the chamber reaches 200 millitorr.
9. Close the valve to decrease the pressure to 70 millitorr. Then, switch on the voltage and increase it till the current is 15 mA.
10. Put the timer switch in auto, and rotate a knob to 1.5 to coat the samples for 1.5 mins.
11. When the power is automatically turned off after 1.5 mins, remove the stub, and turn off the main power. Ensure if the main power is off, voltage is zero and gas switch is off.
12. Load the stub with the sample on the SEM sample holder.
13. Adjust the height, and check the height of the holder with no-go gauge. It must be less than 12cm.
14. Press the open button in SEM chamber and open the chamber.

15. Place and tighten a sample holder to the arm, and pull back the arm.

16. Close the chamber and press the close button.

17. Open the gate after vacuuming the chamber, and move the arm directly beneath the electron beam.

18. Close the gate. The arm can be computer controlled.

19. Set the appropriate working distance, level of detector, and accelerating voltage (e.g. 10cm, upper detector, 5 KV and 10 μA).

20. Focus on the sample for the desired magnifications and save the micrographs.

A.5 Transmission Electron Microscopy

Graphitic structure of carbon nanofibers, morphology and lamellar structure of polymers, and their composites was observed using Transmission Electron microscope (Hitachi H-7600, Japan). Figure A.5 can be referred for following this procedure.

1. For Acc voltage on (the left hand side monitor), click “40 kV” → “Set” → “HV on”, then wait for 5min. Follow these steps for each voltage (60, 80, 100, and 120 kV). When 120 kV was reached, move to "Filament on"

2. Click on “Filament on” (the left hand side panel)

3. Select HR1 for a high resolution (max = 600K X) (on the left hand side monitor)

4. Put 5 for spot number (spot size = 5 μm) and click “Set” (on the left hand side monitor)

5. Reset “LENS” on the left hand side panel

6. Press “ZOOM1” button in “LENS MODE” on the left hand side panel

7. Rotate “BRIGHT” knob to check beam alignment on the left hand side panel

8. Condenser lens alignment
   Make beam be ciurclar using two adjustment knobs on both panels.
   Press “BH” button on the right hand side panel. Make beam be ciurclar

using two adjustment knobs on both panels

9. Z axis alignment
   Put a magnification of 10K. On the right hand side panel, press “WOB” on “MODULE” to make beam move around. Adjust a knob under the sample holder tube to have a stable beam. Press “MODU” on “MODULE” to make beam sputter with a magnification of 30K. Make beam be stabe using two adjustment knobs on both panels.

10. Put a magnification of 200K and focus on a copper grid.

11. Select “FFT” on the right hand side monitor and “FFT” window will pop up.

12. Make beam be circular using two adjustment knobs on both panels.

13. Back to “Survey” on the right hand side monitor.

14. Make sure that “BH” should be “ON” on the right hand side panel.

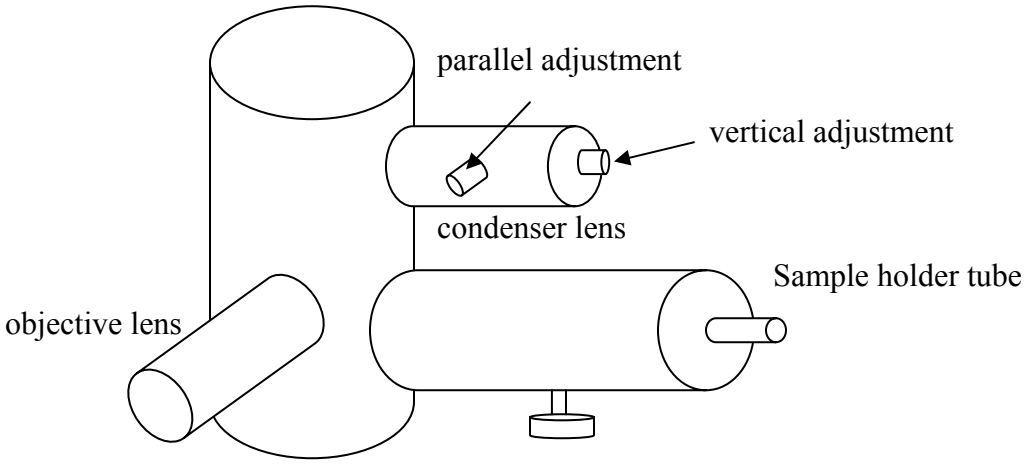

Figure A.4. A schematic of TEM.

LITERATURE CITED

Aggarwall SL, Tilley GP. Determination of crystallinity in polyethylene by X-ray diffractometer. J Polym Sci 1955; 18: 17-26.

Applied Science Inc. http://www.apsci.com/asi-research.html as viewed 19 October 2007.

Avella M, Dell'Erba R, Martuscelli E. Fiber reinforced polypropylene: Influence of iPP molecular weight on morphology, crystallization, and thermal and mechanical properties. Polymer Composites. 1996; 17: 288-99.

Baker RTK, Barber MA, Harris PS, Feates FS, Waite RJ. Nucleation and growth of carbon deposits from the nickel catalyzed decomposition of acetylene. J Catal 1972; 26: 51-62.

Beach DL, Kissin YV. Dual functional catalysis for ethylene polymerization to branched polyethylene. I. Evaluation of catalytic systems. J Polym Sci 1984; 22: 3027-42.

Belin T, Epron F. Characterization methods of carbon nanotubes: a review. Mater Sci Eng B 2005; 119: 105-18.

Bhama S, Stupp SI. Liquid crystal polymer-carbon fiber composites. Molecular orientation. Polym Eng Sci 1990; 30: 228-34.

Bhattacharyya AR, Sreekumar TV, Liu T, Kumar S, Ericson LM, Hauge RH, Smalley RE. Crystallization and orientation studies in polypropylene/single wall carbon nanotube composite. Polymer 2003; 44: 2373-77.

Blythe AR. Electrical properties of polymers. Cambridge University Press, 1979, Cambridge.

Brandl W. Marginean G, Chirila V, Warschewski W. Production and characterization of vapour grown carbon fiber/polypropylene composites Carbon 2004; 42: 5-9.

Buckley and Edie, Cabon-carbon materials and composites. NASA Reference Publication 1254, 1992.

Butzbach GD, Wendorff JH, Zimmermann HJ. Structure and structure formation of a main chain thermotropic polymer. Polymer 1986; 27: 1337-1344.

Chai GS, Yoon SB, Yu JS. Highly efficient anode electrode materials for direct methanol fuel cell prepared with ordered and disordered arrays of carbon nanofibers. Carbon 2005; 43: 3028-31.

Chan CK, Gao P. Shear-induced interactions in blends of HMMPE containing a small amount of thermotropic copolyester HBA/HQ/SA. Polymer 2005; 46: 10890-6.

Cherukupalli SS, Ogale AA. Online measurements of crystallinity using Raman spectroscopy during blown film extrusion of a linear low-density polyethylene. Polym Eng Sci 2004; 44: 1484-90.

Chiou JS, Paul DR. Gas transport in a thermotropic liquid crystalline polyester. J Polym Sci A Polym Phys 1987; 25: 1699-707.

Chivers RA, Moore DR. Influence of fiber reinforcement on the mechanical anisotropy of liquid crystal polymer. Polymer 1991; 32: 2190-8.

Cho T, Lee YS, Rao R, Rao AM, Edie DD, Ogale AA. Structure of carbon fiber obtained from nanotube-reinforced mesophase pitch. Carbon 2003; 41: 1419-24.

Choi YK, Sugimoto K, Song SM, Gotoh Y, Ohkoshi Y, Endo M. Mechanical and physical properties of epoxy composites reinforced by vapor grown carbon nanofibers. Carbon 2005; 43: 2199-208.

Chung TS. Thermotropic liquid crystal polymers: Thin-film polymerization, characterization, blends, and applications; Technomic Publishing Company Inc.: Lancaster, 2001.

Defoor F, Groeninckx G, Schouterden P, Van der Heijden B. Molecular, thermal and morphological characterization of narrowly branched factions of 1-octene LLDPE: 2. Study of the lamellar morphology by transmission electron microscopy. Polymer 1992; 33: 5186-90.

Donald AM, Windle AH. Electron microscopy of banded structures in oriented thermotropic polymers. J Mater Sci 1983; 18: 1143-50.

Donald AM, Viney C, Windle AH. Banded structures in oriented thermotropic polymers. Polymer 1983; 24: 155-9.

Donald AM, Windle AH. Liquid Crystalline Polymers; Cambridge University press: Cambridge, 1992.

Donohue MD, Aranovich GL. Classification of Gibbs adsorption isotherms, Advances in Colloid and Interface Science 1998: 76-77: 137-152.

Endo M, Kim YA, Hayashi T, Yanagisawa T, Muramatsu H, Ezaka M, Terrones H, Terrones M, Dresselhaus MS. Microstructural changes induced in “stacked cup” carbon nanofibers by heat treatment. Carbon 2003; 41: 1941-7.

Feller JF, Linossier I, Grohens Y. Conductive polymer composites: comparative study of poly(ester)-short carbon fibres and poly(epoxy)-short carbon fibres mechanical and electrical properties. Mater Lett 2002; 57: 64-71.

Feng J, Li J, Chan CM. Distribution of carbon black in semicrystalline polypropylene studied by transmission electron microscopy. J Appl Polym Sci 2001; 85: 358-65.

Feng L, Kamal MR. Crystallization and melting behavior of homogeneous and heterogeneous linear low-density polyethylene resins. Polym Eng Sci 2005; 45: 1140-51.

Finegan IC, Tibbetts GG. Electrical conductivity of vapor-grown carbon fiber/thermoplastic composites. J Mater Res 2001; 16: 1668-74.

Finegan IC, Tibbetts GG, Glasgow DG, Ting JM, Lake ML. Surface treatments for improving the mechanical properties of carbon nanofiber/thermoplastic composites. J Mater Sci 2003; 38: 3485-90.

Flodberg G, Hedenqvist MS, Gedde UW. Barrier properties of injection molded blends of liquid crystalline polyester (Vectra) and high density polyethylene. Polym Eng Sci 2003; 43: 1044-57.

Freidel G. The mesomorphic states of matter. Ann Phys (Paris) 1922; 18: 273-473.

Gregg SJ, Sing KSW. Adsorption, Surface Area, and Porosity, Academic Press Inc.: New York, 1967, Chap. 2.

Guillemo AJ, Jana SC. Electrically conductive polymer nanocomposites of polymethylmetacrylate and carbon nanofibers prepared by chaotic mixing. Composites Part A 2006; 38: 983-93.

Guo T, Harrison GM, Ogale AA. Transient shear rheology and rheo-optical microstructural characterization of a thermotropic liquid crystalline polymer. Polym Eng Sci 2005; 45: 187-97.

Gupta AK, Rana SK, Deopura BL. Crystallization kinetics of high-density polyethylene/linear low-density polyethylene blend. J Appl Polym Sci 1994; 51: 231-9.

Hammel E, Tang X, Trampert M, Schmitt T, Mauthner K, Eder A, Potschke P. Carbon nanofibers for composite applications. Carbon 2004; 42: 1153-8.

Han H, Bhowmik PK. Wholly aromatic liquid-crystalline polyesters. Prog Polym Sci 1997; 22: 1431-1502.

Han L, Kim TK, Kim YJ, Hahm HS, Kim MS. Hydrogen production by catalytic decomposition of methane over carbon nanofibers. Mater Sci Forum 2006; 510: 30-3.

Handlos AA, Baird DG. Extrusion blow molding of microcomposites based on thermotropic liquid crystalline polymers and polypropylene. Polym Eng Sci 1996; 36: 378-86.

He P, Gao Y, Lian J, Wang L, Quia D, Zhao J, Wang W, Schulz MJ, Zhou XP, Shi D. Surface modification and ultrasonication effect on the mechanical properties of carbon nanofiber/polycarbonate composites. Composites Part A 2005; 37: 1270-5.

Helveg S, Lopez-Cartes C, Sehested J, Hansen PL, Clausen BC, Rostrup-Nielsen, JR, Abild-Pedersen F, Norskov JK. Atomic-scale imaging of carbon nanofibre growth. Nature 2004; 427: 426-9.

Heremans J. Electrical conductivity of vapor-grown carbon fibers. Carbon 1985; 23: 431-6.

Hine P, Broome V, Ward I. The incorporation of carbon nanofibres to enhance the properties of self reinforced, single polymer composites. Polymer 2005; 46: 10936-44.

Howe JY, Tibbetts GG, Kwang C, Lake ML. Heat treating carbon nanofibers for optimal composite performance. J Mater Res 2006; 21: 2646-52.

Huang Y, Young RJ. Interfacial micromechanics in thermoplastic and thermosetting matrix carbon fibre composites. Composites Part A 1996; 27: 973-80.

Hughes TV, Chambers CR. Manufacture of carbon filaments. US patent 405480, 1889.

Hwang JY, Lee SH, Sim KS, Kim JW. Synthesis and hydrogen storage of carbon nanofibers. Synth Metals 2002; 126: 81-5.

Ijima S. Helical microtubes of graphitic carbon. Nature 1999; 354: 56-8.

Jacobsen RL, Tritt TM, Guth JR, Ehrlich AC, Gillespie DJ. Mechanical properties of vapor-grown carbon fiber. Carbon 1995; 33: 1217-21.

Janimak JJ, Stevens GC. Structure correlated properties of metallocene catalysed polyethylenes by modulated temperature differential scanning calorimetry. Thermochimica Acta 1999; 332: 125-42.

Jawhari T, Roid A, Casado, J. Raman spectroscopic characterization of some commercially available carbon black materials. Carbon 1995; 33: 1561-5.

Jou WS, Wu TL, Chiu SK, Cheng WH. The influence of fiber orientation on electromagnetic shielding in liquid crystal polymers. J Electron Mater 2001; 31: 178-84.

Kaito A, Kyotani M, Nakayama K. Effect of annealing on the structure formation in a thermotropic liquid crystalline copolyester. Macromolecules 1990; 23: 1035-40.

Kaito A, Kyotani M, Nakayama K. Orientation profiles in the strand of thermotropic liquid crystalline polymer studied by polarized Fourier Transform Infrared Microspectroscopy. Macromolecules 1991; 24: 3244-9.

Kelker H, Hatz R. Handbook of liquid crystals, Verlag Chemie, Berlin, Germany, 1980.

Keller N, Maksimova NI, Roddatis VV, Schur M, Mestl G, Butenko YV, Kuznetsov VL, Schlogl R. The catalytic use of onion-like carbon materials for styrene synthesis by oxidative dehydrogenation of ethylbenzene. Angew Chem Int Ed 2002; 41: 1885-8.

Kim SU, Lee KH. Carbon nanofiber composites for the electrodes of electrochemical capacitors. Chem Phys Lett 2004; 400: 253-7.

King JA, Morrison FA, Keith JM, Miller MG, Smith RC, Cruz M, Neuhalfen AM, Barton RL. Electrical conductivity and rheology of carbon-filled liquid crystal polymer composites. J Appl Polym Sci 2006; 101: 2680-8.

Knight DS, White WB. Characterization of diamond film by Raman spectroscopy. J Mater Res 1989; 4: 385-93.

Kumar S, Doshi H, Srinivasarao M, Park JO, Schiraldi DA. Fibers from polypropylene/nano carbon fiber composites. Polymer 2002; 43: 1701-3.

Kuriger RJ, Alam MK, Anderson DP. Strength prediction of partially aligned discontinuous fiber-reinforced composites. J Mater Rev 2001; 16: 226-32.

Kuriger RJ, Alam MK, Anderson DP, Jacobsen RL. Processing and characterization of aligned vapor grown carbon fiber reinforced polypropylene. Composites Part A 2002; 33: 53-62.

Lakshminarayanan PV, Toghiani H, Pittman Jr CU. Nitric acid oxidation of vapor grown carbon nanofibers. Carbon 2004; 42: 2433-42.

Langelaan HC, Posthuma de Boer A. Crystallization of thermotropic liquid crystalline HBA/HNA copolymers. Polymer 1996; 37: 5667-79

Le Brizoual L, Belmahi M, Chatei H, Assouar MB, Bougdira J. Transmission electron microscopy study of carbon nanostructures grown by MPACVD in CH_4/CO_2 gas mixture. Diamond Relat Mater 2007; 16: 1244-9.

Lee WG, Hsu TC, Su AC. Interphase morphology of liquid crystalline polymer/glass fiber composites: Effect of fiber surface treatment. Macromolecules 1994; 27: 6551-8.

Lee BO, Woo WJ, Kim MS. EMI shielding effectiveness of carbon nanofiber filled poly(vinyl alcohol) coating materials. Macromol Mater Eng 2001; 286: 114-8.

Lee S, Kim MS, Ogale AA. Proc. Microstructure and tensile properties of thermotropic liquid crystalline polymer based films. Polymer Processing Society PPS-20 2004, Akron.

Lee S, Kim MS, Naskar AK, Ogale AA. Effect of carbon nanofibers on the anisotropy of an aromatic thermotropic liquid crystalline polymer. Polymer 2005; 46: 2663-7.

Lee S, Kim MS, Ogale AA. Influence of carbon nanofiber microstructure on electrical properties of LLDPE-based nanocomposites. ANTEC proccedings 2006; 486-90.

Lee S, Kim TR, Ogale AA, Kim MS. Surface and structure modification of carbon nanofibers. Synthetic Metals 2007a; 157: 644-50.

Lee S, Ogale AA, Kim MS. Crystallization behavior of carbon nanofiber/linear low density polyethylene nanocomposites. J Appl Polym Sci 2007b; 106: 2605-14.

Lehmann O. Zeits Phys Chem (Leipzig) 1890; 5: 427-435.

Li SN, Li ZM, Yang MB, Hu ZQ, Xu XB, Huang R. Carbon nanotubes induced nonisothermal crystallization of ethylene–vinyl acetate copolymer. Mater Lett 2004; 58: 3967-70.

Li P, Zhao TJ, Zhou JH, Sui ZJ, Dai YC, Yuan WK. Characterization of carbon nanofiber composites synthesized by shaping process. Carbon 2005; 43: 2701-10.

Lim JS, Lee SY, Park SM, Kim MS. Preparation of carbon nanofibers by catalytic CVD and their purification. Carbon Science 2005; 6: 31-40.

Lin CT, Chen WC, Yen MY, Wang LS, Lee CY, Chin TS, Chiu HT. Cone-stacked carbon nanofibers with cone angle increasing along longitudinal axis. Carbon 2007; 45: 411-5.

Linstid III HC, Cangiano DL, Demartino RN, Kuder JE, Provino VJ, Jester R. U.S. Patent 6 294 640, 2001.

Lopez Manchado MAL, Valentini L, Biagiotti J, Kenny JM. Thermal and mechanical properties of single-walled carbon nanotubes–polypropylene composites prepared by melt processing. Carbon 2005; 43: 1499-1505.

Lozano K, Barrera EV. Nanofiber-reinforced thermoplastic composites. I. Thermoanalytical and mechanical analyses. J Appl Polym Sci 2001; 79: 125-33.

Lozano K, Bonilla-Rios J, Barrera EV. A study on nanofiber-reinforced thermoplastic composites (II): Investigation of the mixing rheology and conduction properties. J Appl Polym Sci 2001; 80: 1162-72.

Lueking AD, Gutierrrez HR, Fonseca DA, Dickey E. Structural characterization of exfoliated graphite nanofibers. Carbon 2007; 45: 751-9.

Ma H, Zeng J, Realff ML, Kumar S, Schiraldi DA. Processing, structure, and properties of fibers from polyester/carbon nanofiber composites. Compos Sci Technol 2003; 63: 1617-28.

Marega C, Marigo A, Causin V. Small-angle X-ray scattering from polyethylene: Distorted lamellar stryctures. J Appl Polym Sci 2003; 90: 2400-7.

McNally T, Pötschke P, Halley P, Murphy M, Martin D, Bell SEJ, Brennan GP, Bein D, Lemoine P, Quinn JP. Polyethylene multiwalled carbon nanotube composites. Polymer 2005; 46: 8222-32.

Melanitis N, Tetlow PL, Galiotis C. Characterization of PAN-based carbon fibres with laser Raman spectroscopy. J Mater Sci 1996; 31: 851-60.

Mirabella FM, Bafna A. Determination of the crystallinity of polyethylene/α-olefin copolymers by thermal analysis: Relationship of the heat of fusion of 100% polyethylene crystal and the density. J Polym Sci Part B: Polym Phys 2002; 40: 1637-43.

Mironov VS, Park M, Choe C, Kim J, Lim S, Ko H. Influence of carbon fiber surface treatments on the structure and properties of conductive carbon fiber/polyethylene films. J Appl Polym Sci 2002; 84: 2040-8.

Muller AJ, Arnal ML, Spinelli AL, Carizales E, Puig CC, Wang H, Han CC. Morphology and crystallization kinetics of melt miscible polyolefin blends. Macromol Chem Phys 2003; 204: 1497-513.

Nielsen LE, Landel RF. Mechanical Properties of Polymers and Composites, 2nd ed 1994, Marcel Dekker, New York, NY.

Nikiel L, Jagodzinski PW. Raman spectroscopic characterization of graphites: A reevaluation of spectra/ structure correlation. Carbon 1993; 31: 1313-1317.

Qin Y, Zhang Z, Cui Z. Helical carbon nanofibers with a symmetric growth mode. Carbon 2004; 42: 1917-22.

Ono H, Oya A. Preparation of highly crystalline carbon nanofibers from pitch/polymer blend. Carbon 2006; 44: 682-6.

Orsini PG, Marchese B, Mazzarella L. Morphology of polyethylene single crystals. J Polym Sci Part A 1963; 1: 1901-8.

Quan H, Li ZM, Yang MB, Huang R. On transcrystallinity in semi-crystalline polymer composites. Compos Sci Tech 2005; 65: 999-1021.

Parados F. Plastic films-Situation and outlook: Rapra market report. Rapra Technology Limited, 2004, UK.

Park SH, Jo SM, Kim DY, Lee WS, Kim BC. Effects of iron catalyst on the formation of crystalline domain during carbonization of electrospun acrylic nanofiber. Synth Metals 2005; 150: 265-70.

Pierson HO. Handbook of Carbon, Graphite, Diamond and Fullerenes - Properties, Processing and Applications Chapter 3. William Andrew Publishing/Noyes, 1993.

Prasad A. A quantitative analysis of low density polyethylene and linear low density polyethylene blends by differential scanning calorimetery and fourier transform infrared spectroscopy methods. Polym Eng Sci 1998; 38: 1716-28.

Price RL, Waid MC, Haberstroh KM, Webster TJ. Selective bone cell adhesion on formulations containing carbon nanofibers. Biomaterials 2003; 24: 1877-87.

Probst O, Moore EM, Resasco DE, Grady BP. Nucleation of polyvinyl alcohol crystallization by single-walled carbon nanotubes. Polymer 2004; 45: 4437-43.

Puig CC, Aviles MV, Joskowicz P, Diaz A. On the melting behavior of isothermally crystallized 1-octene linear low-density polyethylene copolymers. J Appl Polym Sci 2001; 79: 2022-8.

Rabesiaka J, Kovacs AJ. Isothermal crystallization kinetics of polyethylene. III. Influence of the sample preparation. J Appl Phys 1961; 32: 2314-20.

Reinitzer F. Beitrage zur kenntniss des cholesterins. Monatsh Chemie 1888; 9: 421-441.

Rodriguez NM, Chambers A, Baker RTK. Catalytic engineering of carbon nanostructures. Langmuir 1995;11: 3862-6.

Rodriguez NM, Kim MS, Fortin F, Mochida I, Baker RTK. Carbon deposition on iron-nickel alloy particles. Appl Catal 1997; 148: 265-82.

Romo-Uribe A, Windle AH. Log-rolling alignment in main-chain thermotropic liquid crystalline polymer melts under shear: An in-situ WAXS study. Macromolecules 1996; 29: 6246-55.

Ros TG, van Dillen AJ, Geus JW, Koningsberger DC. Surface oxidation of carbon nanofibers. Chem Eur J 2002; 8: 1151-62.

Saengsuwan S, Mitchell GR, Bualek-Limcharoen S. Determination of orientation parameters in drawn films of thermotropic liquid crystalline polymer/polypropylene blends using WAXS. Polymer 2003; 44: 5951-9.

Sandler J, Windle AH, Werner P, Altstadt V, Es MV, Shaffer MSP. Carbon-nanofibre reinforced poly(ether ether ketone) fibres. J Mater Sci 2003; 38: 2135-41.

Sawyer LC, Jaffe M. The structure of thermotropic copolyester. J Mater Sci 1986; 21: 1897-913.

Sawyer LC, Chen RT, Jamieson MG, Musselman IH, Russell PE. The fibrillar hierarchy in liquid crystalline polymers. J Mater Sci 1993; 28: 225-38.

Sawyer LC, Grubb DT. Polymer Microscopy, 2nd ed.; Chapman & Hall: London, 1996.

Schmitt S. TEM analysis of microstructural morphology in ultra high molecular weight polyethylene. Scripta Materialia 2000; 43: 523-8.

Schouterden P, Groeninckx G, Van der Heijden B, Jansen F. Fractionation and thermal behaviour of linear low density polyethylene. Polymer 1987; 28: 2099-104.

Seo KS, in: Chung TS. (Eds.) Thermotropic liquid crystalline polymers. Technomic Publishing Co., Inc., 2001, Lancaster, PA, Chap. 8.

Shaikhutdinov ShK, Kinet Catal 1995; 36: 549–606.

Sperling LH. Introduction to Physical Polymer Science, 3rd ed.; John Wiley & Sons, Inc.: New York, 2001, Chap. 6.

Springer H, Hengse A, Hohne J, Schich A, Hinrichsen G. Investigation on crystallization and melting behaviour of linear low density polyethylene (LLDPE). Progr Coll Polym Sci 1986; 72: 101-5.

Sun Z, Cheng HM, Blackwell J. Structure of annealed copoly(p-hydroxybenzoic acid-2-hydroxy-6-naphthoic acid). 1. Chain conformation and packing. Macromolecules 1991; 24: 4162.

Taylor JE, Romo-Uribe A, Libera MR. Molecular orientation gradients in thermotropic liquid crystalline fiber. Polym Adv Technol 2003; 14: 595-600.

Tchoudakov R, Narkis M, Siegmann A. Electrical conductivity of polymer blends containing liquid crystalline polymer and carbon black. Polym Eng Sci 2004; 44: 528-40.

Tibbetts GG, Lake ML, Strong KL, Rice BP. A review of the fabrication and properties of vapor-grown carbon nanofiber/polymer composites. Comp Sci Tech 2007; 67: 1709-18.

Ticona, http://tools.ticona.com/tools/mcbasei as viewed 19 October 2007.

Tjong SC. Structure, morphology, mechanical and thermal characteristics of the in situ composites based on liquid crystalline polymers and thermoplastics. Mater Sci Eng R 2003; 41: 1-60.

Toebes MJ, Bitter JH, van Dillen AJ, de Jong KP. Impact of the structure and reactivity of nickel particles on the catalytic growth of carbon nanofibers. Catal Today 2002; 76: 33-42.

Toebes MJ, van Heeswijk JMP, Bitter JH, van Dillen AJ, de Jong KP. The influence of oxidation on the texture and the number of oxidation-containing surface groups of carbon nanofibers. Carbon 2004; 42: 307-15.

Thongruang W, Spontak RJ, Balik CM. Correlated electrical conductivity and mechanical property analysis of high density polyethylene filled with graphite and carbon fiber. Polymer 2002; 43: 2279-86.

Thostenson ET, Li C, Chou TW. Nanocomposites in context. Comps Sci Technol 2005; 65: 491-516.

Turek DE, Simon GP, Smejkal F, Grosso M, Incarnato L, Acierno D. Transient isothermal elongational flow of thermotropic liquid crystalline polymers. Polymer 1993; 34: 204-6.

Van Gulijk C, de Lathouder KM, Haswell R. Characterizing herring bone structures in carbon nanofibers using selected area electron diffraction and dark field transmission electron microscopy. Carbon 2006; 44: 2950-6.

Vilcakova J, Saha P, Kresalek V, Quadrat O. Pre-exponential factor and activation energy of electrical conductivity in polyester resin/ carbon fiber composites. Synthetic metals 2000; 113: 83-7.

Uchida T, Anderson DP, Minus ML, Kumar S. Morphology and modulus of vapor grown carbon nano fibers. J Mater Sci 2006; 41: 5851-6.

Wang Y, Serrano S, Santiago-Aviles JJ. Raman characterization of carbon nanofibers prepared using electrospinning. 2003; 138: 423-7.

Wilson DJ, Vonk CG, Windle AH. Diffraction measurements of crystalline morphology in a thermotropic random copolymer. Polymer 1993; 34: 227-37.

Wolf H, Willert-Porada. Electrically conductive LCP-carbon composite with low carbon content for bipolar plate application in polymer electrolyte membrane fuel cell. J Power Source 2006; 153: 41-6.

Wong YW, LO KL, Shin FG. Electrical and thermal properties of composite of liquid crystalline polymer filled with carbon black. J Appl Polym Sci 2001; 82: 1549-55.

Wu J, Schultz JM. Calculation of mesophase percentage of polymer fibers from 2D wide-angle X-ray scattering patterns. Polymer 2002; 43: 6695-6700.

Wu G, Asai S, Sumita M. Entropy Penalty-Induced Self-Assembly in Carbon Black or Carbon Fiber Filled Polymer Blends. Macromolecules 2002; 35: 945-51.

Yang S, Lozano K, Lomeli A, Foltz HD, Jones R. Electromagnetic interference shielding effectiveness of carbon nanofiber/LCP composites. Composites Part A 2005; 36: 691-7.

Yu W, Santiago S, Santiago-Aviles JJ. Raman characterization of carbon nanofibers prepared using electrospinning. Synth Metals 2003; 138: 423-7.

Zeng J, Saltysiak B, Johnson WS, Schiraldi DA, Kumar S. Processing and properties of poly(methyl methacryalte)/carbon nanofiber composites. Composites Part B 2004; 35: 245-9.

Zhang H, Zhang Z, Breidt C. Comparison of short carbon fibre surface treatments on epoxy composites: I. Enhancement of the mechanical properties. Comp Sci Tech 2004; 64: 2021-9

Zheng R, Zhao Y, Liu H, Liang C, Cheng G. Preparation, characterization and growth mechanism of platelet carbon nanofibers. Carbon 2006; 44: 742-6.